Probing Functional Network Topology in Major Depressive Disorder on the Cellular and Systems Levels

DISSERTATION ZUR ERLANGUNG DES DOKTORGRADES DER NATURWISSENSCHAFTEN (DR. RER. NAT.)
DER FAKULTÄT FÜR BIOLOGIE UND VORKLINISCHE MEDIZIN DER UNIVERSITÄT REGENSBURG

Vorgelegt von

RAHAF ISSA

رهف عيسى

aus

Lattakia, Syria

Im Jahr 2023

Der Promotionsgesuch wurde eingereicht am:

23.11.2023

Die Arbeit wurde angeleitet von:

Prof. Dr. Christian Wetzel

Unterschrift:

Rahaf Issa

Abstract

The function and dynamics of brain networks are products of the complex interplay among the networks' constituent components. Common organizational principles are thought to govern this interplay across spatial scale. Such organizational features of functional network topology, such as integration and segregation, are known to be altered in depression. However, how depression affect functional topology across the different scales of network organization remains a domain poorly understood. This work aims to investigate whether MDD patients and healthy controls differ in features of functional network topology and to assess whether such differences are consistent across two levels of granularity: the cellular and systems levels.

Cellular human neural networks were developed through reprogramming of skin fibroblasts collected from nine MDD patients and nine age- and sex-matched healthy controls. These cellular networks were examined by means of Calcium imaging. Seven of these same patients and seven matched controls were recruited for a follow up session of functional magnetic resonance imaging to capture functional networks on the systems level. Graph theory analysis was utilized to quantify topological properties of segregation, integration, and overall connections using the graph metrics clustering coefficient, global efficiency, and average node degree, respectively. Additionally, the efficiency and centrality of individual brain regions were examined to detect any MDD-related differences in nodal topology.

At the cellular level, iPSCs-derived networks of MDD patients showed decreased clustering coefficient and average node degree. On the other hand, large-scale brain networks did not exhibit significant group differences in global functional topology, although a contrasting trend emerged involving enhanced global efficiency and average node degree in networks of depressed patients. Similarly, nodal graph metrics did not differ between groups. Nonetheless, trends of altered betweenness centrality were observed in anterior insula and intraparietal sulcus.

The current work marks the first attempt to explore multiscale alterations in functional network topology in MDD. Together, the findings suggest reduced segregation and overall node connections in microscale networks of depressed patients. They also suggest a potential compensatory mechanism of micro-macro scale association that might explain the contrasting patterns of topology seen across scales. This work sets a framework for a scale-bridging investigation to understand how network topology across scale is affected in mental disorders.

Zusammenfassung

Die Funktion und die Dynamik von Gehirnnetzwerken sind das Ergebnis des komplexen Zusammenspiels der einzelnen Komponenten der Netzwerke. Es wird angenommen, dass dieses Zusammenspiel auf verschiedenen räumlichen Ebenen von gemeinsamen Organisationsprinzipien bestimmt wird. Es ist bekannt, dass solche organisatorischen Merkmale der funktionellen Netzwerktopologie, wie Integration und Segregation, bei Depressionen verändert sind. Wie sich Depressionen auf die funktionelle Topologie in den verschiedenen Skalen der Netzwerkorganisation auswirken, ist jedoch noch nicht ausreichend erforscht. In dieser Arbeit soll untersucht werden, ob sich Patienten mit MDD und gesunde Kontrollpersonen in den Merkmalen der funktionellen Netzwerktopologie unterscheiden und ob diese Unterschiede auf zwei verschiedenen Ebenen bestehen: auf der zellulären und der Systemebene.

Durch Reprogrammierung von Hautfibroblasten, die von neun MDD-Patienten und neun alters- und geschlechtsgleichen gesunden Kontrollpersonen entnommen wurden, wurden zelluläre menschliche neuronale Netzwerke entwickelt. Diese zellulären Netzwerke wurden mit Hilfe der Kalzium-Bildgebung untersucht. Sieben dieser Patienten und sieben alters- und geschlechtsgleiche Kontrollpersonen wurden für eine Folgesitzung mit funktioneller Magnetresonanztomographie rekrutiert, um funktionelle Netzwerke auf Systemebene zu erfassen. Mit Hilfe der graphentheoretischen Analyse wurden die topologischen Eigenschaften der Segregation, der Integration und der Gesamtverbindungen anhand der Graphmetriken Clustering-Koeffizient, globale Effizienz und durchschnittlicher Knotengrad quantifiziert. Zusätzlich wurden die Effizienz und Zentralität einzelner Hirnregionen untersucht, um etwaige MDD-bedingte Unterschiede in der Knotentopologie zu erkennen.

Auf zellulärer Ebene wiesen iPSCs-abgeleitete Netzwerke von MDD-Patienten einen geringeren Clustering-Koeffizienten und durchschnittlichen Knotengrad auf. Andererseits wiesen großräumige Hirnnetzwerke keine signifikanten Gruppenunterschiede in der globalen funktionellen Topologie auf, obwohl sich ein kontrastierender Trend abzeichnete, der eine höhere globale Effizienz und einen höheren durchschnittlichen Knotengrad in Netzwerken depressiver Patienten beinhaltete. Auch die Metrik der Knotengraphen unterschied sich nicht zwischen den Gruppen. Dennoch wurden in der anterioren Insula und im intraparietalen Sulcus Tendenzen zu einer veränderten Betweenness-Zentralität beobachtet.

Die aktuelle Arbeit stellt den ersten Versuch dar, multiskalige Veränderungen in der Topologie funktioneller Netzwerke bei MDD zu untersuchen. Die Ergebnisse deuten auf eine geringere Segregation und insgesamt geringere Knotenverbindungen in mikroskaligen Netzwerken von depressiven Patienten hin. Sie deuten auch auf einen potenziellen Kompensationsmechanismus der Mikro-Makro-Assoziation hin, der die kontrastierenden Muster der Topologie auf verschiedenen Skalen erklären könnte. Diese Arbeit bildet den Rahmen für eine skalenübergreifende Untersuchung, um zu verstehen, wie die Netzwerktopologie über Skalen hinweg bei psychischen Störungen beeinflusst wird.

Content

ABSTRACT II

ZUSAMMENFASSUNG III

LIST OF FIGURE VIII

LIST OF TABLES IX

LIST OF EQUATIONS X

LIST OF ABBREVIATIONS XI

CHAPTER 1. INTRODUCTION 1

1.1. A JOURNEY THROUGH NETWORK NEUROSCIENCE'S TIMELINE 1

1.2. THE BRAIN AS A COMPLEX NETWORK 4

1.2.1. Fundamental principles of brain network organization 4

1.2.2 Topology and graph theory 6

1.2.3. It is a small world, isn't it? 12

1.3. THE MULTISCALE BRAIN 15

1.3.1. Functional and structural network relationship 18

1.3.2. Mapping structural and functional neural connections 19

1.4. MAJOR DEPRESSIVE DISORDER 22

1.4.1. Definition of depression 22

1.4.2. Etiology of Depression: A Complex Interplay of Nature and Nurture 24

1.4.3. Treatment options 25

1.5. STATE OF THE ART: DISTURBED FUNCTIONAL TOPOLOGY IN DEPRESSION 27

1.5.1. On the microscale 28

1.5.2. On the macroscale 31

1.6. AIM OF THE STUDY 36

CHAPTER 2. MATERIALS AND METHODS 37

2.1. ON THE MICROSCALE 37

2.1.1. Participants and behavioral assessment 37

2.1.2. Cultivating primary human fibroblasts and generating hiPSCs 38

2.1.3. Generating and culturing of hiPSC-derived neural progenitor cells (NPCs) 38
2.1.4. Differentiation of NPCs into human induced neurons (iNeurons) 40
2.1.5. Microscopy and Calcium imaging 41
2.1.6. Motion correction and segmentation 43
2.1.7. Graph theory analysis 44
2.1.8. Definition of graph measures 47
2.1.9. Statistical testing 48
2.2. ON THE MACROSCALE 50
2.2.1. Participants and behavioral assessment 50
2.2.2. MRI acquisition 51
2.2.3. MRI preprocessing 52
2.2.4. Graph theory analysis 52
2.2.5. Statistical analysis: 55
CHAPTER 3. RESULTS 56
3.1. ON THE MICROSCALE 56
3.1.1. Demographic details and sample characteristics 56
3.1.2. Segregation properties 57
3.1.3. Integration properties 59
3.1.4. Average node degree 61
3.2. ON THE MACROSCALE 63
3.2.1. Demographic details and sample characteristics 63
3.2.2. Global graph theoretical analysis 63
3.2.3. Nodal graph theoretical analysis 66
CHAPTER 4. DISCUSSION 68
4.1. FINDINGS ON THE MICROSCALE 69
4.1.1. Reduced segregation capacity and overall node degree in patient-derived cellular networks 69
4.1.2. Changes in integration capacity of patient-derived cellular networks 70
4.1.3. Remarks on methodology and analysis 71
4.2. FINDINGS ON THE MACROSCALE 73
4.2.1. Alterations in global network organization of whole-brain networks of MDD patients 73

4.2.2. Alterations in nodal topological features in whole-brain networks of MDD patients 74
4.2.3. General remarks on the sample 76
4.3. INTEGRATED MICRO-MACRO VIEW 77
4.4. LIMITATIONS AND METHODOLOGICAL CONSIDERATIONS 81
4.5. FUTURE OUTLOOK 82
CONCLUSION 85
ACKNOWLEDGEMENTS 86
REFERENCES 88
APPENDIX A. METHOD-RELATED MATERIAL 117
APPENDIX B. RESULT-RELATED MATERIAL 126

List of Figure

FIGURE 1. GRAPH METRICS OF SEGREGATION 9
FIGURE 2. SHORTEST PATH IS A MEASURE OF INTEGRATION 10
FIGURE 3. GRAPH METRICS OF CENTRALITY AND INFLUENCE 11
FIGURE 4. FUNDAMENTAL TOPOLOGICAL ATTRIBUTES OF BRAIN NETWORKS 14
FIGURE 5. THE MULTISCALE ORGANIZATION OF THE BRAIN 17
FIGURE 6. DSM-5 CRITERIA FOR THE CLINICAL DIAGNOSIS OF MAJOR DEPRESSIVE DISORDER 24
FIGURE 7. DEVELOPING A HUMAN CELLULAR MODEL AND WHOLE-BRAIN, LARGE-SCALE MODEL TO PROBE NETWORK TOPOLOGY IN DEPRESSION. 42
FIGURE 8. PROCESSING PIPELINE AND GRAPH THEORETICAL ANALYSIS OF CA^{2+} IMAGING RECORDINGS AND FMRI DATA. 46
FIGURE 9. CONNECTION DENSITY OF WHOLE-BRAIN NETWORKS ACROSS GROUPS AS A FUNCTION OF CORRELATION THRESHOLD R_{THRESH}. 54
FIGURE 10. DECREASED *CLUSTERING COEFFICIENT* IN PATIENT-DERIVED NEURONS COMPARED TO CONTROLS ACROSS VARYING NETWORK THRESHOLDS AND SIZES. 58
FIGURE 11. ALTERATIONS IN *GLOBAL EFFICIENCY* ACROSS EXPERIMENTAL GROUPS, THRESHOLDS, AND NETWORK SIZES. 60
FIGURE 12. DECREASED *AVERAGE NODE DEGREE* IN PATIENT-DERIVED NEURONS COMPARED TO CONTROLS ACROSS VARYING NETWORK THRESHOLDS AND SIZES. 62
FIGURE 13. DIFFERENCES IN FUNCTIONAL NETWORK ORGANIZATION BETWEEN GROUPS ON THE MACROSCALE 65
FIGURE 14. CHANGES IN NODAL *BETWEENNESS CENTRALITY* IN THE BRAIN OF DEPRESSED PATIENTS IN COMPARISON TO HEALTHY CONTROLS AT DIFFERENT CORRELATION THRESHOLDS. 67

List of Tables

TABLE 1. HAMD CUT-OFF SCORES ---------- 37

TABLE 2. BDI SCALE CUT-OFF POINTS ---------- 51

TABLE 3. DEMOGRAPHIC AND CLINICAL CHARACTERISTICS OF MICROSCALE STUDY'S COHORTS ---------- 57

TABLE 4. DEMOGRAPHIC PROFILE AND MOOD RATING OF MACROSCALE STUDY'S COHORTS ---------- 63

TABLE 5. DESCRIPTIVE AND INFERENTIAL STATISTICS ON NODAL BETWEENNESS CENTRALITY IN LARGE-SCALE NETWORKS ---------- 66

List of Equations

EQUATION (1) CLUSTERING COEFFICIENT 47

EQUATION (2) GLOBAL EFFICIENCY 47

EQUATION (3) AVERAGE NODE DEGREE 48

EQUATION (4) BETWEENNESS CENTRALITY 55

List of abbreviations

AAIC	Anterior agranular insular complex
AM	Acquisition matrix
ANDeg	Average node degree
Ara-C	Cytosine arabinoside (Cytarabine)
BC	Betweenness centrality
BMI	Body mass index
C	Clustering coefficient
CCN	Cognitive control network
CRH	Corticotrophin-releasing hormone
DBS	Deep brain stimulation
DIV	Days in vitro
DMEM/F12	Dulbecco's Modified Eagle Medium/Nutrient Mixture F-12
DMN	Default mode network
dMRI	Diffusion magnetic resonance imaging
DSM-V	Diagnostic and Statistical Manual of Mental Disorders, 5th
DTI	Diffusion tensor imaging
ECT	Electroconvulsive therapy
EEG	Electroencephalography
E_{glob}	Global efficiency
E_{loc}	Local efficiency
EPI	Echo-planar imaging
FA	Flip angle
FC	Functional connectivity
FoV	Field of view
GABA	Glutamate and γ-aminobutyric acid
$HAMD_{21}$	21-item Hamilton Rating Scale for Depression

HPA	Hypothalamic-pituitary-adrenal
iN	Induced neurons
IPS	Intraparietal sulcus
iPSCs	Induced pluripotent stem cells
L	Shortest path length
MAOIs	Monoamine oxidase inhibitors
MDD	Major depressive disorder
MEG	Magnetoencephalography
MP_RAGE	Magnetization Prepared Rapid Gradient Echo
NASSAs	Noradrenergic and specific serotonergic antidepressants
NDM	neuronal differentiation medium
NEM	Neural expansion medium
NGS	Next generation sequencing
NMDA	N-methyl-D-aspartate glutamate receptor antagonist
NPC	Neural progenitor cells
NRIs	Norepinephrine reuptake inhibitors
PBS	Phosphate Buffered Saline
PLO	Ploy-L-ornithine
Rs-fMRI	Resting-state functional magnetic resonance imaging
r_{thresh}	Correlation threshold
SEM	Standard error of the mean
SN	Salience network
SNRIs	Serotonin-norepinephrine reuptake inhibitors
SSRIs	Selective serotonin reuptake inhibitors
TCAs	Tricyclic antidepressants
TE	Echo time
TMS	Transcranial magnetic stimulation

TR	repetition time
TRD	Treatment resistant depression
VNS	Vagus nerve stimulation

Chapter 1. Introduction

1.1. A journey through network neuroscience's timeline

"In a way, the history of neuroscience is the history of its methods"

Yuste, 2015

For years, the neuron doctrine that crowned the neuron as the structural and functional building block of the nervous system constituted the main school of thought in modern neuroscience. This conceptual principle was built upon the outstanding work of Santiago Ramón y Cajal (1852–1934) in characterizing the properties of the neural cell (Ramón y Cajal, 1888). The general focus on individual neuron properties in the late 19th and early 20th centuries was driven by the methodological advancements in single-cell techniques in that era, such as Golgi staining, the light microscope, and microelectrodes for single-cell recordings. While the neuron doctrine facilitated a comprehensive understanding of the nervous system using the available analytical tools of its time (Yuste, 2015), such a reductionist approach fell short in providing a comprehensive framework that links neuron function to cognition and behavior within which mental illnesses could be explained. As a result of this major conceptual limitations, the field's investigational lens started to shift its focus from the single neuron to encompass a more holistic view of neural ensembles or populations and their interaction. This marked the birth of network theory in contemporary neuroscience which states that intricate patterns of connectivity between ensembles of neurons, rather than the discrete individual neurons themselves, serve as the foundation of brain function (Churchland & Sejnowski, 1992). According to network models, the functional properties of a network emerge from the interaction of its individual elements which may not possess these properties when considered in isolation. Although theoretical models of neural network were formulated since the 1940s (Hebb, 1949; McCulloch & Pitts, 1943), the technology required for testing these theories was lagging behind. Nevertheless, the recent advances in optical, magnetic, electrophysiological,

and computational modelling techniques have revolutionized the field of network neuroscience and made it possible to capture the activity of extended neural circuits and probe and perturb their connectivity and dynamics as an attempt to understand their role in brain function (Yuste, 2015). Mapping the comprehensive set of connection between neural elements of the nervous system, commonly known as a the *"connectome"*, has long been a primary objective of systems neuroscience. Not only does this pursuit promise to advance our understanding of the brain's basic cognitive functions, but it also has the potential to reveal how irregularities in network properties may contribute to the development of pathological processes in the context of mental illnesses.

The organizational principles governing neural networks in the brain are nonrandom and conserved across species and special scales (see section 1.2). The special organizational levels of brain networks span the micro-, meso-, and macroscale (see section 1.3). At each of these special scales, network connectivity can be described in terms of the structural or functional relations between the network's elements (see section 1.3.1). Akin to earlier advancement in neuroscience, the accumulation of connectivity data across different scales followed the technological breakthroughs made in optical imaging and physiological recording (Fornito et al., 2016; Sporns, 2016). This is exemplified by the successful reconstruction of the entire nervous system of *Caenorhabditis elegans* by White et al., (1986) and the identification of the links between wiring features and specific patterns of behavior in *C.elegnas*, drosophila, and mouse retina (Jarrell et al., 2012; Rivera-Alba et al., 2011; Briggman et al., 2011). Moreover, the growing accessibility of imaging techniques has contributed to our understanding of both structural and functional aspects of the mammalian brain organization, whether on the cellular or the systems level (section 1.3.2). The invasiveness of cellular imaging methods such as Calcium imaging and tract-tracing has been overcome by the introduction of noninvasive, whole-brain covering imaging tools such as functional magnetic resonance imaging (fMRI) and diffusion tensor imaging (DTI). The safety and flexibility of these methods resulted in a rapid expansion in large-scale connectivity data from individual subjects and allowed for clinical comparison between groups to identify connectivity-related disease phenotypes.

However, acquiring the data was only half the challenge. The deep insights collected from the large amount of complex network data would have not been possible without the giant leap made in analytical approaches and statistical and mathematical modelling of neural data. By

using computational tools that are mostly borrowed from physics and mathematics, researchers have been able to address the brain as a complex system of interconnected elements and model the relations between these elements to depict, elucidate, and predict the behavior of that system (Bassett et al., 2018).

As brain network data collected at individual observation levels becomes increasingly ubiquitous, a major challenge arises in developing a comprehensive, cross-level approach to address the multiscale nature of brain network organization and function. An accumulating line of evidence suggests that the multiple levels of brain network organization are related and interlinked (van den Heuvel et al., 2019) (see section 1.3). Therefore, an approach that bridges the gap between different scales of brain organization can provide insight into how alterations in network organization at one level may impact function and dynamics at other levels. This approach offers the potential to uncover the fundamental mechanisms behind cognitive dysfunction in the context of mental disorders, presenting a challenging, yet promising avenue of research.

One of the major challenges in such a cross-level investigation of brain networks in the realm of psychiatric diseases is the availability of multiscale data collected from the same groups of individuals. While large-scale human brain networks can be examined non-invasively using brain imaging techniques, obtaining non-invasive microscale data from the same human subjects has posed difficulties. As a result, most available data on cellular-level network organization are derived either from animal models or postmortem tissue, which, while informative, lacks the resemblance to a viable human tissue. Once again, the stride of technology comes to the rescue. The introduction of the human induced pluripotent stem cell (hiPSC) technology in the late 2000 (Takahashi et al., 2007) has helped overcome this hurdle and has unlocked novel possibilities in disease modelling and drug discovery (Soliman et al., 2017) (see section 1.5.1). With this technique, somatic cells can be reprogrammed into adult pluripotent stem cells that can adopt any neuronal fate, providing disease-relevant, patient-specific neural tissues that were previously inaccessible.

The work presented in this thesis seeks to integrate some of the above-mentioned cutting-edge advances in network neuroscience to explore multiscale functional network organization in the realm of major depressive disorder. This pioneering exploration spans the cellular,

microscale and the systems, macroscale levels. The following introduction section embarks on elucidating the foundational aspects of human brain organization and their representation through graph theory (section 1.2). It further delves into the mapping of these topological features across different spatial scales and network modalities (structure and function) (section 1.3), with particular emphasis on their potential involvement in psychopathological processes. The introduction also provides a concise overview of major depressive disorder (MDD), encompassing its definition, etiology, and available treatment options (section 1.4). This is followed by a review of the current state of the art addressing changes in functional topology in depression across both micro and macroscale (section 1.5). With the necessary background information provided, the chapter concludes by defining the precise aim of this study.

1.2. The brain as a complex network

1.2.1. Fundamental principles of brain network organization

> *"We realized that all of the various conformations of the neuron and its various components are simply morphological adaptations governed by laws of conservation for time, space and material"*
>
> *Ramón y Cajal (1995), p.116, Volume I.*

As in any complex system, the function and resulting behavior of the brain arise from the intricate interplay among its constituent components, be they individual neurons or a population of neurons forming brain regions (Bressler & Menon, 2010; Vértes & Bullmore, 2015). This core concept of network neuroscience allows one to represent the brain as a network providing a simplified framework to tackle its complexity and offering a valuable insight into its fundamental processes in health and in disease.

Accumulated evidence strongly supports the notion that the organizational principles of the brain's network is nonrandom, exhibiting a significant degree of conservation across species, spatial scales, and between functional and structural modalities (van den Heuvel et al., 2016; Bullmore & Sporns, 2009). More than a decade ago, Cajal proposed what is called conservation laws (see quote at the beginning of this section). These laws govern the organization of almost all aspects of the nervous system, including its communication and

connectivity. Cajal anticipated that aspects of brain network organization, whether anatomical or functional, are selected to minimize three main critical elements: space, time, and material.

The brain resides within a finite three-dimensional physical space. Building and maintaining such a spatially embedded system place high constrains on many anatomical features such as the number of neurons and wiring patterns involving connection density (number of synapsis), axonal length, and axonal cross-sectional diameters. This pertains to Cajal's conservation laws concerning space and material, which postulate that complex networks of the brain evolve to minimize these aspects by reducing what is known as axonal wiring cost (Attwell & Laughlin, 2001). Cost, in this context, refers to any biological expenditure utilized for establishing connections between neurons, be it energy, metabolism requirements, or cellular resources (Bullmore & Sporns, 2012; Chklovskii, 2004). Consequently, it becomes advantageous - and highly probable - for the brain network to construct axonal connections with shorter projections and smaller diameters between spatially adjacent neurons, optimizing spatial utilization and minimizing resource expenditure (Bullmore & Sporns, 2009). Under these constrains of space and material, connections between remote neurons are rendered more costly and therefore, less likely.

Time, on the other hand, an aspect related to function and efficiency, can be conserved by enhancing signal transmission speed and minimizing conduction delay between remote regions of the brain (Wen & Chklovskii, 2005). For instance, signal delay between distant regions can be minimized by establishing long-distance direct connections that passes through as few synapsis as possible. These long-distance connections are vital for brain function and dynamics as they mediate strong oscillations in neural networks, enabling the efficient spread of synchronized activity among topologically remote oscillators (Buzsáki et al., 2004). However, as discussed above, establishing and sustaining such direct, monosynaptic short-cuts that facilitate information flow and coordination of neural activity is energy expensive. Furthermore, conduction velocity is higher along axonal projections with large cross-sectional diameter, which is an expensive feature (Puppo et al., 2018; Niven & Laughlin, 2008). This shows that while minimizing wiring costs is a strong selection pressure in constructing brain networks, exclusively prioritizing brain networks for this aspect can potentially compromise overall function and efficiency. Thus, the brain, like any complex spatially embedded system, must strike an economical balance between minimizing wiring cost and maximizing efficiency

in information flow and processing (Fornito et al., 2011; Meunier et al., 2010; Schröter et al., 2017). This trade-off between function and cost underpins the concept of *"brain economy"*, which illustrates how the brain's organization enables efficient performance by optimally managing its resources (Bullmore & Sporns, 2012). The focal point of this concept is to prioritize efficient resource management rather than solely focusing on cost reduction. In other words, brain networks occasionally compromise the minimum cost in order to ensure efficient functionality, as exemplified by the presence of the expensive direct short-cut connections.

The presence of such a function/cost trade-off highlights the complex, non-trivial organization of brain networks. Complex organization refers to the presence of intricate structure that is irregular and temporally dynamic allowing for complex function (Boccaletti et al., 2006). In particular, when a network compromises a certain cost in favor of functional efficiency, two contrasting aspects emerge: the segregation of different regions within the network, and the integration of information across those regions. Neighboring neurons in the brains of higher vertebrates tend to form densely connected neuronal clusters or communities to minimize wiring costs. This modular architecture allows for functional segregation, where distinct communities or modules perform specialized functions. Conversely, integration in brain networks occurs when certain material and metabolic costs are sacrificed to establish costly long-range connections between distant parts of the network, facilitating efficient large-scale information transmission. Therefore, maintaining a cost/function trade-off allows the brain to strike a balance between integration and segregation processes. This balance is critical to accommodate the highly dynamic cognitive demands and to generate complex, adaptive behavior (Cocchi et al., 2013).

These fundamental principles governing brain network organization are often empirically depicted and quantified through the application of graph theory. The following section touches on the basics of graph theory and elucidate the relevance of its metrics in revealing insights into the topological architecture of human brain networks.

1.2.2. Topology and graph theory

Topology first developed as a branch of mathematics in the 19th century and involved studying geometric object properties that are invariant under any continuous spatial deformation. In the context of network science, network topology refers to the patterns of

connections and relations occurring between the network's elements (Bullmore & Sporns, 2012). Graph theory, originally developed in the 18th century by the mathematician Leonhard Euler (1707-1783), became pivotal for network analysis to describe the general principles of complex systems organization. It was not until the end of the 20th century that graph theory found its way into biology and network neuroscience, unravelling the intricate connectivity patterns in the cortex and enhancing our understanding of brain network organization (Felleman & Van Essen, 1991; Young, 1992; Watts & Strogatz, 1998).

The power of graph theory lies on its ability to provide a simple, straightforward means to examine complex systems like the brain. Within this mathematical framework, a network is modeled as a graph consisting of vertices (nodes) and their connections (edges) (Figure 1A). The interpretation of edges differs depending on the network modality in hand, whether structural or functional (Butts, 2009, Sporns, 2011). In graphs describing structural networks, an edge reflects the presence of an anatomical connection between the nodes, while in functional graphs, edges typically indicate coactivation between nodes, inferred statistically by pairwise temporal correlations between their activity (Park & Friston, 2013). Graphs can be further differentiated based on other properties of their edges. For instance, a graph can be directed, in which edges represent a directional relationship between the nodes, or undirected, in which edges represent a symmetrical relationship with no directional information (Stam & Reijneveld, 2007). Another distinction is made between binarized and weighted graphs. Binarized or unweighted graphs assign binary values (1 or 0) to their edges after a thresholding procedure, denoting the presence or absence of a connection. In such graphs, all present edges are considered equally important or "unweighted". In contrast, edges in weighted graphs retain their numerical values, which indicate the strength of the connection or the distance between the nodes, providing additional information about the magnitude of the relationships within the graph (Stam & Reijneveld, 2007).

Once nodes of a given network have been defined, their pair-wise structural or functional associations are measured to create a "*connectivity matrix*", which is one way to represent a network. When binarized undirected graphs are examined, a binarized "*adjacency matrix*" is generated by thresholding the aforementioned connectivity matrix. Subsequently, graph measures are computed to examine relevant aspects of that network's architecture, allowing to compare individuals and groups of subjects. These measures serve as robust and reliable means

to characterize both the overall global topology of the network as well as the specific local topological features of individual nodes. The broad range of graph metrics available can be categorized into three distinct classes based on the attributes of network organization they capture: measures of segregation, integration, and influence (Sporns, 2011).

1.2.2.1. Measures of segregation

A graph with segregation attributes shows the capacity to form clusters of densely connected nodes that are adjacent and functionally related. This clustered architecture with localized specialization grants the system robustness, reliability and resilience to injuries, as damage to one specific region would not cripple the entire network (Bullmore & Sporns, 2009b; Meunier et al., 2010; Robinson et al., 2009). Furthermore, clustered topology influences neural function and shapes network dynamics (Arenas et al., 2006; Sporns et al., 2000; Yamamoto et al., 2018). Graph metrics of segregation depict the presence of such functionally specialized clusters or communities. Examples of segregation metrics include *clustering coefficient*, *local efficiency*, and *modularity*. *Clustering coefficient* (*C*) measures the number of closed triangles that are connected to a given node relative to the number of all possible triangles (Fornito et al., 2016) (**Figure 1**). In other words, it depicts the proportion of a node's neighbors that are also neighbors of each other. *Local efficiency* (E_{loc}) is another measure of segregation that quantifies the effectiveness of information exchange within localized subnetworks (Latora & Marchiori, 2001). These subnetworks are defined as direct neighbors of a given node after removing that node and its incident edge. *Modularity* quantifies the number of nonoverlapping "*modules*" in the network, which are community structures characterized by dense within-module connections, while exhibiting sparse connectivity between modules (Newman, 2004) (**Figure 1**). *Modularity* is considered a more sophisticated measure of network segregation as it not only depicts the presence of clustered communities but also provide detailed information about their specific size and composition (Rubinov & Sporns, 2010).

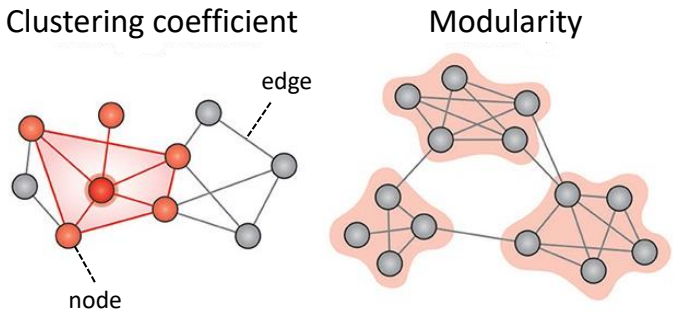

Figure 1. Graph metrics of segregation. *Left*, clustering coefficient reflects how much neighbors of a given node are also neighbors of each other. *Right*, Modularity quantifies the number of "*modules*" in the network. Modules refer to clustered communities in the network which exhibit dense connections between nodes within a given module or cluster, and sparse connections between nodes belonging to different modules. *Adapted from (Farahani et al., 2019).*

1.2.2.2. Measures of Integration

Functional integration indicates the capacity of the network to sustain rapid and efficient communication between all its nodes, combining information from its specialized, distributed parts. Graph theoretical measures of integration captures this capacity quantitatively by utilizing the concept of path (Rubinov & Sporns, 2010). A path in graph theory refers to the number of edges that need to be traversed in order to travel from one node to another (Bullmore & Sporns, 2009). Therefore, the average path length serves as an indicator of the speed and efficiency with which information is transmitted throughout that network, with shorter path lengths on average reflecting more efficient and integrative networks. The *characteristic path length* (*L*) is a common integration measure that stems from this concept. *L* represents the average shortest paths linking all nodes in the network (**Figure 2**). However, the *characteristic shortest path* is not numerically applicable in "fragmented" graphs, in which there is at least one node that is not connected by an edge to any other node in the graph, dividing the graph into more than one component (Fornito et al., 2016). This problem often occurs when applying relatively high thresholds to connectivity matrices that might result in the disconnection of the weakly connected regions, forming disconnected components. In such cases, the path length between this disconnected node and any other node in the graph is assumed to be infinite, which means that the *characteristic path length* will be also infinite. One approach to avoid this problem in a fragmented graph is to compute the reciprocal of the shortest path length. By taking the reciprocal of the shortest path length, the infinite path between two disconnected nodes becomes zero, as $\frac{1}{\infty} = 0$, contributing nothing to the sum and keeping the mean

necessarily finite. One graph metric that adopt this approach is *global efficiency* (E_{glob}), defined as the reciprocal of the shortest path length (Rubinov & Sporns, 2010; Feldt et al., 2011).

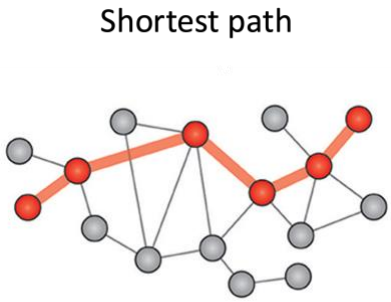

Figure 2. Shortest path is a measure of integration. It quantifies the minimum number of edges that need to be traversed to get from one node to the other. *Adapted from (Farahani et al., 2019)*.

Most of the above-mentioned segregation and integration measures provide a node-level topological description. When these nodal measurements are averaged across the network's nodes, they provide a comprehensive, global assessment of the segregation and integration features of the entire network.

1.2.2.3. Measures of Influence

Measures of influence reveal the topological importance or contribution of individual nodes in the graph. Such measures are highly interesting in the context of brain networks as they emphasize how the embedding of brain regions within the network governs their functional participation in dynamic processes (Sporns et al., 2007). Graph theory offers a wide range of influence measures, also called measures of centrality or "*hubness*", as they identify highly connected regions, so-called "*hubs*". Each of these measures highlights a distinct aspect of the region participation in the network (**Figure 3**). For example, *node degree*, also known as *degree centrality*, is one of the simplest and easily computed measures to identify hubs (Bullmore & Sporns, 2009) (**Figure 3**). It is simply defined as the number of edges connected to a specific node within a network. Nevertheless, *degree centrality* solely considers the number of neighbors connected to a node, failing to account for the "quality" of these neighbors, specifically whether the neighboring nodes themselves show high centrality. *Eigenvector centrality* (Bonacich, 1972) is a measure that accounts for both quantity and quality of a node's neighbors as it quantifies the influence of a node based on the centrality of

its connected neighbors. In other words, nodes with high *eigenvector centrality* are those that are connected to other highly central nodes (**Figure 3**). Some centrality measures are path-based, of which *betweenness centrality* is one example. *Betweenness centrality* (*BC*) is another measure of hubness that takes into account the number of shortest paths between all nodes in a network that passes through a given node (Freeman, 1977) (**Figure 3**). As the name implies, *BC* measures the degree to which a node lies "between" other nodes, thereby strongly mediating the flow of information across the network through the shortest paths. When a set of highly central hubs are also densely connected to each other, this organization is called "*rich-club"* and is considered to form the "connectivity backbone" in the network (Zhou & Mondragon, 2004; Van Den Heuvel & Sporns, 2011).

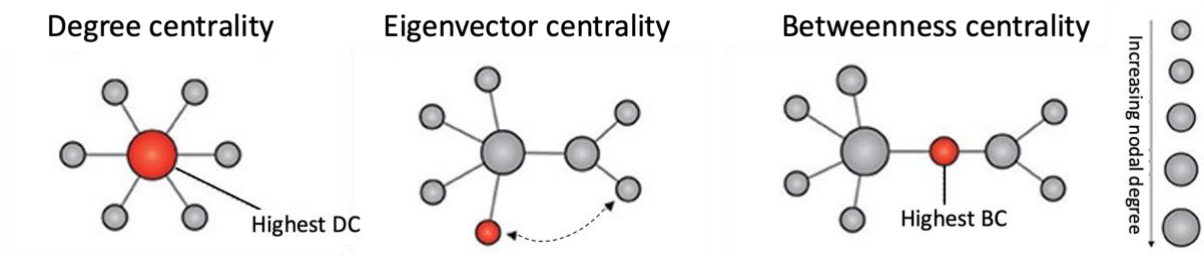

Figure 3. Graph metrics of centrality and influence. *Left,* degree centrality is calculated as the number of edges connected to a given node. *Middle,* eigenvector centrality takes both the number and the quality of a connection into account; the red node is more central than the gray one despite having the same degree. This is because the red node is connected to a central node with high *degree*. *Right, betweenness centrality* computes the proportion of shortest paths that cross through a given node relative to the total number of shortest paths in the network.

Network hubs are elements of integration. Their topological centrality allows them to play a vital role in facilitating efficient communication through rapid routing of information across distant parts of the network. This is mainly facilitated by the high number of shortest paths that a hub-node lies on. Since wiring costs depend on the number and length of connections, one expects that hubness (whether defined as high *betweenness* or simply high *degree*) is a biologically expensive topological feature as it entails increased wiring. Several studies have shown that the presence of hubs in a network, particularly when they organize in *rich-clubs*, accounts for high wiring demands and energy burden whether in humans, rodents, or in the nematode *C.elegans* (Collin et al., 2014; van den Heuvel et al., 2012; Fulcher & Fornito, 2016; Towlson et al., 2013). This high metabolic burden associated with the brain's hub-nodes

explains their increased vulnerability to diseases and lesions that might effect energy supplies, as seen in schizophrenia and Alzheimer's disease (Buckner et al., 2009; Crossley et al., 2014). Furthermore, *centrality* is a double-edged sword. On one hand *centrality* is crucial for efficient information exchange across the network. On the other hand, the high *centrality* and connectivity of hub-nodes make them more susceptible to injury as they are easy to reach by pathological processes (Fornito et al., 2015). Furthermore, hubs play a significant role in the propagation of disease and have a negative influence on the prognosis of recovery after insult (Fornito et al., 2015). Once a hub-node is affected, its topological centrality facilitates the spread of the pathological process throughout the network. This results in a diffuse impact on network function, contributing to pervasive cognitive impairment that is associated with poor recovery prognosis (Kitsak et al., 2010; Warren et al., 2014).

Therefore, exploring and understanding the complex patters of influence becomes particularly important in the context of brain disorders. These measures are not only instrumental in understanding disease mechanism and predicting the pathological progression, but also essential to identify potential targets for therapeutic interventions.

1.2.3. It is a small world, isn't it?

The term "*small-worldness*" originated from the social sciences when Milgram (1967) found that any person (from a random set) was on average 5.9 degrees distant from one target person. This suggests that any large network could be traversed with a small number of steps on average – a small world!

Later on, in their groundbreaking work, Watts & Strogatz (1998) introduced a mathematical model of the small-world phenomenon by focusing on two key network attributes: *clustering coefficient* and *characteristic path length*. The Watts-Strogatz model of small-world involved randomly rewiring the connections of a regular, lattice-like network. They found that introducing even a small number of random connections into the network led to a significant increase in its efficiency, as indicated by the decreased path length. Interestingly, these random connections had a minimal impact on the network's clustering structure. This hybrid model exhibited a unique combination of topological properties which constituted a middle ground on the spectrum of network topology between regular network

(high clustering and high segregation) and random network (short path length and high integration) (**Figure 4**). This organization that supports the delicate integration-segregation balance as a defining feature was referred to as "*small-world*" as it drew parallels to the properties of the first explored social network of Milgram (1967).

Small-worldness is ubiquitous. In fact, abundant scientific investigation has shown that brain networks organize in a small-world architecture (Achard, 2006; Achard & Bullmore, 2007; Bassett et al., 2006; Sporns & Zwi, 2004). This topology enables efficient integration of information across distant network's components while maintaining a level of segregation that allows for effective local communication and functional specialization. Such an inherit trade-off between integration and segregation is hallmark of many complex real-world systems such as the brain as it guarantees a flexible, efficient network function and rich dynamic repertoire (Achard, 2006; Achard & Bullmore, 2007). Interestingly, not only macroscale brain networks, but also neural circuits grown in cultures tend to self-organize into a small-world configuration throughout their development and maturation, whether on the microscale (tens of neurons) or the mesoscale (hundreds to thousands of neurons) (Perin et al., 2011; Schröter et al., 2017; Shimono & Beggs, 2015; Yamamoto et al., 2018; Downes et al., 2012). Several neuroimaging studies reported altered small-world organization of large-scale networks in depression (Gong & He, 2015). However, MDD-related effect on functional topology of neuronal networks on the microscale is still a domain rarely investigated. Section 1.5 will provide a comprehensive review on the existing research on alterations of small-worldness in the context of MDD.

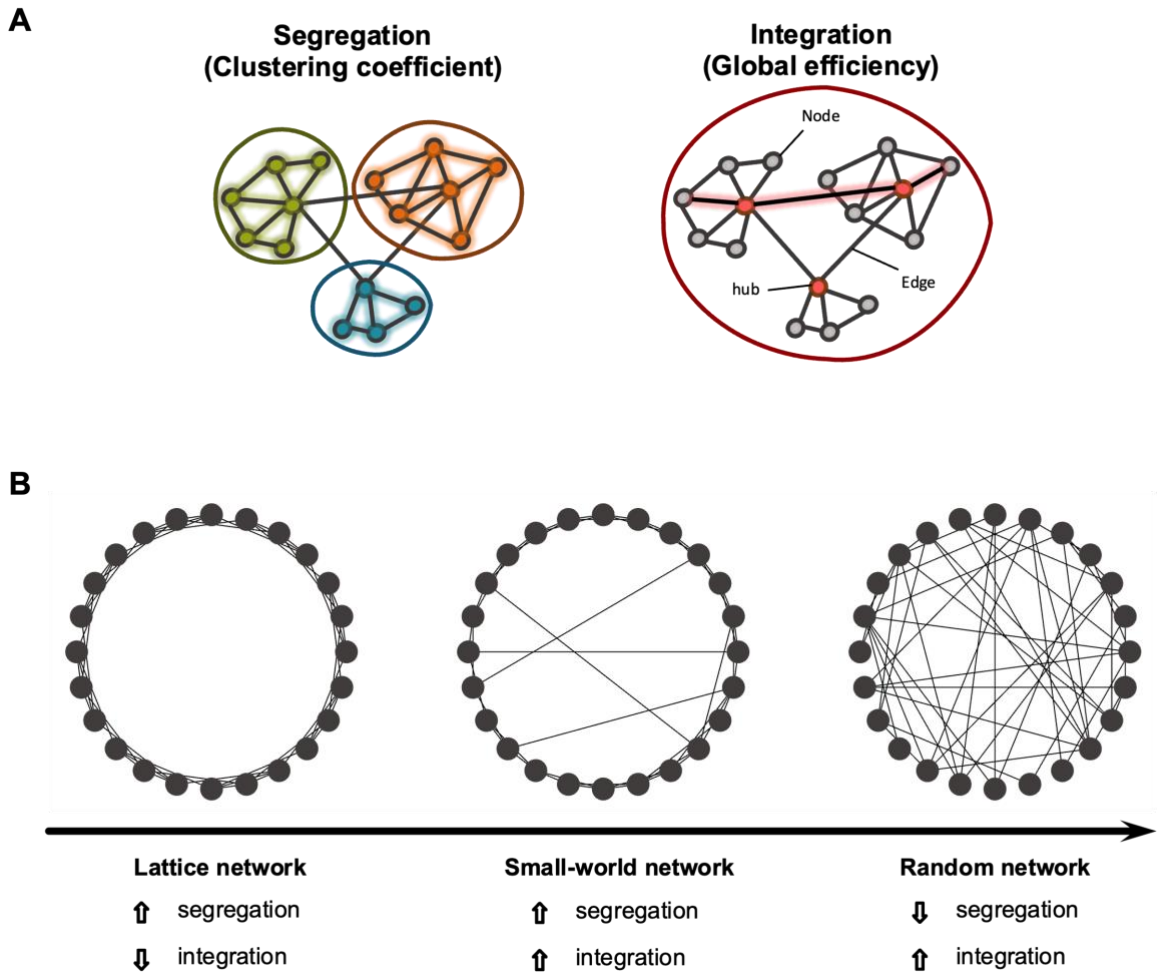

Figure 4. Fundamental topological attributes of brain networks. (A) An efficient network is one that strikes a balance between its integration and segregation attributes. Graph theory offers a framework to examine topological network properties by representing networks as graphs composed of nodes (neurons or brain regions, depending on the spatial scale) and edges (connections between nodes). *Left*, a network with segregation attributes demonstrates dense connections between neighboring nodes leading to the formation of clustered communities exhibiting specialized functions. The graph metric "clustering coefficient" is used to assess network segregation (see section 1.2.2.1 for definition). *Right*, integration capacity allows for effective coordinating and combining information arriving from different communities in the network. Integration is topologically supported by efficient long-ranging connections with short path length connecting spatially remote parts of the network. The graph metric "*global efficiency*" is used to assess network integration (see section 1.2.2.2 for definition). (B) a representation of a continuum of network topology on a randomness scale ranging from a completely lattice-like organization (left) exhibiting maximal segregation to a completely random organization exhibiting maximal integration. Brain networks organize in "*small-world*" topology (middle) which constitutes a middle ground between a regular and random topology. Small-world network combines the highly clustered topology observed in regular networks while harboring a number of efficient long-ranging paths that are characteristic for random networks. Accordingly, small-world organization in brain networks harbor a balance between integration and segregation that is crucial for efficient function and cognition.

1.3. The Multiscale Brain

Brain networks exist on multiple levels of spatial organization, ranging from micro to macroscale. At a microscale level, networks are shaped by a small number of neurons, typically tens to hundreds, that establishe intricate connectivity patterns through axonal projections and local synaptic connections. Zooming out to the mesoscale level, networks represent connections between populations of neuronal assemblies rather than individual neurons, as seen for example on the level of cortical columns or larger cytoarchitectonic regions. At the macroscale, network components are large-scale brain regions consisting of million to billions of neurons. These regions coordinate activity and integrate information through complex connectivity facilitated by white matter connections, giving rise to complex cognitive functions and behavior such as learning, memory, and decision making (**Figure 5**).

The principal topological features of brain network organization discussed in the previous sections govern the emergence of both the macro- as well as the micro-connectome. For instance, a substantial line of evidence shows that both large-scale brain networks (Achard, 2006; Bassett et al., 2006) and *in vitro* neuronal circuits of cultured neurons (Perin et al., 2011; Shimono & Beggs, 2015; Teller et al., 2014; Yamamoto et al., 2018) tend to self-organize into a small-world architecture that is conserved across both anatomical structure (Santos-Sierra et al., 2014; Yu et al., 2008) and function (Bullmore & Sporns, 2009; Downes et al., 2012). Perin et al. (2011) even proposed that microscale small-world structure serves as the building block for the emergence of larger scale nonrandom structure.

One question that might arise to the reader is: how does such a micro-macro association manifest? Several mechanisms have been proposed through which an inter-scale relationship can take form:

- The simplest suggested mechanism for micro-macro relationship proposes that microscale organizational features could serve as “Lego-like building blocks” that accumulate to form larger scale networks (Perin et al., 2011). This form of multiscale relationship implies that alteration in macroscale networks are a consequence of similar alterations that occurred in microscale networks and propagated across scales (van den Heuvel et al., 2019). However, it is argued that such multiscale link is overly simplistic when it comes to explaining organizational association in complex dynamic systems such as the brain (van den Heuvel & Yeo, 2017).

- Another form of micro-macro interaction is denoted in the organizational constrains that one scale could place on the other (Goulas et al., 2017). One of the simplest examples of such constraints is that neurons that share similarities in cell type, gene expression pattern, and/or myeloarchitecture are more likely to connect to each other (Hilgetag et al., 2016; Krienen et al., 2016; Buckner & Krienen, 2013). This cytoarchitectural similarity constitutes a "like-connect-to-like" guiding principle in the formation of the macroscale interregional corticocortical connectivity (van den Heuvel & Yeo, 2017). However, this interlevel interaction might similarly occur in the opposite direction (macro to micro). Namely, the macroscale organization can exert a top-down causal effect on network processes at the cellular level. This type of interaction is particularly evident in the context of neurodegenerative disorders, where disease onset and spread are suggested to be governed by the macro level network organization of the brain (Seeley et al., 2009; Zhou et al., 2012). For instance, during the initial stages of a disease, the modular organization of the brain network typically constrains disease-related cellular alterations to a local network surrounding the pathology's epicenter (Zhou et al., 2012). However, as the disorder progresses, these alterations begin to spread to topologically distant regions by means of integrative hub regions (Crossley et al., 2014). This phenomenon underscores the significant role of macroscale network organization in governing the spread of disease and suggests that targeting these hub regions may be an effective strategy for interventions aimed at slowing or stopping disease progression (van den Heuvel & Yeo, 2017; Crossley et al., 2014).
- Alternatively, micro-macro relationship can manifest as a common set of organizational principles that are shared between brain networks at different spatial scale (Scholtens et al., 2022). Several studies have demonstrated that distinct network configuration features are conserved across multiple network scales (Schroeter et al., 2015), modules (structural or functional), and species (van den Heuvel et al., 2016). Examples of these features include the tendency to form densely connected local clusters, together with features that promote network efficiency such as short connecting paths, hubs, and rich clubs. Such organizational principles are subject to both genetic regulation, exhibiting substantial heritability (Fornito et al., 2011; Jahanshad et al., 2012; Lydon-Staley & Bassett, 2018) as well as ongoing modulation by various environmental perturbations and behavior patterns (Gibson, 2008), and/or development (Douet et al., 2014).

The evident cross-scale interplay makes it interesting to examine how topological features unfold on different organizational levels within the same individuals. Such an endeavor aims to unravel how alterations in network organization at one level may impact function and dynamics at another level in the same organism. This scale-bridging approach holds the potential to forge a deeper understanding not only on the functional brain organization across different levels of granularity, but also on the mechanisms underlying cognitive dysfunction in the context of mental disorders. Despite the growing evidence of micro-macro scale association, our understanding of how these two organizational scales interact within the realm of psychiatric disorders remains remarkably limited. Certain endeavors have undertaken multiscale investigations in psychiatric conditions, such as schizophrenia (Lawrie et al., 2001; Romme et al., 2017) and bipolar disorder (McCarthy et al., 2014). However, these studies primarily focused on linking large-scale network attributes to specific genetic variations, without examining how network organization on the microscale might also be affected by such genetic modulations. Moreover, there is a lack of multiscale studies aimed at probing alterations in network topology in depression, a wildly common psychopathology with mechanisms that remains poorly understood.

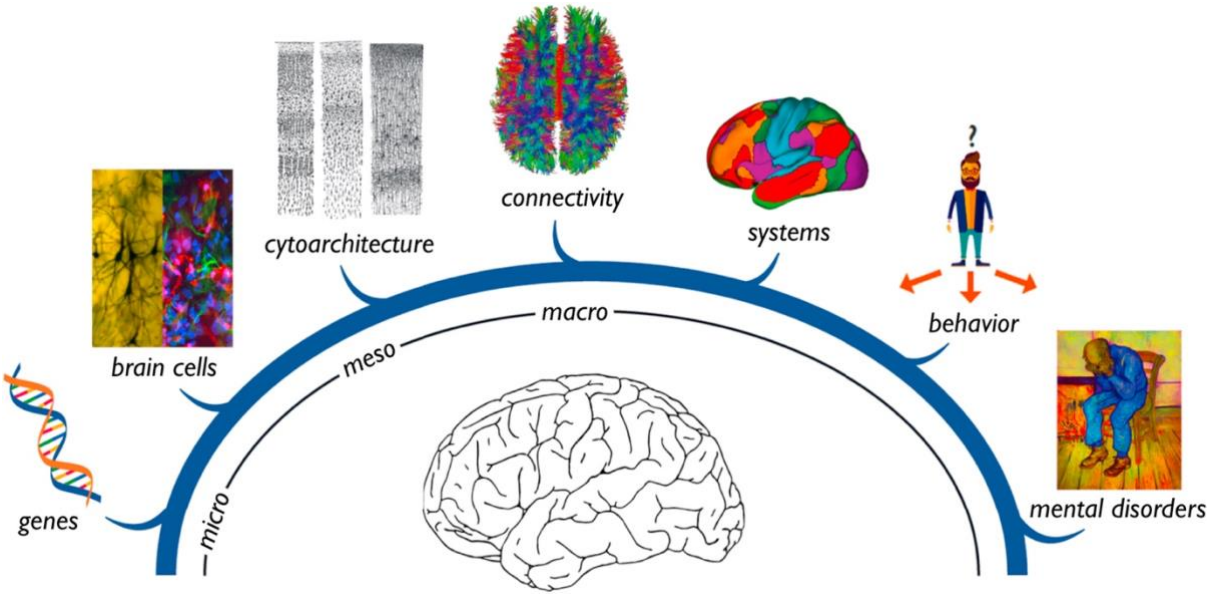

Figure 5. The multiscale organization of the brain. Examples of the multi-level organization of brain on the microscale (genes and brain cells ((left) neurons in black, (right) astrocytes in green, and microglia in red shown among human cultivated cells), mesoscale (cytoarchitecture), and macroscale (connectivity and systems). Collectively, the structure and function of these different levels of organization give rise to collective behavior. The dysfunction at one of these levels can affect the others leading to the abnormal behavior observed in mental disorders. *Reprinted from (van den Heuvel et al., 2019).*

1.3.1. Functional and structural network relationship

The interplay between structure and function in neuronal networks is dynamic and interconnected where one exerts a continuous influence on the other. Structural brain connectivity forms the backbone of functional connectivity, yet it does not rigidly dictate function. Instead, it imposes certain constrains on functional robustness and dynamic repertoire (Sporns, 2011). Within that constrained functional space, neural dynamics remain rich and varied. On a relatively long time scale, in which mechanisms of learning and plasticity could take place, functional connectivity itself can exhibit strong influence on the patterns of anatomical connections in a network (Rubinov et al., 2009).

Both structural and functional networks have been shown to exhibit a complex topology, e.g., small-worldness, modularity, and hubness (He & Evans, 2010; Stam et al., 2016; Wang et al., 2015). Several studies have been conducted on the same subjects to directly compare the two modalities of connectivity in brain networks (Hagmann et al., 2008; Honey et al., 2009; Skudlarski et al., 2008). They revealed a positive association between the strength of structural connectivity with that of functional connectivity. Notably, robust functional connections were detected between regions that lack direct structural links. This highlights the intricate interplay between direct and indirect structural pathways in shaping pair-wise dynamics within the network (Sporns, 2011). The consequences of this phenomenon are evident in brain pathologies. When a specific region within the brain network is damaged, the repercussions of this damage on the dynamic interactions occurring in remote regions are only partially predicted by structural network connectivity (Alstott et al., 2009; O′Reilly et al., 2013). One other key difference between structural and functional connectivity is that while structural connections are rather stable (apart from the long-term effect of plasticity), functional connectome is non-stationary and dynamic (Park et al., 2008). Mišić and colleagues demonstrated how a particular structure topology can give rise to diverse functional network configurations (Mišić et al., 2016). This further explains why previous studies failed to obtain a one-to-one mapping between structural and functional connectome.

This comprehensive exploration of structure-function relationship extends beyond the large-scale brain network, encompassing microscale neuronal networks as well, whether using *in vitro* or *in silico* neuronal cultures (Yamamoto et al., 2018; Pernice et al., 2011; Wang, 2011; Kim & Lim, 2015). These cellular-level investigations have consistently revealed similar

findings, highlighting the profound influence of structural organization on functional network. They also suggest that given the strong interplay between functional and structural networks, estimation of functional connectivity may be a mean to infer structural connectivity (Stetter et al., 2012) Moreover, several reports on both micro- and macroscale elucidated the critical role of specific structural configurations within the network (such as hierarchical modularity and rich clubs) in the emergence of rich patterns of complex dynamics such as orchestrated synchronous activity (Feldt et al., 2011; Yamamoto et al., 2018; Reimann et al., 2017; Van Den Heuvel & Sporns, 2013). This further underscores the reciprocal influence between structure and function.

As discussed above, this structure-function relationship is complex and non-linear, yet essential to further our understanding of how the anatomical neural connectome can give rise to coherent function and rich dynamics. Numerous research endeavors set on to address the nature of this relationship. However, such enquiries fall beyond the scope of the current work. This thesis exclusively centers on the functional domain of neural networks. Nevertheless, it was vital to provide above a brief contextual understanding of the dynamic interplay between functional organization and the underlying anatomical structure in the brain and the instances of their convergence and divergence (Mišić et al., 2016).

1.3.2. Mapping structural and functional neural connections

The recent advances in network methodologies have allowed for the dissection of neural connectivity and topology, whether structural or functional, on both macro- and microscale levels. On the macroscale: structural networks are investigated using diffusion magnetic resonance imaging (dMRI) that, as the name implies, measures the diffusion of water molecules along the fatty myelinated brain fibers. This method allows for the reconstruction of presumed trajectories of axonal fibers in the brain using what is called fiber tracking or “tractography” algorithms (Hagmann et al., 2007; Iturria-Medina et al., 2008). On the other hand, several techniques are accessible for exploring functional connectivity at the macroscale, including functional magnetic resonance imaging (fMRI), electroencephalography (EEG), and magnetoencephalography (MEG) (Fornito et al., 2016). These non-invasive approaches provide a mean to quantify the functional association between brain regions by measuring their electrical activity (EEG), the magnetic signal generated by neuronal currents (MEG), or their

blood-oxygenation-level-dependent (BOLD) signal (fMRI). These methods exhibit a trade-off between spatial and temporal resolution. For example, both EEG and MEG demonstrate impressive temporal resolution, capturing measurements on a millisecond scale. However, they still suffer in terms of spatial resolution. In contrast, fMRI offer high spatial precession, making it the most commonly used tool for assessing the brain's functional connectivity, despite its relatively low temporal resolution (0.5-1.5 Hz). Ultimately, the choice of which method to utilize will hinge on the specific scientific question being investigated.

At cellular resolution, the integration of microscopic technologies, tract tracing, and genetic labelling methods offers a powerful approach to investigate structural connectivity. To map micro/mesoscale functional neuronal interactions, researchers have at their disposal optical imaging techniques using fluorescent calcium indicators or voltage-sensitive dyes, as well as electrophysiological methods like multi-electrode arrays (MEA) (Bonifazi & Massobrio, 2019; Chemla & Chavane, 2010). Similar to whole-brain imaging techniques, these cellular methods differ in the spatial and temporal resolution they provide. The choice between them again depends on the scientific questions and which level of resolution the experimenter is willing to compromise. These versatile techniques can be employed both invasively in animal models or in *in vitro* neuronal cultures, facilitating detailed investigations of functional neuronal circuitry and network dynamics.

In this study, functional networks were captured and examined using fMRI on the macroscale, and calcium imaging at the microscale. This section provides a suitable occasion to briefly introduce the mechanisms behind these techniques.

1.3.2.1. Calcium imaging: a window into neuronal activity

Calcium (Ca^{2+}) is an important intracellular messenger that plays a crucial role in the regulation of a broad spectrum of cellular processes, ranging from neurotransmitter release to regulating gene transcriptions (Grienberger & Konnerth, 2012). As such, intracellular calcium signal serves as robust indicator of cellular function, as Ca^{2+}concentrations transiently rise upon neuronal activation. In calcium imaging, this signal is measured by utilizing calcium-sensitive indicators, which can be either chemical dyes or genetically encoded proteins. When bound to free Ca^{2+} ions inside the cell, these indicators undergo conformational changes that lead to changes in their fluorescence properties. In other words, as the cell activates and experience an

influx of calcium, the calcium indicators rapidly bind to the calcium ions leading to a change in the fluorescence signal which can be picked up by optical recordings techniques. Through detecting these activity-related intracellular calcium dynamics, calcium imaging provides a mean to monitor and quantify neuronal activity across a large population of neurons, the size of which is dependent on culture density and objective magnifications.

Accordingly, Ca^{2+} imaging offers a powerful tool for examining neuronal connectivity and topology whether *in vivo* (Denk et al., 1994; Grewe et al., 2010) or in the dish (Tibau et al., 2013). However, it does suffer from some important caveats. These include low temporal resolution and low signal-to-noise ratio (Nelson & Bonner, 2021). In addition, Ca^{2+} imaging can record from dozens to thousands of neurons simultaneously at a single-cell resolution, producing challenging large datasets that call for scalable and automated analysis methods (Pnevmatikakis, 2019). Despite these methodological shortcomings, Ca^{2+} imaging continues to be a dominant method for recording neuronal activity. After segmenting active neurons in a Ca^{2+} recording and extracting their activity time courses, pairwise correlation is computed to reflect their coactivation and extract connectivity information. This information is then used to construct graphs and examine their functional topology by assessing the relevant graph metrics. The growing application of graph theory in the analysis of Ca^{2+} data holds promise for addressing pressing biological questions related to network function and connectivity (for review see Nelson & Bonner, 2021).

1.3.2.2. fMRI: the interplay between physics and biology

fMRI is one of the most commonly used techniques to acquire whole-brain network data. The impressive spatial resolution provided by fMRI together with its ease of use makes it an attractive tool for mapping functional networks. fMRI measures fluctuations in regional levels of blood oxygenation as a non-invasive method to detect the changes in neural activity. When a population of neurons activate, whether spontaneously or in response to external stimuli, their oxygen consumption increases to meet the elevated metabolic demands. This leads to an increased influx of oxygenated cerebral blood to the activated regions through vasodilation, resulting in a net decrease in deoxygenated blood. Oxygenated and deoxygenated hemoglobin have opposing magnetic properties. While oxygenated hemoglobin is “diamagnetic”, which means it is weakly repelled by the magnetic field, deoxygenated hemoglobin is weakly attracted to the magnetic field or “paramagnetic”, causing high interference with the MR signal.

This change in the ratio of oxygenated and deoxygenated blood at activated areas of the brain is what gives rise to the MR signal, where lower amounts of deoxygenated blood causes less signal distortion. The signal that measures such blood-oxygenations-level-dependent (BOLD) fluctuations is termed "the hemodynamic response".

Thus, fMRI serves as a valuable tool for capturing changes in neural activity, whether during cognitive tasks or at rest. In resting state fMRI (rs-fMRI), subjects lie quietly in the scanner without having to perform any cognitive task. Here, the BOLD signal can reveal spontaneous low-frequency fluctuations (0.01-0.08 Hz) that exhibit temporal correlation between different brain regions (Anand, Li, Wang, Gardner, & Lowe, 2007). By examining these correlations, fMRI provides insights into the brain's functional connectivity, leveraging on the premise that coactivation between two regions signifies information exchange and communication between them, thus indicating their "functionally connectivity".

Before delving into the research that has been done on the different spatial scales regarding disturbed network topology in depression, it is important to provide a concise overview of this psychiatric illness. The following introductory section encompasses its definition, etiology, and therapeutic options, serving to provide a comprehensive grasp of the complex psychiatric challenge that forms the focus of this study.

1.4. Major Depressive Disorder

1.4.1. Definition of depression

"I felt that I breathed an atmosphere of sorrow." Edgar Allan Poe

Depression is the common cold of mental disorders. It affects over 280 million people worldwide (World Health Organization [WHO], 2023) and is considered among the top ten diseased with the highest global burden (Vos et al., 2020). Furthermore, depression has been linked to a high mortality rate owing to suicidal ideation, in addition to an increased risk of comorbid conditions including anxiety disorders (Kessler et al., 2005), as well as digestive, cardiac, and cardiovascular diseases (Duman et al., 2016; Lee et al., 2015). The average age of onset in depression is around 30 years. However, cases occurring at almost any age have been reported, including adolescent depression starting at an average age of 14 years (Lewinsohn et

al., 1994) and geriatric depression occurring after the age of 60 (Brodaty et al., 2001). Women are typically twice as likely to be affected as men regardless of age group (Kessler et al., 2005).

While depression is a universal term that is usually used imprecisely to refer to a general sense of sadness or to a set of mental disorders, major depressive disorder (MDD) refers to a specific affective illness characterized by a set of cognitive, affective, and vegetative deficits. Cognitive dysfunctions include a reduced goal-directed behavior, inappropriate cognitive appraisal of negative events, and a persistent inward shift of attentional focus which gives rise to pathological rumination and over-dwelling in self-referential thoughts (Fischer et al., 2016). Affective symptoms, on the other hand, are characterized by an enduring sad mood, accompanied by a range of other manifestations. These include excessive worry, a processing bias towards negative stimuli, and altered reward and incentive processing, which can lead to amotivation and anhedonia, i.e., the inability to experience pleasure (Price & Drevets, 2012). Finally, the vegetative symptoms associated with MDD originate from disturbed autonomic and endocrine functions regulating sleep, appetite, weight, and psychomotor activity (Cheng et al., 2016). Although the neurobiological correlates of depression outlined above have been studied and characterized over several decades, the clinical definition and diagnosis of MDD continue to rely solely on the psychological and behavior symptomatology of the disorder. The Diagnostic and Statistical Manual of Mental Disorders, 5th edition (DSM-V) provides a guideline for the clinical diagnoses of MDD, in which these dysregulations are listed as nine main symptoms of depression (**Figure 6**). MDD is clinically diagnosed if the patient checks at least five out of the nine symptoms, with one of them being either depressed mode or anhedonia. For the diagnosis to be made, these symptoms should persist for more than two weeks in a way that intervene with the patient's social and occupational life, without being attributable to medical conditions or a substance abuse or being an appropriate response to grief or traumatic event (American Psychiatric Association [APA], 2013).

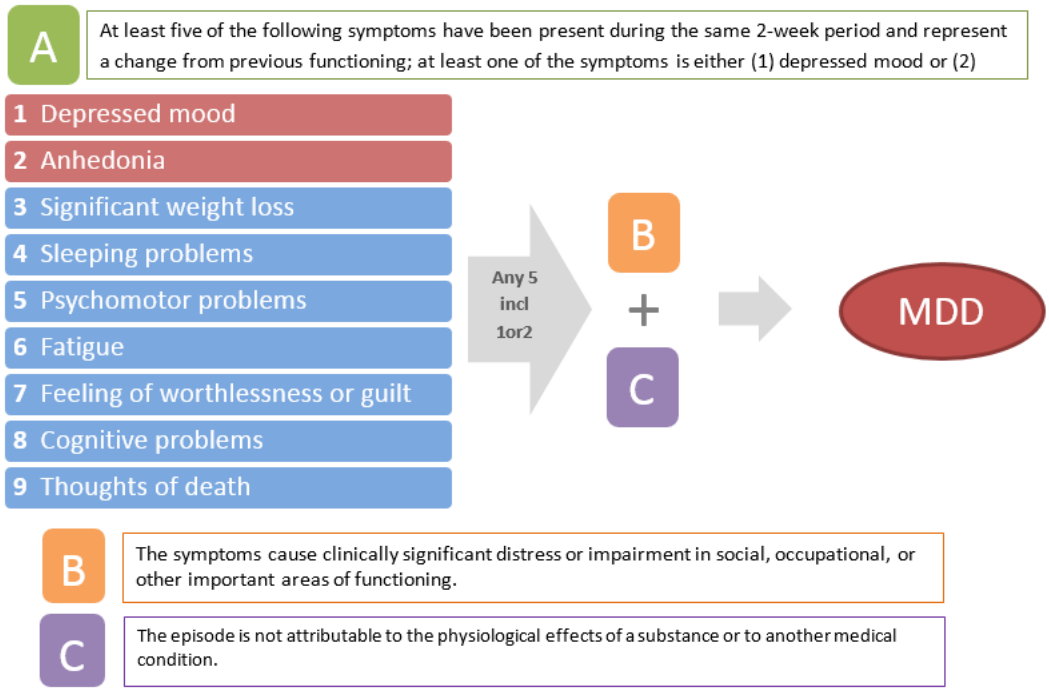

Figure 6. DSM-5 criteria for the clinical diagnosis of Major Depressive Disorder.

Depression is a complex disorder. This rather broad, unspecific definition of depression brings a substantial number of clinically different sub-phenotypes with inherently differential biological etiologies under one umbrella. The heterogeneous nature of depression has hampered the understanding of its underlying pathophysiology. For that reason, tremendous efforts are being made to delineate the neurobiological mechanisms of major depression and to identify an objective biomarker that can guide the currently unreliable clinical diagnosis. This, in consequence, would provide a solid ground for developing more effective treatment interventions with novel biological and neural targets.

1.4.2. Etiology of Depression: A Complex Interplay of Nature and Nurture

Major depression is a complex disorder with a multifactorial genesis including both genetic and environmental factors. The genetic component of MDD involves complex, polygenic variations and explains around 30-40% of the disorder's etiology (Sullivan et al., 2000). The complexity of the disorder stems from the fact that it is influenced by a relatively large number of susceptibility genes, with each having little impact on the disorder genesis. Depression arises through the interaction among these genes and/or their interaction with

environmental risk factors (Fava & Kendler, 2000). It is also possible that different combinations of vulnerability genes that contribute to depression are expressed in different individuals, which further complicates the identifications of these implicated genes (Nestler et al., 2002). Furthermore, the expression of certain genetic risk factors appears to be modulated in depression by gender and developmental phase (Kendler et al., 2001, 2006). All the aforementioned facts render isolating and identifying the chromosomal locations of susceptibility genes in depression extremely challenging (Fava & Kendler, 2000).

Nevertheless, the genetic contribution is only part of the etiological equation of depression. Environmental factors such as stress, early-life trauma, and socioeconomic adversity also play an important role in the development of this mental illness. Notably, not every stressful event will eventually lead to depression. Individuals vary in their response to the same adverse event and the risk of developing MDD is determined by genetic disposition. The precise nature of this complex interaction between the environment and genetic makeup remains an active area of research (Saveanu & Nemeroff, 2012; Nestler et al., 2002).

1.4.3. Treatment options

Several treatment approaches are now available for the management of MDD including psychotherapy, pharmacotherapy, and somatic therapy. The most commonly practiced psychotherapeutic techniques nowadays are interpersonal psychotherapy (IPT) and cognitive behavioral therapy (CBT). When used as a monotherapy, these techniques exhibit comparable efficacy to antidepressants and are associated with longer-lasting effect (Beck, 2005; Mello et al., 2005). Psychotherapy, however, is frequently used in combination with antidepressant medications, which are considered the mainstay of effective treatment of MDD.

Since the introduction of the first drug in the mid-fifties, several antidepressant medications have been developed and approved for the treatment of MDD. These antidepressants share their effect on the monoaminergic (neurotransmission) system and are classified based on their target monoamine synaptic receptors and/or monoamine transporters (Otte et al., 2016). The main antidepressant classes include: tricyclic antidepressants (TCAs), monoamine oxidase inhibitors (MAOIs), selective serotonin reuptake inhibitors (SSRIs), norepinephrine reuptake inhibitors (NRIs), serotonin-norepinephrine reuptake inhibitors

(SNRIs), and finally, noradrenergic and specific serotonergic antidepressants (NASSAs). These drugs share a common effect of elevating monoamines concentrations at the synaptic cleft. However, they differ in their affinity to the various monoamine receptors, and therefore in their efficacy, tolerability and side effect profile (Cipriani et al., 2009). The effect of these drugs supports the monoamine hypothesis of depression that suggests a link between the pathophysiology of MDD and a catecholamine-deficiency in the brain (catecholamine including: noradrenaline, serotonin, and/or dopamine) (Schildkraut, 1965).

However, recent studies have identified several other systems that are implicated in MDD and can serve as novel targets for antidepressant development. The hypothalamic-pituitary-adrenal (HPA) axis is one such system, with drugs that modulate this system showing potential antidepressant effects such as corticotrophin-releasing hormone (CRH) antagonists (Cowen, 2010). Additionally, The acute antidepressant effect of ketamine, the N-methyl-D-aspartate glutamate receptor antagonist (NMDA), has proposed a role of glutamate and γ-aminobutyric acid (GABA) in mood regulation (Berman et al., 2000). The antimuscarinic agent scopolamine has also shown a rapid antidepressant effect, highlighting the hyperactive cholinergic system as a potential target for MDD treatment (Jaffe et al., 2013). Another system of interest is the melatonin system that can be targeted using the melatonin receptor agonist agomelatine, which has demonstrated therapeutic benefit in treating depression (S. H. Kennedy & Emsley, 2006).

Despite the various treatment options available on the market today, depression treatment remains suboptimal. It is true that antidepressants offer substantial benefit for depression patients and up to 80% of patients manage to achieve partial responses. However, only around half of MDD patients show a complete remission (Nestler et al., 2002). Relapse and treatment resistance are still two major problems in MDD therapy. In addition, most antidepressants have delayed onset of action, extending to over three weeks, which can further complicate the treatment process and be an added strain for patients, especially those experiencing suicidal thoughts (Stassen & Angst, 1998). Tolerability is another crucial issue and is often used as a basis for prescribing of antidepressants (Penn & Tracy, 2012).

When two or more adequate treatment trails (in terms of duration and dosage) of different classes of antidepressants fail to achieve response in a current episode, the case is considered a treatment-resistant depression (TRD) (Ruhé et al., 2011). 20-30% of MDD patients remain

at risk of developing TRD and are then candidates for neuromodulatory somatic therapy such as electroconvulsive therapy (ECT), transcranial magnetic stimulation (TMS), vagus nerve stimulation (VNS), and deep brain stimulation (DBS) (Cusin & Dougherty, 2012). These physical techniques work by stimulating the brain to reestablish homeostasis in neural circuits that are usually dysregulated in depression (S. H. Kennedy & Giacobbe, 2007).

In summary, the current state of depression treatment is found on a slippery ground. This state of uncertainty is presumably due to an incomplete understanding of the underlying pathophysiology of depression as a mental illness and the inherent heterogeneity rooted in its broad clinical definition. One other reason is the limited knowledge we have concerning the exact mechanism of action of antidepressants as they evidently modulate neurophysiological targets and cause adaptive changes that work beyond their direct molecular mechanism of increasing monoamine levels. The alarming rates of relapse and treatment resistance in depression not only highlight the suboptimal treatment process but also underscores our limited understanding of the disorder's etiology and mechanisms. Examining the brain on a network level provides a new perspective to understand its complex function and how this function can go awry in face of a challenging environment. This level of understanding can be further deepened by addressing these network-related questions at a multiscale level, ultimately identifying new therapeutic targets and optimizing the so far suboptimal diagnostic and prescribing procedure.

1.5. State of the art: Disturbed functional topology in depression

A large body of evidence has demonstrated that depression, among other psychiatric illnesses, is a disorder of disrupted neuronal circuits rather than a localized dysfunction in a discrete brain region, which could fairly explain this disorder's complexity (J. P. Hamilton et al., 2013; J. L. Price & Drevets, 2012; L. Wang et al., 2012; Zeng et al., 2012). This led to the reconceptualizing of MDD as a complex network disorder in which connectivity is disturbed. This connectivity is postulated to be governed by a specific set of topological rules, and it is deviations from these fundamental principles of large-scale brain network organization that underlies the behavioral and physical dysfunctions observed in depression (van den Heuvel & Sporns, 2019). Clinical network neuroscience offers a conceptual basis and analytical tools to study topological network alterations in MDD. Identifying such alterations is key for

establishing network-based biomarkers that would aid in the currently suboptimal diagnostic and therapeutic procedure of depression (for review, see Lydon-Staley & Bassett, 2018).

As discussed in the previous section, addressing network alterations on a multiscale level is crucial for gaining deeper insight into the pathological effects of MDD on network organization. Yet, no multiscale studies in the context of topological network dysfunction in MDD are available at the time of writing this thesis. Most of the evidence for disrupted functional network topology in depression originates from macroscale, whole-brain imaging studies using fMRI and EEG data (see literature review below). Studies linking dysfunctional topology to depression at the cellular level are lacking, likely due to the absence of a suitable human cellular model. This section reviews the body of MDD-related research conducted at each of these special scales individually (micro and macro) and present the efforts made to employ iPSC-derived cellular models for dissecting MDD and antidepressants mechanisms.

1.5.1. On the microscale

Until recently, methods available for modeling psychiatric illnesses preclinically were limited to animal models and postmortem analyses of brain tissue. Both approaches, albeit informative, fail to recapitulate the complexity and heterogeneity of psychiatric disorders. Moreover, these methods inherently lack a vital key to understanding and dissecting cellular mechanisms of human psychopathologies: an access to a viable, functioning human tissue (Colpo & Teixeira, 2021; Wang et al., 2020).

Animal models have been subject to scrutiny when used for “mental” illnesses such as MDD. The absence of objective biomarkers for depression coupled with the phenotype-based diagnosis present a challenge in accurately relating and validating the disorder’s phenomenology to animal models. This is mainly attributed to the subjective nature of many of the MDD-associated symptoms, e.g., sadness and guilt. It is true that behavioral correlates of these symptoms can be observed in animals (such as abnormal social behavior, motivation, and working memory, among others), yet linking such behavior to the subjective emotional symptoms of the disorder can only be approximate. Moreover, although animals and humans share certain biological processes, notable distinctions in gene expression and regulation exist, contributing to inherent variations in physiology (Barré-Sinoussi & Montagutelli, 2015; Cardoso-Moreira et al., 2020). Furthermore, the heterogeneity of some mental disorders like

MDD rooted in the vague symptom-based diagnostic boarders (discussed earlier) poses extreme challenges for the development and validation of animal models. While animal models continue to provide insights into the complex networks abnormalities underling psychopathologies, it is important to address their findings with caution, recognizing their limited capacity to fully capture the breadth of DSM-defined psychiatric disorders (Nestler & Hyman, 2010). Similarly, the analysis of postmortem tissues has its own limitations in modelling mental illness, despite it providing a window into diseased human tissues. For example, postmortem tissues are unable to reveal the early complex dynamic cellular changes that drove the development of the disorder, offering only a limited prospect of the disease end-point (Wang et al., 2020).

The introduction of human induced pluripotent stem cells (hiPSCs) technology (Takahashi et al., 2007) helped overcome these aforementioned hurdles and opened up new avenues in psychiatric disease modeling and drug discovery (Soliman et al., 2017). The iPSC technology offers a great advantage over the use of embryonic stem cells (ESCs) as it allows derivation from readily available adults cells, providing disease-relevant, patient-specific viable neuronal cultures accessible for investigation (Bardy et al., 2020; Soliman et al., 2017). With this technique, mature human somatic cells can be reprogrammed into adult stem cells with a set of just four transcription factors. The regained pluripotency allows for the stem cells to adopt a neuronal fate while preserving the genetic makeup of the donor cells. This makes iPSC technology particularly useful for modeling diseases with strong genetic components such as MDD, where complex, polygenic variations account for 30-40% of the disorder etiology (Sullivan et al., 2000; Shadrina et al., 2018; Wray et al., 2018). Epigenetic modifications, however, occurring in depression as a result of various environmental risk factors such as stress, early-life trauma, and medications, are normally erased after several cell divisions of fibroblasts (Garbett et al., 2015) and upon the reprogramming procedure (Soliman et al., 2017). This might pose a challenge when modelling disorders such as depression where the influence of environmental factors plays a significant role in the disorder’s etiology.

iPSCs have been successfully used to model complex neurological and psychiatric disorders such as schizophrenia (Brennand et al., 2011), bipolar disorder (Mertens et al., 2015, O'Shea et al., 2016), autism spectrum disorder (ASD) (DeRosa et al., 2012), and Parkinson’s disease (Kikuchi et al., 2017). In the realm of depression research, two distinct research teams

have established effective protocols for generating serotonergic neurons from iPSCs. This provided a platform for investigating dysfunctions specific to serotonergic system, including those related to depression (Xu et al., 2016; Vadodaria et al., 2016). Vadodaria et al. later employed their iPSC-derived model and examined the cellular mechanism underlying SSRI-resistance (Vadodaria et al., 2019a). They compared serotonergic responses and neural activity in *in vitro* neuronal cultures derived from SSRI-remitters and SSRI-non-remitters depression patients. They observed a serotonin induced hyperactivity downstream of the upregulated excitatory serotonergic receptors in the neurons of the non-remitter cohort. In another study, they revealed no differences in serotonin-related genes but showed significantly lower expression of genes regulating neuronal growth and morphology in the non-remitters group compared to remitters and healthy controls (Vadodaria et al., 2019b). This suggested that inherent differences in neurite growth and morphology might contribute to SSRI-resistance in depression and have serious consequences on the structure and function of neural circuits.

Another group examined the involvement of mitochondrial dysfunction in the etiology of depression. They reported altered energy metabolism and impaired mitochondrial function in both fibroblasts and neural progenitor cells (NPCs) of depressed patients (Kuffner et al., 2020; Triebelhorn et al., 2022). This disturbed bioenergetic activity was evident by reduced oxygen consumption rates and mitochondrial membrane potential in patient-derived fibroblasts (Kuffner et al., 2020). Similar reduction was also observed in respiration, cytosolic Ca^{2+} levels, and cell size of NPCs (Triebelhorn et al., 2022). Furthermore, the group also generated iPSC-neurons in which they observed a less negative resting membrane potential in MDD patient-derived neurons compared to healthy controls. They also reported reduced membrane capacitance of patient-derived neurons indicative of diminished neuronal cell size, the finding that was consistent with the smaller cell size they observed in patients-derived NPCs.

Human iPSCs derived from healthy donors have been employed in several studies to elucidate the acute antidepressant mechanism of ketamine, specifically in dopaminergic neurons which are known to be involved in depression's core symptom, anhedonia (Cavalleri et al., 2018; Collo & Merlo Pich, 2018; Collo et al., 2018, 2019). These reports, generated by the same research group, emphasized the role of ketamine in driving structural neuroplasticity in dopaminergic neuronal cultures. This role was mediated by activating specific downstream intracellular pathways. These pathways involve α-amino-3-hydroxy-5-methyl-4-

isoxazolepropionic acid (AMPA) receptors and brain-derived neurotrophic factor (BDNF), ultimately leading to the activation of the mammalian target of rapamycin (mTOR), which is associated with cell growth and survival. Other groups used human iPSC models derived from healthy subjects to explore either the antidepressive mechanism of fibroblast growth factor 2 (FGF2) (Gupta et al., 2018), or the neurotoxicity of certain antidepressants (Huang et al., 2017; Pei et al., 2016)

While the body of research exploring the cellular mechanisms of MDD and antidepressants using human iPSC models is expanding steadily, the application of this technique to investigate alterations in functional network architecture on the microscale and how they might contribute to the disorder remain unexplored thus far. The only evidence for disturbed functional organization at the microscale in depression stems from a recent study conducted on dissociated hippocampal neuronal culture in healthy rats. Trepl et al (2022) examined the effect of various antidepressants on large-scale network wiring, revealing reduced number of connections and E_{glob}, as well as increased local clustering in the treated cultures. However, it is important to consider the limitations of this study, including the use of healthy (animal) neural tissues on which antidepressant might have little or atypical effect, and the restricted effect of antidepressants on a specific neural tissue (hippocampal). Nonetheless, these results underscore the implication of functional network organization in the underlying mechanism of antidepressant action, thereby prompting a need for further explorations in this particular direction.

1.5.2. On the macroscale

1.5.2.1. Global functional network alterations

Several brain imaging studies using rs-fMRI have investigated changes in functional network organization in MDD and their effect on the essential integration-segregation balance. The findings of these investigations, however, remain inconsistent. For example, Zhang et al, showed a topological shift toward randomization in functional brain networks of untreated patients with first episode MDD compared to controls, as was evident by increased E_{glob} and decreased path lengths in whole-brain networks of the patients cohort (Zhang et al., 2011). Meng et al, on the other hand observed an opposite pattern in depressed patients (decreased E_{glob}), although small-world topology and C did not differ from healthy controls (Meng et al.,

2014). Unlike Zhang et al., Meng and colleagues recruited patient with recurrent major depression who were treated with antidepressants. This difference in medication status might be one reason behind these varying results. Two additional investigations did not reported any significant depression-related changes in these global measures of functional topology (Bohr et al., 2013; Lord et al., 2012).

Two other studies explored whole-brain functional network topology alterations in first-episode, medication-naive adolescent MDD patients (Jin et al., 2011; Wu et al., 2020). Both investigations reported a general departure from small-worldness in MDD patient compared to their healthy cohort. More specifically, Wu et al. observed topological aberration consisting with those reported by Zhang, where depressed patients showed lower *C* and higher integration efficiency (Wu et al., 2020). Integration and segregation topological features were also examined in late-life depression by Li and colleagues (Li et al., 2015). Their results indicated a lower integration (reduced E_{glob}) accompanied by a lower segregation (reduced E_{loc}) in depressed patients with and without cognitive impairment compared to healthy subjects. Notably, the observed reduction in small-world measures in this study was associated with higher depressive symptom severity in the depressed group irrespective of the cognitive status.

An important factor contributing to the inconsistency of these findings is the substantial heterogeneity present within the patient sample across the studies. Certain investigations included patients that varied in terms of their age, clinical characteristics, number of depressive episodes, and/or treatment status. Additional factors involve differences across studies is the definition of nodes and the choice of brain parcellation, two key aspects that typically dictate the final graph structure and thus the graph measures (Wang et al., 2009; Zalesky et al., 2010). Furthermore, variations in motion artifacts and how the data were preprocessed may further contribute to the incongruences observed in the results (Liang et al., 2012).

1.5.2.2. Subnetwork-specific and nodal alterations in functional organization

The brain's capacity to segregate and establish functionally specialized modules offers an intriguing avenue for examining module-specific topological changes and their potential implication in the cognitive and affective dysfunction associated with depression. Furthermore, exploring nodal topological characteristics of various brain regions, particularly in terms of their degree and centrality is of interest to inspect how the psychopathy affect these regions'

influence in the network. In fact, frequent reports have highlighted the aberrant connectivity patterns within three specific modules or subnetworks that consistently feature in depression research: the default mode network (DMN), the cognitive control network (CCN), and the salience network (SN). The DMN encompasses spatially remote regions spanning the medial prefrontal cortex (MPFC), inferior parietal lobules (IPLs), posterior cingulate cortex (PCC), and the precuneus (Raichle et al., 2001). It is believed to mediate self-referential thoughts and introspective processing involved in "mind wandering". As a result, DMN is typically activated at rest and deactivated during the performance of cognitive tasks. In contrast, CCN, alternatively referred to as frontoparietal network (FPN), activates during tasks and deactivate at rest. It supports executive functions and goal-directed behavior as well as decision making processes (Sheline et al., 2010). CCN is structurally composed of lateral frontal regions including the dorsolateral prefrontal cortex (DLPFC), dorsal anterior cingulate cortex (ACC), and posterior parietal cortex. SN constitutes a mesocortico-limbic network responsible for processing affective stimuli and regulating emotions and behavior. Core regions of the SN include cortical areas such as orbitofrontal cortex (OFC), ventral frontal cortex (VFC), and limbic structures of the ACC (subgenual ACC), together with limbic regions like the ventral striatum and nucleus accumbens. Depression-related dysfunctions and altered connectivity patterns within and between these distinct functional brain networks maps well onto core symptoms of depression. For instance, rumination correlates with the DMN (Hamilton et al., 2011; Fischer et al., 2016), attention deficits and reduced concentration are closely linked to the CCN (Alexopoulos et al., 2012; Kaiser et al., 2015), and anhedonia and amotivation are associated with the aberrations in the SN.

On the nodal level, Zhang et al. showed reduced regional connectivity and integration in the DLPFC, measured by *degree*, *efficiency*, and *betweenness centrality* (Zhang et al., 2011). The DLPFC is a core region of the CCN that supports mood regulation and other cognitive function. DLPFC altered connectivity has been frequently reported to play a critical role in the pathophysiology of depression (Bae et al., 2006; Sheline et al., 2010). In addition to the observed overall reduction in small-worldness, Jin and colleagues (2011) also reported a higher functional node degree in first-episode adolescent depressed patients in several regions of the DMN, including areas of prefrontal cortex (PFC) (ACC, dorsolateral, medial, and inferior PFC) and in insula and the amygdala. They also reported a positive correlation between the amygdala's degree and the depression duration. Similar results were reported in the study of

Wu et al. (2020) that included a similar cohort of adolescent patients. The increased nodal centrality reported in their work also involved the hippocampus and the parahippocampal gyrus, while regions in the orbitofrontal, temporal, and occipital cortex showed decreased centrality. However, a contrasting pattern of DMN topology was found in remitted geriatric depression (RGD) patients (Zhu et al., 2018). In this study, the DMN of RGD patients exhibited lower E_{glob} and increased path length compared to controls, implying a less optimal network integration in RGD. They also investigated several regions of the posterior part of the DMN and showed decreased functional connectivity in PCC, precuneus, angular gyrus, and middle temporal gyrus.

Depression-related topological changes were also reported in different regions of the striatum, a subcortical system related to the SN and implicated in regulating emotional processes and reward-related responses (Meng et al., 2014; Robinson et al., 2012). Putamen and the nucleus accumbens of the striatum exhibited increased nodal degree and centrality in MDD, which positively correlated with the number of depressive episodes. This correlation was independent of current depressive symptoms, medication status, or disease duration, suggesting a link between striatum connectivity and the course of the disorder and its relapse (Meng et al., 2014). Similarly, Ye et al. (2016) also reported increased nodal efficiency in many limbic regions regulating mood and affective processing, together with decreased nodal efficiency in regions of cognitive control such as DLPFC and ACC. This is consistent with prior findings that related pathophysiology of depression to a breakdown in the cortico-limbic network (Price & Drevets, 2012). The corticolimbic model of depression suggests decreased cortical and increased limbic activity as well as connectivity. This translates into a loss of top-down regulation by the higher-order cortical areas (the regulatory system) over the mood related limbic structure (the affective system) (Price & Drevets, 2012). This pattern of abnormal cooperation between the two systems was observed and reported in several neuroimaging studies (Delaveau et al., 2011; Drevets et al., 2008).

Together, these rs-MRI studies reveale a global topological aberration in macroscale brain network in individuals with MDD. Besides, they underscore the significance of hub regions within major large-scale brain networks in the disorder's mechanism and provide insights into how their altered topology is linked to the resultant cognitive deficit and behavioral abnormalities. This region-specific information is highly important when considering novel

therapeutic targets in depression, e.g., potential target regions for TMS. However, the inconsistency among the findings of these reports necessitates further validation, preferably with consistent data preprocessing and analysis strategies. It is also worth noting the above reviewed literature primarily addresses abnormalities in functional topology in the resting brain in the absent of a cognitive task. Aberrant functional connectivity in depression patients performing cognitive or emotional tasks was reported in a number of studies (Frodl et al., 2010; Versace et al., 2010), yet similar investigation on network topology is lacking. Examining topological alterations during task performance is crucial to better understand the depression-related network effect on cognition and mood.

1.6. Aim of the study

Based on the stated literature, the distinct spatial scales of nervous system organization are highly interdependent and the changes on one scale could influence changes on the other. However, how this micro-macro relationship of network topology manifest in psychopathologies such as MDD is still a scarcely investigated area. Despite the wealth of research linking MDD to abnormal network communication, there is little evidence available on how functional network topology is affected by this disorder. While empirical findings from whole-brain studies on network topology in depression remain inconclusive, research conducted at the microscale is unavailable altogether. Such cross-scale information is essential to better elucidate the fundamentals of neural network communication and how they map across scales. Answering such a multiscale question is crucial to shed new light on the biological mechanisms underlying MDD pathological processes and how they map across scales affecting cognition and behavior.

Here, we set out to investigate whether MDD patients and their age- and sex-matched healthy controls differ in graph theoretical measures of integration and segregation and overall node connections at two levels of spatial organization: cellular and systems. Furthermore, our objective was to assess whether such differences are consistent between the micro and macro levels. Functional networks were modelled and probed using iPSC technology and calcium imaging on the microscale, cellular level, and fMRI on the macroscale, systems level. We employed graph theory analysis to examine features of functional network topology at both scales. Additionally, a key aim of this research was to pinpoint specific brain regions exhibiting differences in their functional topological properties in MDD, including properties of *efficiency* and *centrality*. Ultimately, this project aims to establish an integrative framework to study the cross-scale effect of depression on neural network organization. It does so by piecing together data describing multiple levels of brain organization to better understand brain function in both health and disease.

Chapter 2. Materials and Methods

2.1. On the microscale

2.1.1. Participants and behavioral assessment

Skin biopsies were collected from 9 MDD patients and 9 age- and gender-matched healthy controls by the Department of Dermatology, University Hospital of Regensburg, Regensburg, Germany. Patient donated skin biopsies at the end of their hospital stay after receiving antidepressant treatment. A written informed consent was obtained from all participants, and the study was approved by the ethics committee of the University of Regensburg (ref: 13-101-0271). The diagnosis of MDD was made based on the ICD10 (WHO, 1993). The 21-item Hamilton Rating Scale for Depression ($HAMD_{21}$) (Hamilton, 1960) was used to rate depression severity in the MDD group at hospital admission and to confirm the absence of depression symptoms in control groups. The $HAMD_{21}$ scale is comprised of 21 items, each is a multiple-choice question examining a distinct symptom of MDD with 3-5 possible responses that increase in severity. The $HAMD_{21}$ ratings are determined by a clinician during a clinical interview based on the clinical observations reported by the patient. This final $HAMD_{21}$ score reflects the presence and severity of the depressive disorder as depicted in **Table 1**.

Total $HAMD_{21}$ Score	**Depression Level**
0-9	Normal (no depression)
10-20	Mild depression
21-30	Moderate depression
> 30	Severe depression

Table 1. $HAMD_{21}$ cut-off scores. $HAMD_{12}$: The 21-item Hamilton Rating Scale for Depression

2.1.2. Cultivating primary human fibroblasts and generating hiPSCs

The obtained human fibroblasts were subsequently cultured, frozen until later use, and then thawed as described in Kuffner et al. (2020). Human iPSCs were generated with episomal plasmid vectors (Okita et al., 2011) as reported in Triebelhorn et al. (2022). Quality assessment of the pluripotency of the generated iPSC was performed using the PluriTest® assay adjusted for next-generation sequencing (NGS) data (Schulze et al., 2015).

2.1.3. Generating and culturing of hiPSC-derived neural progenitor cells (NPCs)

The generated hiPSCs were differentiated into NPCs in accordance with the derivation protocol outlined in the work of Yan et al. (2013). NPCs cultures were subsequently cultivated and expanded as described in the following sections.

2.1.3.1. NPCs seeding

NPCs were seeded onto Matrigel-coated dishes, ensuring the maintenance of cells in a healthy and undifferentiated state (Hughes et al., 2010). Matrigel (Corning Incorporated), stored at -80 °C, was thawed on ice to prevent its polymerization (typically occurring at 10 °C). It was then resuspended in cold DMEM/F12 (Dulbecco's Modified Eagle Medium/Nutrient Mixture F-12) (Gibco by Life Technologies) and applied to pre-cooled 6-well plates (1 ml per well) to yield a final concentration of 8 µg/cm2. The coated plates were then incubated for 30-60 min at 37 °C and subsequently washed with 1ml/well F12 before plating the NPCs. If the plates were not intended for immediate use, a 1:1 ratio of DMEM/F12 was added and the plates were carefully sealed with Parafilm to prevent evaporation and stored at 4 °C for a maximum duration of 7 day.

2.1.3.2. NPCs passaging

NPCs were cultivated in a neural expansion medium (NEM) (49.5% Neurobasal medium (Gibco by Life Technologies), 49.5% Advanced DMEM/F12 media, and 1% neural induction supplement (Life Technologies)). NEM medium was changed every two days until the cell culture reached 80-90% confluency. NPCs were passaged roughly once every 7-10 days. The passaging procedure of NPCs was commenced by first dissociating the cells using 500 µl

prewarmed Accutase (StemCell Technologies) per well and incubating for 3 min at 37 °C. After that, 1 ml of prewarmed F12 was added per well to stop the proteolytic enzyme activity of Accutase and prevent its toxicity. The cells were then harvested with 5 ml of prewarmed F12 medium and centrifuged the cell suspension at 800 rpm for 5 min. Cell counting was performed using trypan blue dye and a Neubauer counting chamber. After another round of centrifugation, 2 x 10^6 cells were resuspended in 2 ml of NEM and seeded in each well of a Matrigel-coated plates. The plates were then carefully moved in an "figure-eight" movement to ensure a homogeneous cell distribution and adhesion on the plates after seeding, and were incubated over night at 37°C. On the following day, the NEM media was changed to remove any remaining traces of Accutase.

2.1.3.3. NPCs freezing and thawing

For cryopreservation of NPCs, 7-10 x 10^6 cells were centrifuged at 800 rpm for 5 minutes. After removal of the supernatant, 1 ml of cold STEMdiff™ Neural Progenitor Freezing medium (StemCell Technologies) was carefully added to the cell pallet. Subsequently, the cell pallet was transformed together with the freezing medium to a cryovial and swiftly moved into a freezing container with 2-propanol to ensure a gradual temperature decrease (-1 °C/min) and thus a consistent freezing profile. The containers were stored at -80 °C overnight and the next day the cryovials were taken out of the freezing containers. For extended storage, the vials were kept at -196 °C in a liquid nitrogen tank.

To thaw NPCs, the cryovial was subjected to a 3-minute incubation in a 37 °C water bath. Subsequently, the cell pallet was resuspended and transformed into a 15 ml falcon tube. 5 ml prewarmed F12 was added for washing purposes and the falcon was centrifuged at 800 rpm for 5 min. After the removal of the supernatant, the resultant pallet was resuspended in 2 ml NEM and seeded the cell suspension onto prewarmed Matrigel-coated plates. The plates were then incubated at 37 °C overnight. On the following day, the NEM was changed to eliminate any residual freezing medium. Subsequent medium change was carried out every 2-3 day, taking into account the cell density in the dish.

2.1.4. Differentiation of NPCs into human induced neurons (iNeurons)

NPCs intended for differentiation were plated on ibidi dishes (Ibidi GmbH, Germany) coated with poly-L-ornithine (PLO) (Sigma-Aldrich) and laminin (Sigma-Aldrich). PLO facilitates optimal cellular adhesion by positively charging the surface, thereby enhancing the binding of negatively charged glycoproteins expressed by neurons (Mazia et al., 1975). On the other hand, laminin assumes a pivotal role as an extracellular matrix molecule that promotes the generation, expansion, and differentiation of neural progenitors into neurons and stimulate neurite outgrowth (Ma et al., 2008). The coating procedure involved diluting PLO in Phosphate Buffered Saline (PBS) to a concentration of 15 µg/ml and adding 1 ml of that solution to each ibidi dish (1 ml/4 cm^2) and distribute it with a an 8-shaped movement. The dishes were incubated overnight (or for a minimum period of 4 hours) at 37 °C, or stored at 4 °C for weeks if not used immediately. Next, the dishes were coated with laminin by replacing the PLO coating solution in each ibidi dish with a solution containing 20 µg of laminin in 1 ml of Advanced DMEM/F12. This ensured a laminin concentration of 5 µg/cm^2, covering an area of 4.1 cm^2 per dish.

The differentiation of NPCs to neurons was specifically carried out using cells from passages 5-10 to insure their complete maturation and optimal health. At the end of the passaging procedure, 3 x 10^5 NPCs were centrifuged and resuspended in 400 µl NEM per dish and seeded on the growth area (3.5 cm^2) of the PLO/laminin-coated ibidi dishes.

Following seeding of NPCs on coated ibidi dishes, the cells were incubated at 37 °C overnight to allow for full attachment and cell division. When a confluency of about 70% was achieved, typically occurring after 24 h of seeding, the differentiation process were initiated by washing off NEM and culturing the cells in 400 µl neuronal differentiation medium (NDM) (1% B27+ supplement (Life technologies), 0.5% GlutaMax (Life Technologies), 0.5% non-essential amino acids, 0.5% Culture One supplement (Thermo Fisher Scientific), 200 nM ascorbic acid (Carl Roth), 20 ng/ml BDNF (PeproTech), 20 ng/ml GDNF (PeproTech), 1 mM dibutyryl-cAMP (StemCell Technologies), 4 µg/ml laminin (Sigma), 50 U/ml Penicillin (Thermo Fisher Scientific), 50 µg/ml Streptomycin (Thermo Fisher Scientific) in Neurobasal Plus medium (Thermo Fisher Scientific)). Half of NDM was changed every other day by removing 200 µl and slowly adding another 200 µl of fresh NDM. To suppress the growth of

other differentiating, non-neuronal cells, the iNeuron cultures were treated with Cytosine arabinoside (Ara-C or Cytarabine), a pyrimidine antimetabolite that directly inhibits DNA replication. Ara-C was added at 6 days *in vitro* (DIV) following differentiation by removing NDM and adding another 400 µl of NDM containing 1 µM of Ara-C. Ara-C-containing NDM was replaced the following day with fresh NDM to prevent potential Ara-C toxicity. Cultures of mature neurons were obtained at 21 DIV and were ready for imaging (Figure 7A).

To ensure results reliability and to boost statistical power, three different iNeuron cultures stemming from different NPCs passages were prepared for each subject's iPS cell line. These cultures served as biological replicates.

2.1.5. Microscopy and Calcium imaging

Calcium imaging was employed to detect and record spontaneous neural activity of *in vitro* neuronal network. The ratiometric calcium indicator Fura-2/AM (Gibco by Life Technologies) was used to monitor changes in the cytosolic free calcium. The acetoxymethyl (AM) ester group renders the fluorescent dye membrane-permeable and is removed by cellular esterases once inside the cell, trapping the dye intracellularly. Fura-2 has an excitation spectrum/peak at 380 nm in its free form. Upon binding free cytosolic Ca^{2+} ions, Fura-2 undergoes conformation change resulting in an excitation shift from 380 nm to 340 nm (with maintaining the same emission wavelength at 510 nm). Thus, cellular Ca^{2+} dynamics, and therefore neural activity, can be determined using the Fura-2 by measuring fluorescence intensity induced at the two wavelength 340 nm and 380 nm and emitted at 510 nm. The intensity ratio 340/380 is then calculated to indicate cytosolic Ca^{2+} dynamics.

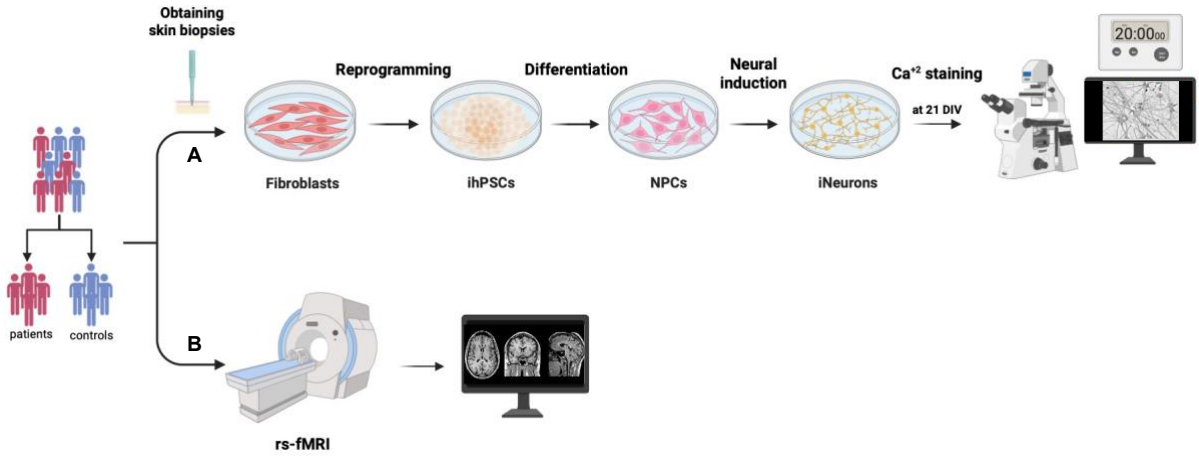

Figure 7. developing a human cellular model and whole-brain, large-scale model to probe network topology in depression. (A) Generating a pluripotent stem cell (iPSC)-based cellular model for depression. Skin biopsies were collected from 9 depressed patients and their matched healthy subjects. Fibroblasts were cultured and reprogrammed into iPSCs and subsequently differentiated into neuronal lineage to NPCs. NPCs were then induced into fully developed neurons, so-called "induced neurons" (iNeurons). At 21 DIV, the cultured neurons were stained with calcium sensitive florescent dye (Fura-2/AM) and collected 20-minute-recordings of their spontaneous activity under the microscope by means of calcium imaging. (B) generating a large-scale brain network human model. Seven patients and seven matched controls from the cohorts that donated skin biopsies were recruited for an MRI session. Functional MR images were collected in a 20-min resting-state (rs-fMRI) scanning session in the absence of any cognitive task. Functional brain images were later used to explore functional network topology at the systems level in depression. iPSCs: induced pluripotent stem cells, NPCs: neural progenitor cells, iNeurons: induced neurons, DIV: days *in vitro*, rs-fMRI: resting-state functional magnetic resonance imaging.

In practice, the neuronal cell cultures were loaded with a solution of Fura-2/AM (2 μM, Gibco by Life Technologies) and 10% Pluronic-F127 (1:1) (Thermo Fisher Scientific) in Opti-MEM solution (Gibco by Life Technologies) and incubated at 37 ℃ for 30 minutes. After the incubation period, the cells were subjected to three consecutive washes, each involving 500 μl of glucose-containing Ringer's solution. The fourth volume of the solution was retained on the cultures, rendering them ready for the subsequent imaging process.

The cultures were then examined with an observer.Z1 inverted fluorescence microscope equipped with a Fluar 20x/0.75 objective and an AxioCam MRm CCD camera (ZEISS, Jena, Germany). Fura2-loaded cell cultures were excited with ultraviolet light at wavelengths of 340 and 380 nm (BP 340/30 HE, BP 387/15 HE) using a fast wavelength switching and excitation device (Lambda DG-4, Sutter Instrument), and fluorescence signal at 510 nm was captured (BP 510/90 HE and FT 409). Zen imaging software (ZEISS) was applied to control the hardware and capture a 20-minute-long recording of spontaneous neural activity for each dish. The recordings were acquired at a 1.89 Hz rate, resulting in 2265 frames/images of size 272x208 pixels (438.736x335.504 μm). It is worth noting that in our sample, Ca^{2+} imaging recordings

of 2 patients and their corresponding controls were collected for another project at a different acquisition rate (0.5 Hz) resulting in a different frame count (1200 frames). While a lower sampling rate can potentially inflate pairwise correlations between time courses, it is crucial to emphasize that the inclusion of these 4 subjects in the analysis does not introduce bias to our comparison between patients and controls. This is due to that fact that both groups have an equal number of datasets that are impacted by the reduction in sampling rate, ensuring an unbiased comparison between the group. For each image in a recording, the Ca^{2+} signal was expressed as the 340/380 fluorescence intensity ratio (indicating the bound/free Ca^{2+} ratio), which was computed using the *ImageJ* plugin "Ratio_Plus" (Magalhães, 2003, Schneider et al., 2012).

2.1.6. Motion correction and segmentation

The preprocessing and segmentations of Ca^{2+} recordings were conducted in MATLAB R2020b (The MathWorks Inc, Natick, MA, USA). Correcting for motion artifacts was carried out by aligning the images within each video using the Non-Rigid Motion Correction (NoRMCORRE) software (Pnevmatikakis & Giovannucci, 2017) (Figure 8A). To eliminate distortions introduced by motion correction, a 2-pixel margin was removed from all video edges. Subsequently, a correlation image was generated for each motion-corrected video. This was accomplished by computing the average temporal correlation of each pixel's activity with that of its nearest 4 neighbors (Smith & Häusser, 2010). This image serves as a summary image that aids the subsequent segmentation process by enhancing active neurons while suppressing uncorrelated neuropil noise (Giovannucci et al., 2019). Next, a segmentation pipeline was designed in CellProfiler (McQuin et al., 2018; Stirling et al., 2021) to generate binary mask images corresponding to each correlation image. These masks outline the boundaries of all neurons in the correlation image, including both active and non-active ones. Similar to the trimming applied to the recordings, the masks produced by CellProfiler were also trimmed to ensure consistent sizes, and cell boundaries were identified and cells were labeled in the binary masks. We then segmented active neurons in each recording as regions of interests (ROIs) by implementing an intensity-thresholding based workflow programmed in MATLAB (Figure 8A). First, each video was spatially smoothed with an 8-pixel Gaussian kernel to mitigate spatially distributed noise, consequently enabling smoother time courses. Then, we normalized the data and computed Z-scores across the temporal dimension. Subsequently, we computed

the frame-wise maximum Z-score and chose the smallest of these values as the threshold above which we considered a pixel to represent neuronal activity. Additionally, we established a size criterion for the detected above-threshold contiguous pixels; only clusters containing more than 14 pixels (equivalent to 22.6 μm) were considered as neurons. In a later step, the identified ROIs were masked with the binary mask of all cells to limit misidentification of background elements as neurons. The temporal evolution (time-course) of each segmented ROI was then determined by averaging the Ca^{2+} signal across all corresponding pixels within that ROI (**Figure 8A**). Validation of the segmented neurons was performed through manual inspection, involving a visual assessment of their temporal profile and spatial masks superimposed onto a summary image (e.g., mean image). Neurons exhibiting non-active Ca^{2+} traces were excluded from the analysis. Time-courses from all active cells in each video were saved for subsequent graph analysis.

2.1.7. Graph theory analysis

Graph theory analysis was performed in Python using the NetworkX 2.2 package (Hagberg et al., 2008) (**Figure 8C**). To reduce temporal noise, we first band-pass filtered the extracted time-courses between 0.0001 and 0.07 Hz. The connectivity profile of the neuronal network in each recording was determined by computing pairwise Pearson correlations between the filtered time-courses, yielding one functional connectivity (FC) matrix per video. Subsequently, a threshold was applied to the FC matrices to create binarized adjacency matrices. These resultant adjacency matrices are composed of binary values - ones and zeros - where "one" signifies the presence of a suprathreshold connection (correlation value) between two nodes, and "zero" signifies the absence of such connection. Next, binary undirected graphs were constructed from the resultant adjacency matrices by depicting the neurons in the matrix as nodes, and assigning an edge to every connection that surpassed the threshold. To assess the network's attributes of integration and segregation attributes, we measured the graph measures E_{glob} and C, respectively. Additionally, we computed *average node degree* (*ANDeg*) to estimate the overall number of connections within our graphs (see (Rubinov & Sporns, 2010) for a review on the interpretation of graph metrics).

The number of supra-threshold edges in the constructed graphs, and consequently the resulting graph measure, is significantly influenced by the choice of correlation threshold r_{thresh}.

In order to mitigate potential bias arising from the selection of an arbitrary threshold, we conducted the graph analysis iteratively across a range of r_{thresh} spanning ±0.2-0.8 (in steps of 0.1). There is no evidence available on the range of r_{thresh} suitable for investigating microscale graphs. Nevertheless, previous studies have noted that graphs generated using very low or very high thresholds tend to exhibit attributes that are indistinguishable from those of random or lattice networks (Achard & Bullmore, 2007). Accordingly, we chose a wide range of r_{thresh} (±0.2-0.8) to examine graph attributes excluding only two thresholds: the excessively liberal r_{thresh} ±0.1, which produces spurious correlation/edges, and the extremely strict r_{thresh} ±0.9, typically yielding fragmented or sparsely connected graphs.

One of the challenges we encountered when analyzing the Ca^{2+} imaging data was the varying number of cells in each video. This variance was due to the fact that recordings were collected from different cultures, each with a unique cellular organization. In order to accommodate this variability in cell counts, we computed graph measures for 500 unique randomly sampled sets of cells for set-sizes of 5 to 47 cells. These boundaries were selected such that a) 500 unique combinations were possible and b) data from at least five subjects per group could be included (*refer to Figure A1 in Appendix A*).

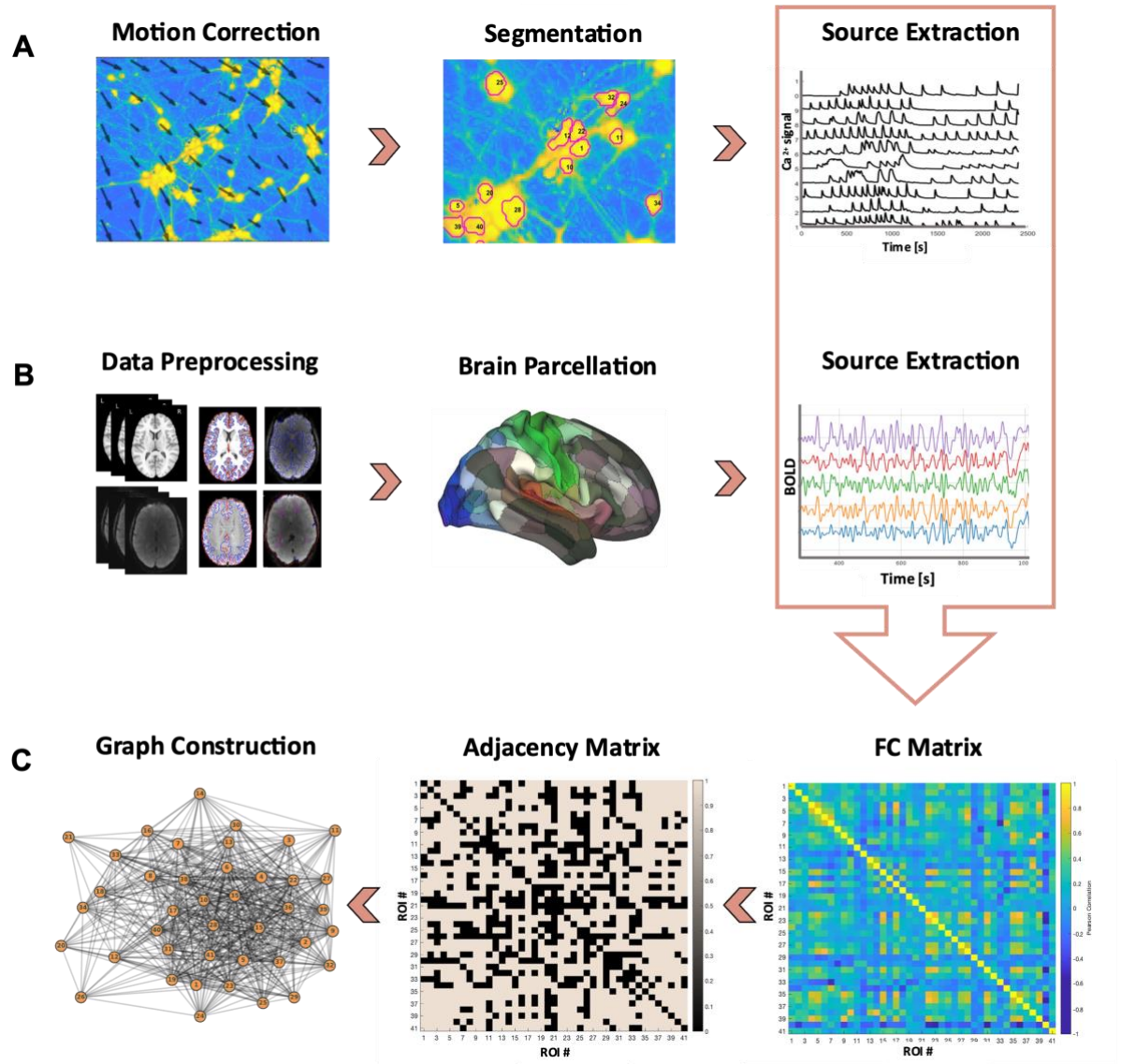

Figure 8. Processing pipeline and graph theoretical analysis of Ca^{2+} imaging recordings and fMRI data. (A) **Motion Correction**: The Ca^{2+} imaging recordings underwent motion correction to account for any motion artifacts. **Segmentation**: Next, active neurons were segmented using a semi-automated pipeline. **Source Extraction**: The time-course of Ca^{2+} signal for each segmented neuron was extracted. (B) **Data Preprocessing**: Structural and functional MRI data were preprocessed using a standardized fMRIPrep pipeline. **Brain Parcellation**: subsequently, brain parcellation was performed, resulting in the division of the brain into 380 distinct regions using the surface-based Glasser atlas. **Source Extraction:** similar to the cellular data, Bold activity averaged across voxels was then extracted from each brain region. (C) Once the time-course of active neurons and brain regions are extracted, the following steps of the graph theoretical analysis were identical for both datasets. **FC Matrix:** functional connectivity (FC) matrices were generated by computing the pair-wise Pearson correlation of all regions of interest (ROIs) in each subject's dataset, whether these ROIs are active neurons in the cellular data, or brain regions in the macroscale data. **Adjacency Matrix:** the FC matrices were then thresholded to create binarized adjacency matrices with values of 0 and 1, where 1 indicates the presence of a suprathreshold connection and 0 indicates the absence of such a connection between a pair of nodes. **Graph Construction:** Binary, undirected graphs were constructed, with nodes representing the ROIs in the adjacency matrix, and edges representing the suprathreshold connections. Graph theory metrics, including measures of network integration (E_{glob}), segregation (C), and *ANDeg*, were computed and compared between experimental groups.

2.1.8. Definition of graph measures

2.1.8.1. Clustering coefficient

The *clustering coefficient C* characterizes the level of segregation in a network by quantifying its tendency to form clusters. On the level of individual nodes, it reflects the proportion of a given node's neighbors that are also neighbors of each other (Watts & Strogatz, 1998). In other words, the *clustering coefficient* c_i is the proportion of closed triangles attached to node *i*, relative to all possible closed triangles between *i*'s neighbors. Nodal *C* can be averaged across all nodes to produce a global description of clustering tendencies of the entire graph. Such network-wide *C* of a graph $G(N, K)$ with *N* nodes and *K* edges is given by the following equation:

$$C = \frac{1}{N}\sum_{i \in N} c_i = \frac{1}{N}\sum_{i \in N} \frac{2t_i}{k_i(k_i - 1)} \qquad \textbf{Equation (1)}$$

where k_i is the number of edges attached to a node *i*, and t_i is the number of closed triangles connected to node *i* (or the number of edges between the direct neighbors of the node *i*). The term $k_i(k_i - 1)/2$ represents all possible connections between the neighbors of the *i*th node in an undirected graph. *C* ranges from zero to one, where *C* = 0 indicates the complete absence of clusters (closed triangles) in the network, while *C* = 1 indicates a fully connected graph.

2.1.8.2. Global efficiency

E_{glob} is defined as the average reciprocal of the shortest path length between any two nodes of the network, with the shortest path being the minimal number of edges passed to get from one node to another (Rubinov & Sporns, 2010; Feldt et al., 2011). Average E_{glob} of a graph with *N* nodes is the mean of E_{glob} of all nodes in the networks and is mathematically defined as follows:

$$E_{glob} = \frac{1}{N}\sum_{i \in N} E_{glob(i)} = \frac{1}{N(N-1)} \sum_{i,j \in N, i \neq j} \frac{1}{l_{ij}} \qquad \textbf{Equation (2)}$$

Here, E_{glob} is the sum of the reciprocal of the shortest path lengths l_{ij} connecting any two nodes *i* and *j* in a graph. This sum is normalized by $N(N-1)$ which is the number of all

possible pairs of nodes in the network excluding self-pairs, i.e., the connection of a node with itself. Thus, $N(N-1)$ represents the off-diagonal elements in the adjacency matrix. The use of the reciprocal of the shortest path length $\frac{1}{l}$, instead of l itself, makes E_{glob} numerically measurable in fragmented graphs in which some nodes are disconnected. In fragmented graphs at least one node i is not connected to the rest of the graph by an edge and $l_{ij} = \infty$.

E_{glob} values range between zero and one where a E_{glob} = 0 indicates the absence of "shortcuts" or long-ranging connections in a network, while a E_{glob} = 1 indicates that all nodes in a network could be reached from any point with few efficient "jumps"/steps.

2.1.8.3. Average node degree

Node *degree* is one of the most fundamental and easy to derive metrics in graph analysis, defined simply as the total number of edges connected to a particular node i (k_i) (Bullmore & Sporns, 2009). *Average node degree* (*ANDeg*) is thus the number of the functional connections found in a graph divided by the number of nodes in that graph:

$$ANDeg = \frac{1}{N}\sum_{i \in N} k_i \qquad \textbf{Equation (3)}$$

2.1.9. Statistical testing

Three-way repeated measures ANOVA (Group x Threshold x Network) was conducted on each of the graph measures computed to assess group differences between MDD patients and healthy controls. We looked for a main effect of Group (controls versus patients) and a possible interaction between the Group factor and other factors (Threshold and Network size). When a group effect or an interaction with the Group factor was detected, we performed post-hoc t-tests of group differences at each network size and each threshold level. This allowed us to determine the specific levels of the factors at which our analysis was more sensitive. To that end, we used Monte Carlo permutation testing by creating a null-distribution of t-values for each measure, shuffling group labels 5000 times, and computing an independent t-test at each level of Threshold and Network size. We used these null distributions to assess the statistical significance of observed t-values in terms of group differences. However, after correcting for multiple comparisons using false discovery rate (FDR) (Benjamini & Hochberg, 1995), the

observed t-values did not show statistically significant differences between groups. Nevertheless, for exploratory purposes, we present the finding at ($p_{\text{uncorrected}} < 0.05$) in the results section.

2.2. On the macroscale

2.2.1. Participants and behavioral assessment

The MRI follow-up study was conducted 4-5 years following the acquisition of the skin biopsies. We contacted former patients and controls from which the skin biopsies were obtained and invited them for a follow-up fMRI scanning session. 15 subjects out of the 18 contacted agreed to participate in the MRI study and were recruited to the Oberpfalz District's Medical Hospital (medbo) in Regensburg. Exclusion criteria included contraindication to MRI scanning (e.g., pacemakers, metal implants, or claustrophobia), pregnancy, and lactation. One patient was wearing hair extensions that was MRI incompatible and was excluded from the study. In total, seven patients and seven controls were included in the study. All enrolled participants provided a written consent in accordance with the ethic commission of the University Hospital of Regensburg (approval number 16-101-0049).

Before the scanning session, subjects completed three questionnaires in German: a demographic questionnaire, the Positive and Negative Affect Schedule (PANAS), and the Beck Depression Inventory (BDI). The PANAS is a 10-item self-report that reliably measures the two primary dimensions of a subject's current mood: positive and negative affect (Krohne et al., 1996; Watson et al., 1988). We used short-term instructions (e.g., "*im Moment*" meaning *right now*) to assess the subject's state of mood at the time of scanning as the mood state can affect functional brain connectivity (Brady et al., 2017; Price et al., 2017). On the other hand, the BDI is a self-report questionnaire to quantitively the behavioral manifestations of depression (intensity) (Beck, 1961). It comprises 21 clinically derived items or depressive symptom category, each with a list of 4-5 self-evaluative statements from which the participants select the statement that best describe their symptom. The statements are ranked in a way that indicates the severity of a given symptom from neutral to maximum severity. The depression score is calculated by summing the ranks of the chosen statements. The resulting score signifies the presence and severity of the depressive disorder, as delineated in **Table 2**.

BDI Total Score	Depression Level
0-10	Non to minimal range of depression
11-18	Mild depression
19-29	Moderate depression
30-63	Severe depression

Table 2. BDI scale cut-off points. BDI: The Beck Depression Inventory.

2.2.2. MRI acquisition

Functional, field map, and structural MRI data were collected using a Siemens Magnetom Prisma 3T Scanner with a 64-channel head-coil at the Brain Imaging Center of the university of Regensburg. During the resting-state fMRI (rs-fMRI) scan, participants were instructed to lie still in the scanner with their eyes closed while staying awake. We used a multiband echo-planar imaging (EPI) sequence with a multiband factor of 4 in a descending order for acquiring functional images with the following acquisition parameters: repetition time (TR) of 1000 ms, echo time (TE) of 30 ms, flip angle (FA) of 60°, and slice thickness of 3 mm. A total of 1320 volumes were collected during a 22-min scan with a field of view (FoV) of 192 mm x 192 mm, an acquisition matrix (AM) of 64 x 64, and an isotopic voxel size of 3 mm.

We acquired field map images after each functional scan to correct for any inhomogeneity in the magnetic field that may have arisen during the scan and caused distortions in the EPI images. Field mapping was carried out using double-echo spoiled gradient echo sequence with TR=715 ms, TE=5.81/8.27 ms, FA=40°, and an isotopic voxel size of 3 mm. This sequence created two magnitude images (one for each echo time) and one phase difference image (the difference between 2 phase images at each echo time). The phase-difference map was then used to estimate the static magnetic field B0-nonuniformity map (also known as field map).

Lastly, we acquired high resolution T1-weighted images using a Magnetization Prepared Rapid Gradient Echo (MP_RAGE). Acquisition parameters included: TR=1910 ms, TE= 3.67 ms, FA=9°, slice thickness = 1 mm, AM= 256 x 256, and FoV= 250mm X 250 mm.

2.2.3. MRI preprocessing

Functional and structural data were preprocessed using a standardized pipeline (fMRIPrep version 20.2.1) (Esteban et al., 2019). The preprocessing steps for structural images comprised segmenting brain tissue and reconstructing the brain surface with FreeSurfer software package (version 6.0.1) (Fischl, 2012) and a spatial normalization of the brain-extracted T1-weighted images to a standard space with nonlinear registration. Resting-state functional images underwent several preprocessing steps. We performed bias field correction performed using estimated field maps that were aligned to the corresponding EPI reference image, followed by susceptibility distortion correction, motion correction, and slice-timing correction. In a last step, the preprocessed functional time-courses were resampled onto the subject-specific cortical surface, resulting in high resolution grayordinate time-courses (**Figure 8B**) *(an automatically-generated summary of fMRIPrep preprocessing steps is provided in Appendix A).*

2.2.4. Graph theory analysis

2.2.4.1. Global level

To parcellate the brain into distinct regions, the surface-based Glasser atlas was employed (Glasser et al., 2016), which subdivides each hemisphere into 180 distinct brain regions or region of interests (RIOs) (**Figure 8B**). In a process analogous to time-course extraction in the cellular data, we computed the mean activity time-course within each region by averaging the activity time-series of all voxels within that region (**Figure 8B**). Band-pass filtering was then performed on the resulting region-specific signal retaining the characteristic low frequency range of the BOLD signal between 0.01 and 0.1 Hz. This frequency range mitigates the impact of low-frequency drift and high frequency physiological noise, including respiration and cardiac pulse. Next, an FC matrix of the 360-ROI network was created for each subject. Similar to the cellular data, we constructed the 360 x 360 FC matrices by computing the pair-wise Pearson correlation coefficient between the BOLD time-courses of all ROIs (**Figure 8C**).

We then binarized the FC matrices using three r_{thresh} (±0.5, ±0.6, ±0.7). The choice of these thresholds was based on the connection density of the graph that they generate. Connection density quantifies the number of existing edges in a graph relative to the maximum possible number of edges. This metric reflects connection costs, where increased connection density

signifies a greater number of edges, leading to higher wiring costs. In contrast to *in vitro* microscale neuronal networks, prior research at the macroscale has provided evidence that human brain networks typically exhibit a connection density range of 5-50%, emphasizing a tendency towards sparse network connectivity in the brain (Humphries et al., 2005; Lynall et al., 2010; Meng et al., 2014; Vértes et al., 2012). In our data, this range of connection densities was attained through the three r_{thresh} (0.5, 0.6, 0.7) (**Figure 9**). Accordingly, these r_{thresh} were used to binarize the connectivity matrices, resulting in adjacency matrices. In an adjacency matrix, a value of 1 reflects the presence of a suprathreshold connection/correlation between a pair of ROIs, and a value of 0 represents the absence of such connection/correlation. Finally, we constructed a binary, undirected graph from each subject's adjacency matrix in which nodes represented different brain regions, and edges represented the suprathreshold functional connections between these regions (**Figure 8C**).

To investigate differential functional network topology in depression on a whole-brain, systems level, we computed and compared the same graph metrics that we estimated for the cellular data. These include E_{glob} and C for assessing integration and segregation properties, respectively. *ANDeg* was also computed to determine and compare the overall number of edges in the patients and controls graphs (see section 2.1.8 for mathematical definitions).

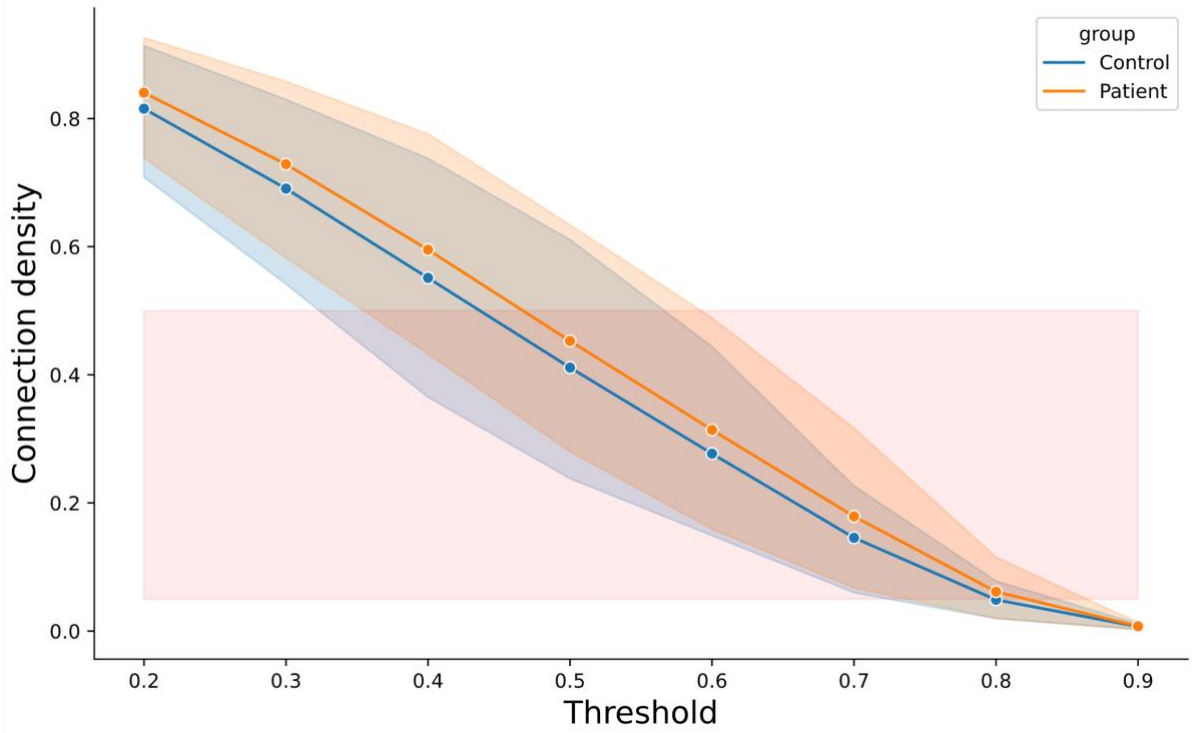

Figure 9. Connection density of whole-brain networks across groups as a function of correlation threshold. The thresholds (±0.5, ±0.6, ±0.7) correspond to the connection density range of 0.05-0.5 (the filled red area) which is typically reported in macroscale human brain networks. The shaded area represents the 95% confidence interval.

2.2.4.2. Nodal level

In contrast to single neurons within *in vitro* cultures, developed brain regions at the whole-brain level exhibit specialized functionality resulting in region-specific, unique and meaningful topological profile that is worth investigating. To that end, we computed graph theory metrics to describe the functional topological characteristics of the individual 360 parcellated ROIs of the Glasser atlas. We investigated nodal efficiency and centrality depicted by the two graph metrics of betweenness centrality and node degree.

2.2.4.2.1. Betweenness centrality

BC counts the proportion of shortest paths that crosses a given node, thus, reflecting how "central" that node is in a network. The highest *BC* is for one node, the more influential that node is by mediating a high proportion of information traffic (Fornito et al., 2016). *BC* is for a given node *i* is computed as follows:

$$BC(i) = \frac{1}{(N-1)(N-2)} \sum_{h \neq i, h \neq j, j \neq i} \frac{\rho_{hj}(i)}{\rho_{hj}} \qquad \textbf{Equation (4)}$$

Where $\rho_{hj}(i)$ is the number of shortest paths between *h* and *j* that passes through *i*. This number is normalized by ρ_{hj}, which is the total number of shortest paths from node *h* to node *j*, including the ones that do not go through node *i*. $(N-1)(N-2)$ is the number of node pairs that does not include node *i* and is used to normalize betweenness centrality between 1 and 0. A value of 1 means that a node lies on every single shortest path in the network, and a value of 0 indicates that the node is not crossed by any shortest path.

2.2.5. Statistical analysis:

On the global level, similar to the analysis on the microscale, we conducted a Two-way repeated measures ANOVA (Group x Threshold) to examine potential group differences in E_{glob}, *C*, and *ANDeg*. In this analysis, the fact "Network size" was omitted given the uniformity of the whole-brain data in terms of the number of parcellated ROIs. This uniformity is a result of employing the same atlas in the parcellation step. On the nodal level, we assessed group differences in each of the computed graph measures by employing permutation test (5000 iterations; $p < 0.05$) at each ROI/node and at each r_{thresh}. The results did not survive the FDR correction for multiple comparisons (360 comparisons/nodes) ($p_{\text{corrected}} < 0.05$). Therefore, only the uncorrected results at $p_{\text{uncorrected}} < 0.01$ will be reported in the following results section.

Chapter 3. Results

This chapter presents the findings of this multiscale study of functional network topology in MDD. It begins by reporting topological findings on the microscale level followed by reviewing the global and nodal topological results at the macroscale.

3.1. On the microscale

The first part of this work involved examined differential functional network topology in *in vitro* cultures of reprogrammed neurons derived from 9 MDD patients and matched healthy controls. These cellular networks were captured by means of Ca^{2+} imaging and probed for their functional architecture using graph theory analysis focusing on the most fundamental functional principles: integration and segregation. Considering that single neurons in *in vitro* cultures are unlikely to exhibit specialized functions, particularly in the absence of stimuli, our microscale analysis primarily focused on averaged graph metrics that describe network organization at a global level rather than on an individual node level. Furthermore, since binarized adjacency matrices change substantially with r_{thresh}, we computed graph measures for a range of such thresholds (r_{thresh} = ±0.2-0.8). These global metrics were E_{glob} (integration), C (segregation), and *ANDeg*.

3.1.1. Demographic details and sample characteristics

We investigated group differences in age, gender, body mass index (BMI), and $HAMD_{21}$ scores (**Table 3**). Since the control group was selected to match MDD patients in terms of gender and age, the two groups do not differ in gender (4 males and 5 females) nor in age (age_{MDD}= 32.33, $age_{control}$= 33.22, $t(16)$= 0.19, p= 0.85). Similarly, BMI (BMI_{MDD}=22.67, $BMI_{control}$=24.58) did not differ between the groups ($t(16)$=-1.29 , p=0.22). As expected, $HAMD_{21}$ score differed significantly between patients and controls ($HAMD_{MDD}$=26 (moderate to severe depression), $HAMD_{control}$=0.4 (no depression), $t(16)$=-12.19, p<0.001). Furthermore,

the control subjects did not report any past occurrences of depressive episodes or other psychiatric conditions.

Measure	Healthy controls Mean (±SEM)	MDD patients Mean (±SEM)	t value	p value
N	9	9	-	-
Gender (M/F)	4/5	4/5	-	-
Age	33.22 (±3.44)	32.33 (±3.82)	0.195	0.85
BMI	22.67 (±0.72)	24.58 (±1.29)	-1.29	0.22
HAMD	0.4 (±0.25)	26 (±1.63)	-12.19	< 0.001

Table 3. Demographic and clinical characteristics of microscale study's cohorts. SEM: Standard error of the mean, BMI:Body mass index; HAMD: Hamilton Rating Scale for Depression.

3.1.2. Segregation properties

Segregation attributes of cultured neuronal networks were assessed by computing *C*. *C* gives an estimation about the neighbors of one node being also neighbors of each other, indicating the capacity of the network to form clusters that could engage in specialized functions. We detected a reduction in the *C* in patient-derived neuronal cultures compared to controls (main effect of group, $F(1,8)= 5.97$, $p= 0.04$, Figure 10). This decrease indicated a diminished segregation capacity in cultured neural networks of the patient group compared to their matched healthy controls. The *C* varied significantly with network size (main effect of network size, $F(37, 296)= 73.59$, $p< 0.001$) and threshold (main effect of threshold, $F(6, 48)= 1003.25$, $p< 0.001$).

Post-hoc t-tests were performed to assess the specific network sizes and thresholds at which a significant decrease in *C* occurred (**Figure 10**). These tests showed that group differences were primarily noticeable in larger network sizes *(refer to Table B1 in Appendix B for post-hoc statistics)*.

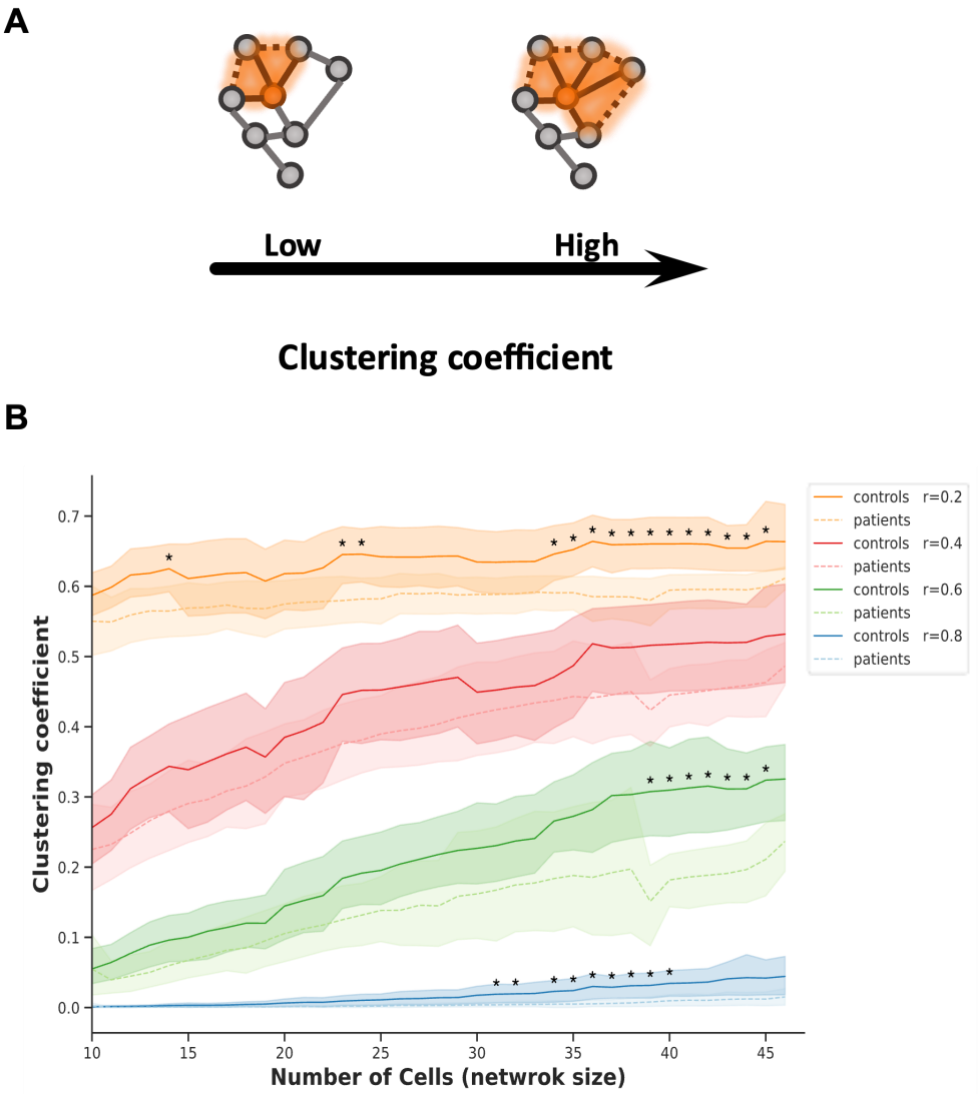

Figure 10. Decreased *clustering coefficient* in patient-derived neurons compared to controls across varying network thresholds and sizes. (A) Schematic illustration of two networks with high and low *C*, a segregation measure. *C* of a given node *i* (the orange node) represents the proportion of closed triangles attached to node *i* relative to all possible closed triangles between *i*'s neighbors. In the left network, the orange node has a low *C* as its direct neighbors are sparsely connected, resulting in only 2 closed triangles (out of 6 possible ones). In contrast, the right network shows a higher *C* since the number of closed triangles between the orange node and its neighbors is higher (4 in this case). **(B)** *C* showed a significant overall reduction (p=0.04) in neuronal cultures of MDD patients (dashed lines) compared to controls (solid lines) across network sizes and all correlation thresholds r_{thresh} (depicted in different colors). *C* was significantly higher when lower r_{thresh} was applied (p< 0.001) and for larger network sizes (p< 0.001). We explored the levels of network sizes and r_{thresh} at which group differences in *C* occurred. Asterisks (*) indicate the presence of statistically significant difference (p<0.05, uncorrected). *C* was computed for all r_{thresh} ranging from ± 0.2 – 0.8 *(see Figure B1 in Appendix B)*; for clarity, results of only four thresholds are shown. The shaded area represents the 95% confidence intervals.

3.1.3. Integration properties

We estimated E_{glob} as a measure of the network capacity for parallel information routing and integration across its distributed units. Although our data revealed a general trend of reduced E_{glob} in neuronal networks derived from patients compared to controls, group difference did not reach statistical significance (no main effect of group, $F(222,1776)=1.63$, $p=0.194$, **Figure 11**). Additionally, no significant influence of different network sizes or thresholds was detected on group differences in E_{glob} (no three-way interaction effect Group x Network size x Threshold, $F(222,1776)= 1.86$, $p=0.152$).

However, the data demonstrates a significant increase in E_{glob} as a function of network size (main effect of network size, $F(37, 296)= 23.56$, $p< 0.001$). Furthermore, there was a significant reduction in E_{glob} as the r_{thresh} used for constructing binarized graph increased (main effect of threshold, $F(6, 48)=1157.36$, $p< 0.001$).

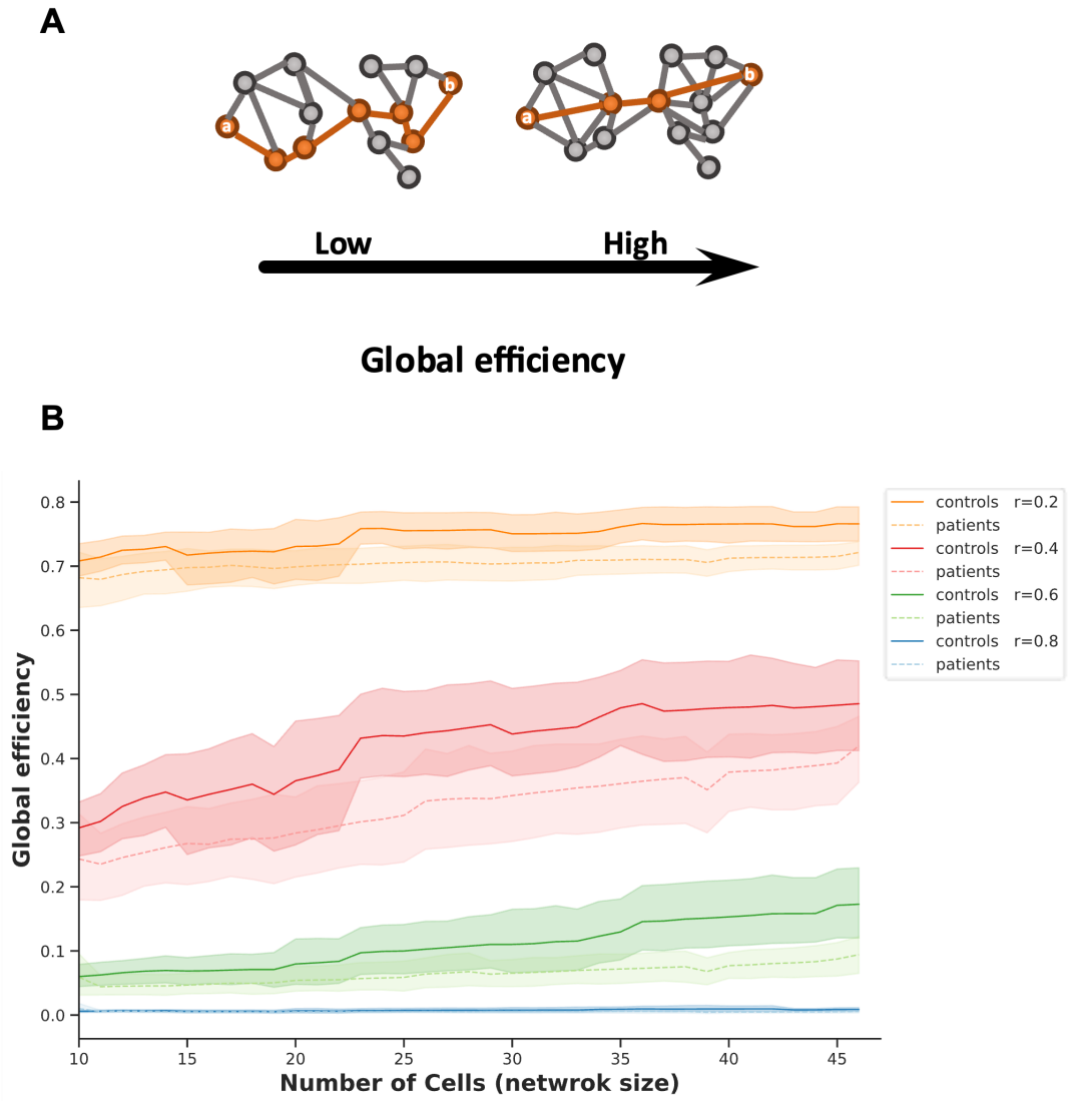

Figure 11. Alterations in *global efficiency* across experimental groups, thresholds, and network sizes. (A) Schematic illustration of two graphs with high and low E_{glob}. E_{glob} is a measure of network integration determined by averaging the reciprocal of the *shortest path length* between all pair of nodes in a network. *Shortest path length*, in turn, is defined as the minimum number of edges that must be traversed to get from one node to another. The network on the left depicts a graph with low E_{glob} evident by the large number of steps (6) required to reach node B from node A, while the network on the right shows high E_{glob} as only 3 steps are required. (B) Changes in mean E_{glob} in graphs of depressed patients (dashed lines) compared to controls (solid lines) across different network sizes and r_{thresh} (depicted by difference colors). Although an overall trend of lower E_{glob} in MDD neuronal cultures is present, no statistically significant group differences in network integration capacity could be detected (p=0.194). E_{glob} significantly increased as the networks grew larger ($p< 0.001$) and as r_{thresh} became more liberal ($p< 0.001$). E_{glob} was computed for all r_{thresh} ranging from ± 0.2 – 0.8 *(see Figure B2 in Appendix B)*; for clarity, results of only four thresholds are shown. The shaded area represents the 95% confidence interval.

3.1.4. Average node degree

ANDeg is one of the most fundamental graph metrics. It describes the number of functional connections that nodes in a network have on average. *ANDeg* in our patient-derived neuronal microscale networks showed a significant decrease compared to networks of healthy controls (main effect of group; $F(1,8)=5.44$, $p=0.048$, **Figure 12**). Besides, *ANDeg* showed an overall significant increase as the network grew larger (main effect of network size, $F(37, 296)=167.82$, $p< 0.001$) and at more liberal r_{thresh} (main effect of threshold, $F(6, 48)= 622.24$, $p< 0.001$) as seen with the previously reported graph metrics.

We also performed post-hoc t-tests to identify the specific network sizes and thresholds at which significant group differences in *ANDeg* became evident. As seen in *C*, group differences in *ANDeg* were discernible at larger network sizes (more than 20) *(refer Table B2 in Appendix B for post-hoc statistics).*

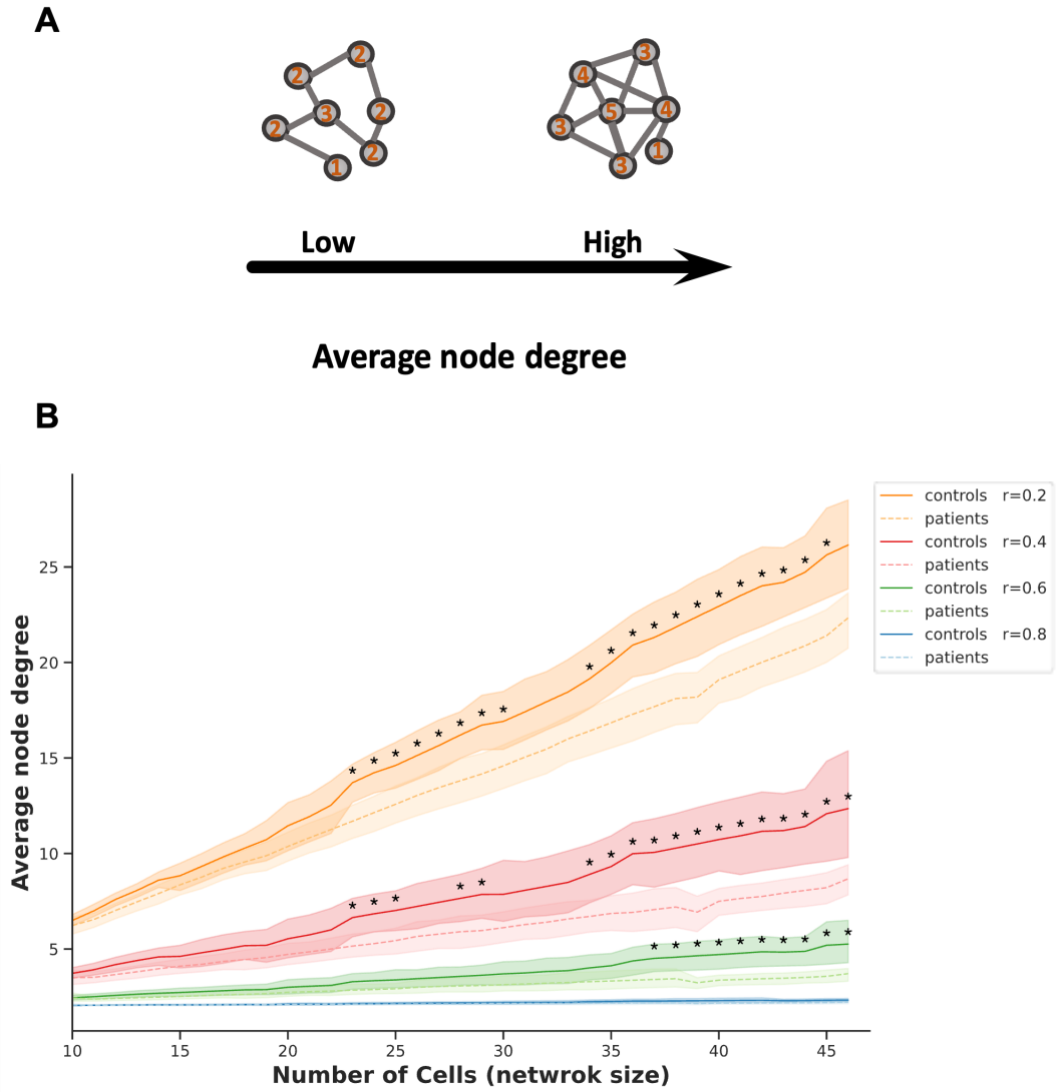

Figure 12. Decreased *average node degree* in patient-derived neurons compared to controls across varying network thresholds and sizes. (A) schematic illustration of two network topologies with contrasting *ANDeg*. *ANDeg* is defined as the mean of the number of functional connections per node in the network (illustrated here by a number inside each node in the graphs). The graph on the left represents a network with low *ANDeg* (equals to 2), while the right graph shows high *ANDeg* (equals to 3.3) as the overall number of connections in the network increases. (B) *ANDeg* showed a significant overall decrease ($p=0.048$) in graphs of depressed patients (dashed lines) compared to controls (solid lines) across varying network sizes and r_{thresh} (depicted in different colors). *ANDeg* significantly increased with larger network sizes ($p<0.001$) and lower r_{thresh} ($p<0.001$). We explored the levels of network sizes and r_{thresh} at which group differences in *ANDeg* occurred. Asterisks (*) indicate the presence of statistically significant difference ($p<0.05$, uncorrected). *ANDeg* was computed for all r_{thresh} ranging from ± 0.2 – 0.8 *(see Figure B3 in Appendix B)*; for clarity, results of only four thresholds are shown here. The shaded area represents the 95% confidence intervals.

3.2. On the macroscale

3.2.1. Demographic details and sample characteristics

Table 4 demonstrates BMI values and behavioral scores and their differences between the patient group and their age- and gender-matched healthy controls who were recruited for the MRI study. BMI differed significantly between groups showing higher values in MDD group (BMI_{MDD}=28.83, $BMI_{control}$=23.29, $t(12)$=-2.827, p=0.015). There were no differences between the groups in terms of positive and negative affect measured prior to the fMRI, as statistically tested by an independent t-test ($p < 0.05$). Interestingly, BDI scores did not differ between groups (**Table 4**). It is also worth noting that there was high variability in BDI within the patient group, with BDI scores ranging from 0 to 23. Among the seven patients, three were receiving antidepressant treatment at the time of scanning, with only two of those reporting BDI scores indicative of moderate depression. The remainder of the patient cohort demonstrated BDI scores typical for normal mood.

	Healthy controls Mean (±SEM)	MDD patients Mean (±SEM)	t value	df	p value
N	7	7	-	-	-
Gender (M/F)	3/4	3/4	-	-	-
Age	37.71 (±4.76)	37.86 (±5.04)	-0.02	12	0.984
BMI	23.29 (±1.09)	28.83 (±1.63)	-2.827	12	0.015
BDI	3.86 (±2.24)	9.57 (±3.37)	-1.413	12	0.183
PANAS pos.	35.71 (±2.93)	34.29 (±2.45)	0.375	12	0.715
PANAS neg.	11.43 (±0.81)	13.71 (±1.38)	-1.431	12	0.178

Table 4. Demographic profile and mood rating of macroscale study's cohorts.
SEM: Standard error of the mean; BMI: Body mass index; BDI: Beck Depression Inventory; PANAS: Positive and Negative Affect Schedule.

3.2.2. Global graph theoretical analysis

In this analysis, we investigated differences in macroscale functional network topology between the experimental groups at a global level. Figure 13 illustrates the computed metrics of integration (E_{glob}) and segregation (C), together with *ANDeg* at the three r_{thresh} corresponding to connection densities range between 5-50%. The mixed ANOVA (Group x Threshold)

showed no significant group effects observed neither in *C* (no main effect of group; $F(1,12)=0.002$, $p=0.965$) nor in E_{glob} (no main effect of group; $F(1,12)=0.141$, $p=0.714$) (**Figure 13**). Similarly, *ANDeg* did not differ significantly between the experimental groups (no main effect of group; $F(1,12)=0.102$, $p=0.755$) (**Figure 13**). However, the fMRI data showed a trend of increased *C* and *ANDeg* in large-scale networks of depressed patients.

Graph metrics at the macroscale decreased significantly as the r_{thresh} applied increased (**Figure 13**). This effect of threshold on graph measures was observed for all computed graph metrics: *C* (main effect of threshold; $F(1.3,16)=321.264$, $p<0.001$), E_{glob} (main effect of threshold; $F(1,13.1)=617.485$, $p<0.001$), and *ANDeg* (main effect of threshold; $F(1,13.1)=63.237$, $p<0.001$). However, graph metrics did not differ between groups as r_{thresh} varied: *C* (no Group x Threshold interaction; $F(1.3,16)=0.47$, $p=0.558$), E_{glob} (no Group x Threshold interaction; $F(1,13.1)=0.193$, $p=0.69$), and *ANDeg* (no Group x Threshold interaction; $F(1,13.1)=0.015$, $p=0.921$).

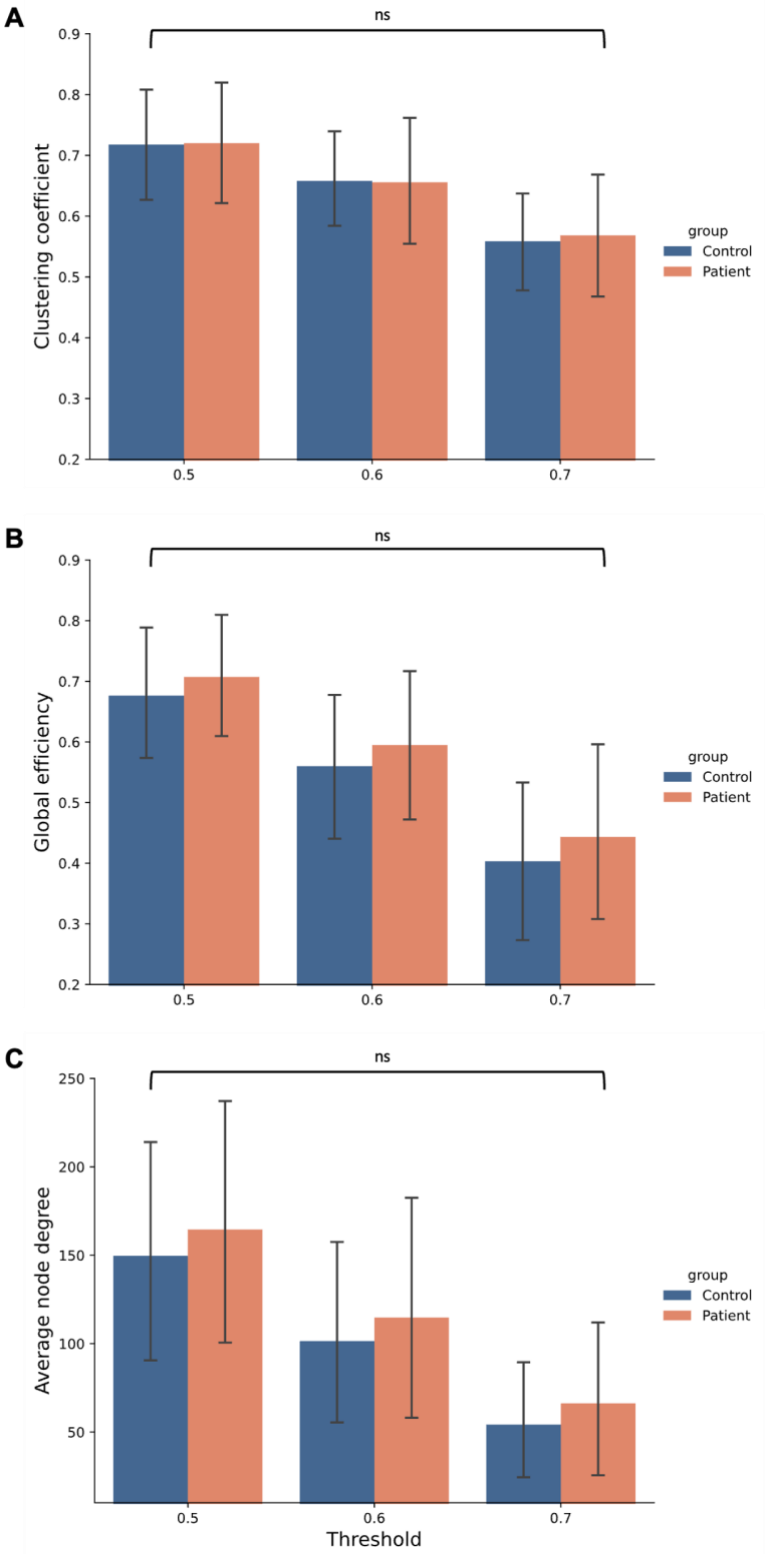

Figure 13. Differences in functional network organization between groups on the macroscale. At each of r_{thresh} tested, no significant differences between former depressed patients and their healthy controls in terms of their segregation capacity as measured by *C* (A), integration capacity as measured by E_{glob} (B), or in the overall number of connections per node as measured by *ANDeg* (C). Error bars represent the 95% confidence intervals. ns: not significant (after correcting for false discovery rate).

3.2.3. Nodal graph theoretical analysis

To further localize distinct regional differences in topological properties between groups, we measured nodal graph metrics — *node efficiency*, *node degree*, and *betweenness centrality* — for each of the 360 regions defined by the Glasser atlas. Even at a $p_{uncorrected} < 0.01$, no significant depression-related changes were observed in *nodal efficiency* or *node degree*. However, only *BC* differed between groups at $p_{uncorrected} < 0.01$. *Betweenness centrality* is a measure of hubness. It reflects how central a given region is in a network in terms of integrating information through shortest paths. Two regions in the left hemisphere exhibited differential *BC* in the patient group compared to healthy controls within the investigated threshold range. These regions are an area in the intraparietal sulcus (IPS) and the anterior agranular insula complex (AAIC) (**Figure 14**). While *BC* of left IP decreased in the patient group, left AAIC showed increased centrality in the patient networks compared to those of healthy controls ($p_{\text{uncorrected}} < 0.01$).

Table 5 summarizes the statistics of this analysis.

Node	Side	r_{thresh}	Group	Mean	CI		t value	df	p value
					upper	lower			
Intraparietal (IP0)	L	0.5	Control	0.0022	0.00076	0.00082	3.555	12	0.0029
			patient	0.0006	0.00023	0.00024			
Intraparietal (IP0)	L	0.6	Control	0.004	0.002	0.002	2.893	12	0.0069
			Patient	0.0007	0.00031	0.00027			
anterior agranular insula (AAI)	L	0.7	Control	0.006	0.0037	0.0034	-3.052	12	0.0058
			Patient	0.0023	0.0024	0.0015			

Table 5. descriptive and inferential statistics on nodal *betweenness centrality* in large-scale networks. r_{thresh}: correlation threshold; CI: confidence interval; df: degrees of freedom.

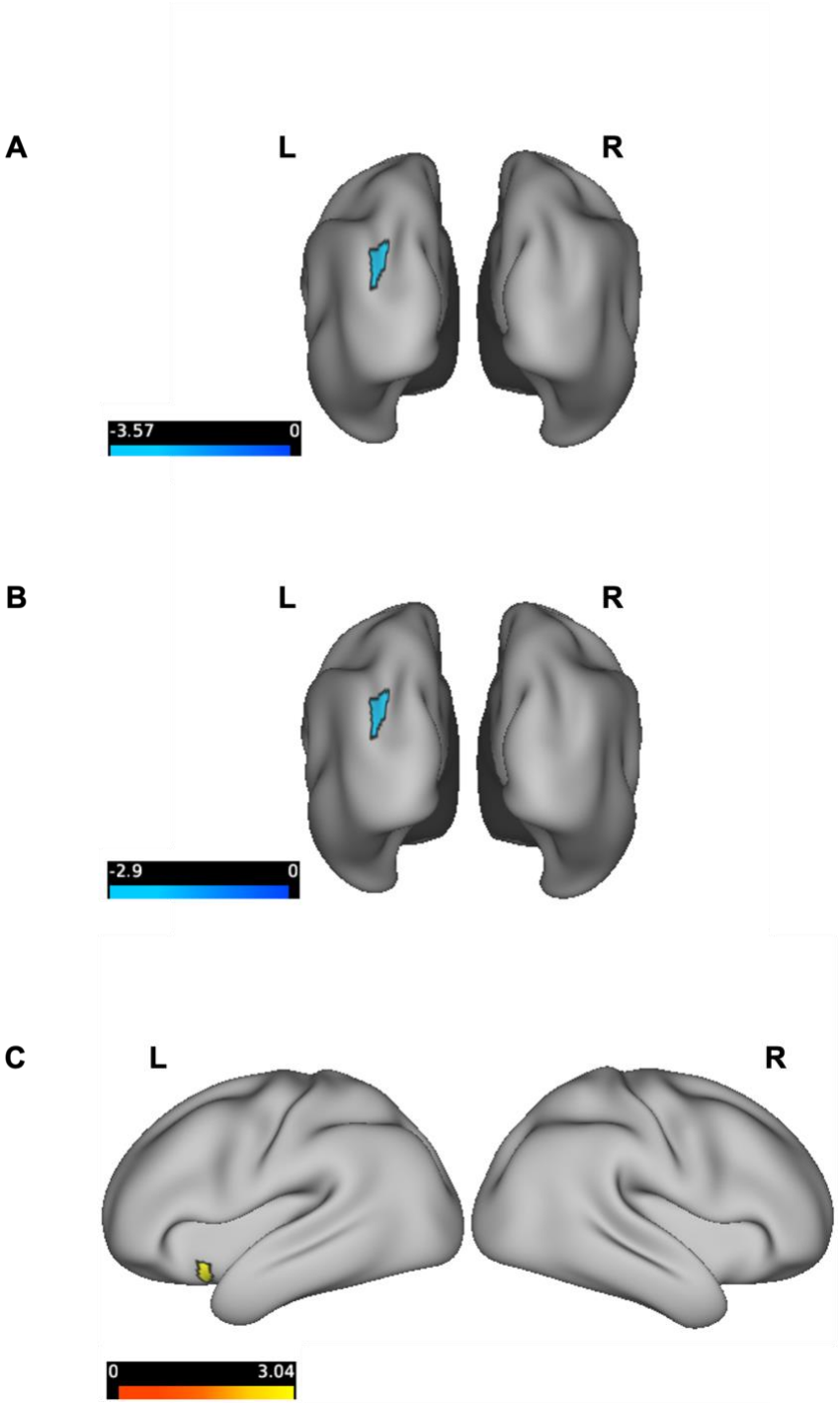

Figure 14. Changes in nodal *betweenness centrality* in the brain of depressed patients in comparison to healthy controls at different correlation thresholds. (A) BC of the left intraparietal region was reduced in depressed patients at r=0.5 and (B) at r=0.6 compared to controls. (C) At r=0.7, increased BC of the anterior agranular insula complex was observed in depressed patients in comparison to healthy controls.

Chapter 4. Discussion

This chapter delves into the findings of this research and discusses their interpretations, as they aim to explore the differential functional organization of neuronal network in MDD. These MDD-related topological changes were probed across two scales of spatial granularity within the same groups of subjects: the cellular and the systems levels. We set out to examine potential differences in graph theoretical measures of integration and segregation between MDD patients and controls and to assess the consistency of these results between micro and macro levels. Network architecture was captured at the cellular level by means of calcium imaging and fluorescent microscopy, while fMRI was utilized to investigate whole-brain, macroscale networks. Graph theory was employed to characterize global and nodal functional network topology on the two scales. The main focus was on graph metrics that reflected features of segregation (*C*), integration (E_{glob}), and the overall number of nodal connections (*ANDeg*). Additionally, nodal graph metrics identifying nodes of influence in the large-scale brain networks were also examined (*degree*, *efficiency*, and *BC*).

The investigation of multiscale network topology in psychiatry, and particularly in the context of MDD, remains a relatively unexplored area. To date, there is a notable lack of research against which we can compare our multiscale findings. In this chapter, we will examine and discuss our findings at each scale individually, facilitating a comparative discussion with the existing body of research specific to each respective scale. The discussion is commenced by presenting the microscale findings, followed by a discussion of the results on the macroscale level. Subsequently, an integrated view will be developed that aims to elucidate the relation between the findings observed at both scales.

4.1. Findings on the microscale

The microscale findings involved decreased segregation capacity coupled with a reduction in overall node degree in iPSC-derived neuronal networks of depressed patients compared to their healthy controls. Although integration properties, as measured by E_{glob}, also exhibited a clear reduction trend in patient-derived networks, this reduction did not show statistical significance.

4.1.1. Reduced segregation capacity and overall node degree in patient-derived cellular networks

Small-world, efficient networks typically support a level of segregation that can be measured by the graph metric *C*. These segregation abilities are typically facilitated by a network topology that allows for dense connections between adjacent and functionally related neurons, forming functionally specialized clusters or "communities". The significant reduction in *C* we found in iPSC-derived neuronal cultures of depressed patients indicates altered local organization and diminished functional specialization and segregation capacity at the cellular level in depression. The influence of clustered topology on neural function (Bisio et al., 2014; Shein-Idelson et al., 2011) and network dynamics (Yamamoto et al., 2018; Wang, 2011; Litwin-Kumar & Doiron, 2012) suggests that the breakdown of such clustered topology is likely to have implications for the network's dynamic repertoire, impacting neural activity and potentially contributing to the restricted dynamics repertoire previously reported in MDD at the macroscale (Holtzheimer & Mayberg, 2011; Kaiser et al., 2015; Tognoli & Kelso, 2014). However, further multiscale investigations examining the relationship between microscale topological alterations and disease manifestation on the macroscale are warranted to establish a causal link between these phenomena. Additionally, the positive effect of segregated topology on the network's robustness and resilience to insult (Teller et al., 2014; Yamamoto et al., 2018) suggests that a network lacking strong local interconnectivity can no longer confine and impede the propagation of pathological processes within the system. Consequently, this diminishes the network's ability to withstand damage, rendering it more vulnerable to the spread of psychopathologies across its parts (Fornito et al., 2015). Therefore, the reduced segregation capacity seen in our patient-derived cellular networks highlights their increased vulnerability to the pathological processes of depression and the subsequent propagation of these processes throughout the network.

In our patient data, *ANDeg* showed a significant decrease in patient-derived neuronal networks compared to those of controls. This finding aligns with previous postmortem studies that have indicated a link between depression symptoms and reduced synaptic density in prefrontal cortex and hippocampus (for reviews see Kang et al., 2012; Duman & Aghajanian, 2012). The aforementioned link was further substantiated in iPSCs of patients with a commonly found mutation in major psychiatric disorders that is involved in synaptic regulations (Wen et al., 2014). While we did not directly assess synaptic density and dendritic complexity in our neuronal cultures, we postulate that the reduced overall node degree in our patients' data could be a result of such synaptic loss, hindering the formation of healthy connections between neurons. This assumption is in line with previous *in vitro* and *in vivo* investigations reporting an impact of synaptic loss on network connectivity and dynamics in depression. An *in vitro* study linked reduced dendritic complexity and synaptic density to alterations in network dynamics observed in iPSC-derived neurons of patients with mitochondrial pathology accompanied with depressive mood manifestations to (Gunnewiek et al., 2020). On the other hand, Holmes et al. (2019) observed alterations in network connectivity in relation to diminished synaptic density in depressed patient *in vivo*. This established effect of molecular alteration on functional network organization might suggest that the reduced *ANDeg* we observe here in patient-derived networks could be a consequence of genetically determined variations in synaptic formation affecting microscale network communication and architecture.

4.1.2. Changes in integration capacity of patient-derived cellular networks

Network segregation must be balanced with robust integration features that is vital to efficiently integrate and combine information across network parts and communities, ensuring dynamic flexibility. In this work, we observed no significant differences in integration properties measured by E_{glob} between the experimental groups. Nevertheless, our data demonstrates a consistence tendency towards reduced E_{glob}, suggesting a potential significance that could be unraveled with a larger sample size. Typically, an effective integration of information is facilitated by few efficient, yet energy-expensive, long-distance connections linking remote parts of the network, so called "shortcuts". Accordingly, the reduction trend we report in E_{glob} in microscale networks of depressed patients might be a consequence of inadequate energy metabolism that would hinder first and foremost the formation of those costly shortcuts required for optimal integration function. Interestingly, our group previously

reported bioenergetic imbalance and mitochondrial dysfunction in both fibroblasts and NPCs of depressed patients, with a significant overlap between the subjects in that study and our sample (Kuffner et al., 2020; Triebelhorn et al., 2022). The findings of these reports, along with evidence from large-scale studies, support the hypothesis that relates MDD etiology to mitochondrial dysfunction (Tobe, 2013; Rezin et al., 2008). However, further investigations are warranted to establish a direct link between dysfunctional bioenergetic status and network functional topology in depression.

4.1.3. Remarks on methodology and analysis

Microscale graph topology was significantly influenced by both the network size and the threshold applied to binarize FC matrices. These two factors dictate the number of nodes and edges that will be included in the graph. Larger network sizes (more nodes) and lower thresholds (more edges) broaden the range of connectivity patterns available to the network. This diversity in FC configurations increases the likelihood for an enhanced functional topology, and explains the observed increase in graph metrics as the network size increases and the correlation threshold becomes more liberal.

While the conducted post-hoc analysis of *C* and *ANDeg* did not survive multiple correction comparisons, the omnibus test of ANOVA showed significant findings. This highlights that the group differences observed in these two measures are nonrandom and strong, with the potential of becoming more statistically pronounced with a larger sample size.

Even though our skin biopsies were obtained at the end of the patients' hospital stay after receiving different antidepressants, the confounding variations between patients in terms of medication use is expected to be eliminated after several cell divisions of the fibroblasts and upon reprogramming (Garbett et al., 2015; Soliman et al., 2017). Thus, the aberration in functional topology we detected in neural cultures of depressive patients suggests a genetic predisposition for neural networks to functionally organize differently in depression, even at a cellular resolution. Since the genetic influence undoubtedly plays a role in shaping and controlling network organization and connectivity (van den Heuvel et al., 2013; Fornito et al., 2011; Smit et al., 2010), iPSC technology is thus an invaluable tool to identify measures of microcircuit topology as endophenotypes of neuropsychiatric disorders. It is important to point

out, however, that iPS cells could still retain residual epigenetic memory from its parent somatic cells, due, for example, to incomplete programming (Kim et al., 2010; Ohi et al., 2011). Therefore, further research is needed before making strong claims about the pure genetic or epigenetic origin of the microscale topological dysfunction we found in microscale neuronal networks of depressed patients.

A valid alternative to investigating and modeling environmental effects on network topology in psychiatric diseases like MDD is to utilize a sister technology that generates what is referred to as induced neurons (iNs) (Vierbuchen et al., 2010; Yang et al., 2011). Unlike iPSC technology, the somatic cells are directly induced into neurons with this technique, skipping the reprogramming step and thus preserving the entire epigenetic landscape of the donor cells. This is assuming that the epigenetic modifications in skin cells are relevant for psychiatric disorders such as MDD (Soliman et al., 2017). Such technique can be used in exploring the functional features of microscale neuronal circuits in MDD, offering valuable insights into the underlying biological mechanisms of the disorder and its potential connection to epigenetic regulation.

The iPSC-derived NPCs and neurons were further examined and characterized in a previous study of our group which involved half of the cell lines that were included in the current work (Triebelhorn et al., 2022). Not only did patient-derived NPCs show altered mitochondrial function as previously mentioned, but they also showed lower cytosolic Ca^{2+} levels and smaller soma sizes. Additionally, iPSC-derived neurons showed a clear bipolar or multipolar morphology and expressed neural markers indicative of both glutamatergic and GABAergic signalling. The electrophysiology of iPSC-derived neurons of MDD patients was also examined, revealing lower membrane capacitance, lower resting membrane potential, increased Na^{+} current density, and increased spontaneous activity compared to neurons of controls. The observed decrease in membrane capacitance, which is indicative of smaller cell size (Kim & von Gersdorff, 2010; Lindau & Neher, 1988), aligns with the diminished cell size reported in the NPCs from which these neurons were generated (Triebelhorn et al., 2022). Moreover, the decreased membrane potential and cell size were reportedly linked to bioenergetic dysfunction or delayed neural development (Triebelhorn et al., 2022; Vaarmann et al., 2016). In any case, it is unclear how these MDD-related differences in biophysics and spontaneous activity relate to the alterations in microscale network topology we report in this

work. While the current study did not specifically aim to explore this association, investigating such a connection presents an intriguing direction for future research.

4.2. Findings on the macroscale

At the systems level, we did not discern any statistically significance distinctions between brain networks of MDD patients and those of the control group. Nevertheless, an intriguing inverse pattern emerges; E_{glob} and *ANDeg* seemed to increase in MDD patients compared to the control group. Given that nodes in large-scale networks represent brain regions with known function, we conducted a deeper examination of whole-brain networks and explored nodal graph characteristics of these various brain regions. While the nodal graph theoretical analysis did not yield any group differences that survived correction for multiple testing, it is worth emphasizing and discussing the trends in nodal topological differences observed in the data (at $p_{uncorrected} < 0.01$). These trends involved two prominent regions within the left hemisphere that exhibited a noticeable shift in influence as measured by *BC*. These regions are IP region, exhibiting a reduction in *BC*, and AAIC, exhibiting an increase in *BC* within large-scale networks of MDD patients compared to healthy controls.

4.2.1. Alterations in global network organization of whole-brain networks of MDD patients

The absence of statistically significant differences in global network topology between the groups could be attributed to the limited statistical power of the analysis due to the relatively small sample size, with only 7 subjects in each group. However, there was a notable increasing trend in both E_{glob} and *ANDeg* in whole-brain networks of MDD patients, indicating a tendency towards increased integration and overall node connections in large-scale networks in depression.

The existing body of literature on changes in network topology associated with MDD at the macroscale presents inconclusive findings (Gong & He, 2015). While some reports suggest a shift towards randomness and enhanced E_{glob} and integration in individuals with depression (Wu et al., 2020; Zhang et al., 2011), contrasting observations underscore an opposing pattern marked by decreased integration (Meng et al., 2014). In select instances, this diminished integration was accompanied by reduced network segregation, as noted by Li et al. (2015).

Notably, some studies have reported the absence of discernible differences in network topology between brain networks of individuals with depression and those of healthy controls (Bohr et al., 2013; Lord et al., 2012). This inconsistency in the results is likely attributed to the considerable heterogeneity within the patient sample across these studies as they included patients with varying age, clinical characteristics, number of depressive episodes, and/or treatment status. Other factors contributing to the disparities of the results include: variations in motion artifacts, in data preprocessing approaches (Liang et al., 2012), and in node definitions and brain parcellation methods which profoundly influence graph structure and, therefore, graph metrics (Wang et al., 2009; Zalesky et al., 2010).

Another important highlight in the fMRI data is the high variability of global graph metrics within both experimental groups (indicated by confidence interval). This observed variance may be due to the inter-subject variability within the groups. For example, the MDD patients group included subjects who classified as non-depressed on the BDI scale. Moreover, there were variations in medication status among the MDD patients, with three patients undergoing antidepressant therapy at the time of scanning. The control group also included one subject whose BDI score indicated mild depression. Hence, the high variability in graph measures seen at the macroscale may be linked to the influence of diverse environmental factors on network topology at the systems level. The previous results stress the critical need to take individual characteristics and environmental factors into account when interpreting network metrics at the macroscale.

4.2.2. Alterations in nodal topological features in large-scale networks of MDD patients

In the nodal graph theoretical analysis at the systems level, no significant results survived the correction of multiple comparison using FDR. While applying FDR to control for false positives in neuroimaging data is crucial (Genovese et al., 2002; Nichols, 2012), it is interesting to emphasize certain trends in the data that could become more apparent in the presence of a larger sample and increased statistical power. Therefore, brain regions that exhibited changes in nodal graph measures at $p_{\text{uncorrected}} < 0.01$ will be highlighted for context and interpreted tentatively.

Only *BC*, a measure of influence and hubness, showed group differences in the whole-brain networks at $p_{\text{uncorrected}} < 0.01$. More specifically, macroscale networks of MDD patients exhibited a *BC* decrease in a region in IPS and an increase in AAIC. The IP sulcus is part of the dorsal FPN with a function typically linked to visuospatial attention, top-down control of attention allocation, and goal-directed behavior. It is involved in the cognitive selection of relevant sensory stimuli and guiding eye movement to filter out irrelevant information in the environment – selective attention (Szczepanski et al., 2013). Attentional processes are known to be affected in depression. Many MDD patients frequently report concentration difficulties and impaired cognition and attention, massively affecting the psychological and occupational aspects of their lives (Zuckerman et al., 2018). Moreover, the attentional bias towards processing negative stimuli, a distinctive symptom of MDD, is rooted in the disrupted allocation and reallocation of attention to behaviorally relevant cues (for reviews see Gotlib & Joormann, 2010; Kircanski & Gotlib, 2015). The hypoconnectivity of IPS was frequently reported in previous studies and has been linked to impaired goal-directed attention in depression (Keller et al., 2020). Dai et al (2023) also showed a decrease in right IPS centrality and nodal degree in first-episode drug-naïve MDD patients. Decreased nodal efficiency of IPS was also reported both in first-episode and recurrent MDD (Yang et al., 2021). The results reported in this analysis are in line with the previous research, indicating that the reduced IPS centrality may contribute to altered attentional modulation in MDD.

Conversely, AAIC showed increased centrality in networks of MDD patients compared to controls. Anterior agranular insula is one of the three main subdivisions of insula. It is a functionally heterogeneous region involved in interoceptive awareness, emotional processing, and cognitive control (Craig, 2002; Mutschler et al., 2009; Phan et al., 2002; Molnar-Szakacs & Uddin, 2022). It constitutes a core region in the SN with a flexible functional connection profile which allows it to orchestrate activity of major functional brain networks such as the DMN and the CCN (Molnar-Szakacs & Uddin, 2022; Menon et al., 2023). This explains how the anterior insula can serve as a global functional hub for channeling and integrating information across multiple cognitive domains (Molnar-Szakacs & Uddin, 2022; Uddin et al., 2017). AAIC is frequently reported as a region that is highly implicated in depression (Gong & He, 2015; Hamilton et al., 2012; Zhang et al., 2011; Zheng et al., 2015). For instance, two studies reported a higher nodal *degree* in anterior insula in both adult MDD and medication-naïve adolescent depressed patients compared to a control group (Jin et al., 2011; Zheng et al.,

2015). Interestingly, an increase in anterior insula's *centrality* was also reported in subjects with early life stress (Teicher et al., 2014), a key environmental risk factor in the development of MDD that is typically modulated by age, gender, and genetic factors (Heim et al., 2004; Kaufman et al., 2000). In addition, Jakab et al. (2012) demonstrated a leftward functional dominance of the anterior insula enhancing the sensitivity of functional analyses to detect topological changes on the left hemisphere. This observation could potentially account for the unilateral differential centrality in the left AAIC detected in this study. Taken together, these reports align with the results presented in this work that suggest a trend towards increase *BC* in AAIC in brain networks of MDD patients. Hubs are elements of integration. Consequently, the observed overall trend of increased integration detected in large-scale networks of depressed patients in this study might be mainly driven by this heightened *centrality* of this key hub AAIC. Given the tight connections of anterior insula to limbic areas, such as amygdala and orbitofrontal cortex (OFC), and its key role (as a switching lever) in modulating other networks like the DMN and CCN, the observed increase in its *centrality*/*hubness* might be involved in the exaggerated salience response to negative stimuli frequently observed in depression, along with the disturbed contextual and reappraisal processes. A further dissect of the connectivity profile of the anterior insula in future research would be interesting to determine the mechanism behind AAIC implication in depression by investigating the regions or networks between which AAIC mediates integration of information. Another plausible explanation for the increased *centrality* of AAI in MDD is that the anterior insula may need to exert greater control to compensate for the suboptimal regulation and switching between the brain's three major large-scale networks in the depressed brain: the SN, DMN and CCN.

4.2.3. General remarks on the sample

In the MRI study, subjects were recruited several years after their initial diagnosis and hospitalization. At the time of recruitment, the subjects of the patient group differed in their medication status and BDI scores. This indicated a variation in the influence of environmental factors between the patients. Both genetics and environmental factors can exert their effect on macroscale network topology and organization. It is therefore not possible to determine whether the phenotypic topological changes observed between groups in this study are due to genetic variations or to environmental contributions, or an interplay of both. A number of twin and association studies have investigated the genetic basis of human brain network

organization and suggested region-dependent genetic influence where connectivity of some neural nodes, particularly hubs and rich clubs, is under tighter genetic control compared to non-hub regions (Arnatkeviciute et al., 2021). Accordingly, one could argue that the alterations observed in the anterior insula, a key hub in the brain, is mainly influenced by depression-related genetic variations. However, it is not possible to verify such a claim in our data, especially given the analysis's low power. Discerning the nuanced impact of genetics and environment on network organization in future investigations holds considerable interest and promises a deeper insight into the etiology of depression.

Lastly, we note that the two experimental groups differed in terms of their BMI, with the patient group exhibiting higher BMI on average. This finding is not surprising as it has been shown that overweight and obesity share a bidirectional relationship with MDD, where one disorder could contribute to the development of the other (Luppino et al., 2010). Some studies demonstrated a link between high BMI and alteration in the connectivity and topology of large-scale brain networks (Coveleskie et al., 2015; Park et al., 2015). While BMI should be considered as a confounding variable in our macroscale analysis, its specific effect on any group differences in network organization is still unclear.

4.3. Integrated micro-macro view

In this scale-bridging investigation, microscale networks of depressed patients showed significantly diminished segregation (*C*) and overall node degree (*ANDeg*) compared to those of controls. A trend of decreased integration (E_{glob}) was also observed in patient-derived microcircuits. On the systems level, however, significant group differences were absent, although an opposing pattern to that observed on the microscale is detected: increased integration and overall node degree in large-scale networks of depressed patients compared to those of controls. It is therefore difficult to address the multiscale association in our data given the absence of significant group differences at the macroscale. Further research with a larger sample size is warranted to confirm the tendencies we observed in the macroscale data.

For the sake of argument, let's assume that the macroscale changes observed here represent the ground truth. That would mean that large-scale networks in depression either do not show any topological differences compared to controls, or they show reduced integration and degree.

In both cases, network topology at the macroscale diverges from that observed at the microscale data. What could be the reason of these different, sometimes contrasting, patterns? These between-scale discrepancies can emerge as a result of inherent differences in three main aspects: the spatial scale itself, the method used to capture network topology, and the underlying mechanisms governing network organization. This section will include a discussion of these aspects.

Differences between micro and macro network organization might be due to the inherent differences in the scale of the neural elements that define the network nodes. At the microscale, nodes represent individual neurons interacting by means of axonal projections and synaptic transmission. At the macroscale, network nodes represent brain regions connected through bundles of white matter or fibre tracts. Albeit the different scales of granularity, prior investigations proposed that fundamental principles of network organization are conserved across scales (Scholtens et al., 2022). That means that the topological variation observed in this study might not necessarily be a result of differences in organization level (cell-cell vs region-region communication). However, our microscale 2D cultures consisted of only neuronal cells. These 2D neuronal monocultures lack the cytoarchitecture and functional complexity of the native 3D brain tissue which stems from the diverse neural cell types and the wide range of cell-cell and cell-extracellular matrix (ECM) interaction taking place in the brain (Dingle et al., 2020; Zhuang et al., 2018). One highly important, non-neuronal cell type that is absent in our cultures is glia. Neuron-glia interaction is crucial for signal transmission (Araque et al., 1998) and synaptic formation and plasticity (Araque et al., 1999; Papouin et al., 2017; Pfrieger & Barres, 1997), ultimately influencing network functional organization. In fact, glial cell dysfunction has been implicated in many psychiatric disorders including MDD (Di Benedetto & Rupprecht, 2013; Rial et al., 2016; Wang et al., 2017). Therefore, any differences in network topology we observe between scales might be influenced by these inherent distinctions in the microenvironment wherein the network nodes are situated.

In this work, we used Ca^{2+} imaging and fMRI techniques to capture neuronal networks at the micro and macroscale, respectively. The BOLD signal detected by fMRI is an indirect measure of regional neural activity. Changes in BOLD signal arises from haemodynamic changes at functionally active regions. These haemodynamic changes include changes in blood flow, volume, and magnetic properties (Kim & Ogawa, 2012; Pauling & Coryell, 1936).

Several attempts have been made to understand the neural and biophysical components that contribute to the BOLD response (Kim & Ogawa, 2012; Logothetis et al., 2001). One major neural component is local field potential (LFP), which represents the aggregated electrical signal of extracellular dendritic potentials originating from a large population of neurons. Is it crucial to note that the neural component in BOLD signal is often contaminated by non-neuronal components, e.g., head motion, physiological noise (respiration, pulse), and magnetic field instability. This requires meticulous data preprocessing practices to ensure thorough cleaning of fMRI data while preserving the integrity of the neural component (Caballero-Gaudes & Reynolds, 2017; Esteban et al., 2019). In contrast to BOLD, Ca^{2+} signal reflects the activity of individual neurons detected by monitoring their intracellular Ca^{2+} dynamics (Grienberger & Konnerth, 2012). Ca^{2+} is a versatile ion involved in a wide range of cellular functions including neurotransmitter release (Neher & Sakaba, 2008), synaptic plasticity (Zucker, 1999), and transcriptional regulation. Ca^{2+} signal can reflect neural activity at the soma as well as at the synaptic level (Grienberger & Konnerth, 2012; Li et al., 2017). Despite having varying underlying mechanisms, Ca^{2+} and BOLD signals show strong correspondence when the two responses are measured simultaneously in animals (Lake et al., 2020; Ma et al., 2022). Additionally, calcium dynamics (whether in neurons or astrocytes) were shown to contribute to the haemodynamic response of fMRI (Tesler et al., 2023). In this light, and given the robust cleaning we performed on fMRI data, it is unlikely that the cross-scale discrepancies we found in functional network organization are related to methodological differences.

The third potential source of micro-macro differences in network topology involves the varying degree of influence of genetics and environmental factors on network organization in our two datasets. In our microscale data, we assume that the group differences we observe are mainly attributed to differential genetic influence in depression. At this scale and with the iPSC technology used, the environmental influence is supposedly negligible given the epigenetic memory reset during the reprogramming of the fibroblasts (Garbett et al., 2015; Soliman et al., 2017). On the other hand, in the fMRI data, both genetic and environmental factors contribute to group differences (Reineberg et al., 2020; Yang et al., 2016), making it increasingly difficult to disentangle the specific impact of each of these factors on network topology. In other words, it remains unclear whether the observed changes at the macroscale are primarily linked to the pathophysiological processes of MDD or if they are largely influenced by the treatment, given that the patients in this study had previously received or are currently receiving antidepressants.

This means that the observed cross-scale differences might be attributed to differences in the genetic and environmental influence on the two datasets.

Even in the absence of differences in the three factors discussed above (scale and microenvironment, measuring method, and underlying influential factors), patterns of network topology can still differ across scales. This is due to the complex nature of cross-scale interaction involving a range of potential dynamics. One potential and straightforward mechanism of between-scale relationship is that the topological changes at the microscale may persist to the macroscale and manifest similarly. However, that is not always the case. Patterns of brain organization in different scales could still diverge. In fact, alterations at one level might trigger adaptive plasticity mechanisms aimed at mitigating the pathological process and constraining or managing its progression (van den Heuvel et al., 2019). One could argue that the observed macroscopic trend of increased E_{glob} and *ANDeg* in MDD is indicative of such compensatory mechanism. This mechanism could potentially serve as a driving force aimed at reconciling the inherent reduction in integration and neuron-to-neuron functional connections within microscale networks of MDD patients by establishing more functional connections linking large-scale brain regions and enhancing efficiency at the macroscale. The noted heightened *centrality* of the AAIC in depression can also be explained within this compensatory framework. Arguably, the AAIC increases its influence in MDD patients as an attempt to counteract the depression-related altered modulation of dynamical switching between large-scale functional networks associated with high-level cognitive processes. However, it is essential to interpret these macroscale findings and their relation to the cellular findings with caution, given their lack of statistical significance in the current analysis. Attempting to replicate this study with larger sample size would yield valuable insights into the complex dynamic interplay among the distinct spatial scales of functional network organization of the brain.

4.4. Limitations and methodological considerations

This study is subject to a number of limitations common to both experiments on the micro and macroscale. Firstly, the non-depressed status of the control cohort was determined solely by self-reported absence of any history of depression. That means we were unable to control for the potential genetic or environmental risk factors that may have been present in the control group and may have caused a predisposition for depression. Secondly, given that the subjects in the control group were chosen to be paired with MDD patients in terms of age and sex, the inter-subject variability in age, lifestyles, genetics, and physiology limits this study.

The experiment at the cellular level suffered from a specific set of constraints. The analysis at that level demonstrated an overall higher sensitivity to detect topological differences within larger networks, as evident by the increased significance of post-hoc tests at larger network sizes. However, it remains unclear why this heightened sensitivity was not consistently observed across different thresholds. Additionally, the analysis was constrained by the number of nodes within the networks. Attempting to include larger network sizes (exceeding 47 nodes) resulted in an insufficient number of subjects for a meaningful statistical analysis. Consequently, this restricted the generalization of our results to networks with number of nodes higher than 47. This was in part due to the high magnification of the microscope objective used. An objective with a lower magnification would have provided a wider field of view with a higher number of active neurons and allowed for a better estimation of network organization in culture. Nevertheless, even with a limited field of view capturing only tens of active neurons, we still detect significant network alterations. Another methodological limitation in the microscale experiment involves the use of pure neuronal cultures. While human-derived monocultures of neurons used in this work provide a powerful tool to study psychiatric disorders that is superior to animal models and post-mortem tissues, they represent an oversimplification of the human brain tissue. Potential alternatives include hiPSC-derived co-cultures of neurons and glial cells, or 3D cultures, whether biology-based such as spheroids and organoids, or engineering-based such as scaffold and microfluidic platforms. These modelling options all carry a better resemblance to brain tissues and provide an environment that supports the interaction between different cell types which is essential for neuronal health, functionality, and dynamics (Falk et al., 2016; Feldt et al., 2010; Fields & Stevens-Graham, 2002; Lemke, 2001; Ma et al., 2005).

One major constraint of this study on the macroscale is the small sample size, resulting in underpowered statistical analysis, which limited the interpretability of the results on the systems level. It is important to note that this study should be regarded as exploratory, given the inability to recruit a larger number of subjects, despite our best efforts within these constraints. The inter-individual differences between the subjects of the patient group, specifically in terms of their BDI scores and medication status, may have contributed to the low statistical power/sensitivity of the analysis. To attain better discernible differences in network topological features and allow better interpretability, subsequent investigations ought to consider replicating this work with larger sample size and with fMRI scans obtained closer to hospital admission to insure a homogeneous sample with minimal effect of therapeutic intervention on network architecture.

4.5. Future outlook

This work sets the stage for future cross-scale investigations, leveraging cutting-edge technologies to describe how network topology and behavior connect across scales and how this link is influenced in disease. Such technologies include utilizing iPSC-derived human neural tissue that offers a closer approximation to native brain tissue such as 3D cultures of brain organoids. Integrating iPSC-technology with tract-tracing and genetic labelling methods, which were not available for this study, can enhance our understanding of the structural aspect of microscale networks. Combining this with whole-brain DWI of the same subjects enables a comprehensive multiscale investigation of this underlying structural architecture. When coupled with functional investigations, these approaches can give insights into structural-functional interaction at different spatial granularities that is especially informative in the context of psychopathologies.

Employing multiscale network models to explore brain dynamics and how it is affected by altered network topology constitute an interesting line of research that can provide valuable intuition into disease-related brain dysfunction. This is particularly important as the topology of the network shapes its dynamic repertoire and governs the emergence of synchronous behavior whether at the cellular (Poli et al., 2015; Wang, 2011; Yamamoto et al., 2018) or systems level (Breakspear & Stam, 2005; Meunier et al., 2010; Zhou et al., 2006). Several lines of evidence at whole-brain level have linked MDD to altered temporal coordination and

reduced dynamical range rendering the network less flexible and more prone to get “stuck” in a particular state – the depressive state (Alonso Martínez, Deco, et al., 2020; Alonso Martínez, Marsman, et al., 2020; Yang et al., 2022). Thus, exploring the nature of this altered dynamics and its relation to aberrations in network topology across scales is relevant to understand MDD mechanism and the emergence of its behavioral consequences. For such enquiries of dynamics at the cellular level, *in vitro* techniques like MEAs or the application of voltage-sensitive dyes emerge as preferred choice over calcium imaging (Bonifazi & Massobrio, 2019; Chemla & Chavane, 2010). This preference stems from their ability to offer superior temporal resolution (single action potential) and broader dynamic range. Moreover, MEAs feature a fixed number of electrodes that are considered as network’s nodes, effectively resolving the issue of variable nodes count within each *in vitro* culture that was faced in this study.

This scale-bridging approach is crucial for elucidating the micro-macro association and thereby gaining deeper insights into the multiscale disease processes affecting neural network organization and their impact on behavior. The utilization of iPSCs technology provides a novel human cellular model for probing microscale network organization, a resource that was previously not available. This is complemented by integrating neuroimaging methods like fMRI to capture network topology at the systems level.

Another intriguing direction for research is to examine the effect of varying biological processes at the cellular level on multiscale network topology in mental illnesses. With an access to iPSC-derived neuronal tissues, studying the influence of genetic variation, altered electrophysiology and bioenergetics in depression on micro and macroscale alterations in functional network topology is now feasible. This can provide deeper insights into the genetic control on topology, the direct relation between altered neuronal function and network formation and interaction.

Continued advancements in brain modelling and simulation and increased data availability will support cross-scale investigations, promising a comprehensive understanding of the complex multiscale relationship and how it unfolds in disease development and progression (D′Angelo & Jirsa, 2022). iPSC-driven neuronal data can enrich the current neurobiological knowledge, e.g., in biophysics, 3D morphology, and membrane properties, that is used to replicate neuronal function and dynamics in simulated models of brain microcircuits.

By integrating microscale computational models with whole-brain models reconstructed from MRI, EEG, and MEG datasets, the micro-macro relationship can be simulated. This approach enables prediction about the influence of specific cellular processes such as genetic variations or drug-receptor interactions on macroscale network function and dynamics, contributing to a profound understanding of brain function. Multiscale brain modelling not only has its cutting-edged potentials in personalized medicine through the generation of brain digital twins for each patient, but it also contributes massively to the field of artificial intelligence and robotics as it offers means for modeling adaptive behaviors.

Multiscale network neuroscience, especially in the context of psychiatry, is still in its infancy but making consistent strides. Increased efforts are being made to build tailored multiscale models of brain networks that effectively bridge cellular attributes of neural networks with their higher-level, coarse-grained counterparts to establish a comprehensive/holistic understanding of brain connectivity, its functional implications, and its consequences for cognition and collective behavior. However, it is important to acknowledge that these endeavors are not devoid of limitations and challenges. One major challenge involves the inherent complexity when trying to address and model different levels of biological information, rendering accurate models more complex and harder to interpret. Not to mention that any network model will be sensitive to the underlying network structure. That means that between-study variations in node definition and the choice of brain parcellation will have a great impact on the resultant topological properties of the network. An additional challenge is the cross-sectional nature of most of the multiscale investigation that neglects the chronological aspect of the disease. In other words, these studies provide a snapshot at a given point in time and fail to depict how these disease-related multiscale mechanisms have developed and progressed over time. The advancement of computational methodologies and data-acquisition techniques will be instrumental in driving the field forward. Furthermore, the growing availability of open datasets will allow for all numerous comparisons between multiscale network features not just of combining micro and macro features of network organization but also linking other genomics, cytoarchitecture, electrophysiology and bioenergetics factors to network connectivity and topology. Bringing data together from different levels of granularities into the same reference space is crucial for an integrative understanding of brain function and dynamics and for delineating the intricate causal chain from gene to cell to network to collective behavior, both in health and in the context of mental disorders.

Conclusion

The current work marks the pioneering effort to explore multiscale alterations in functional network topology in MDD. The novelty of our approach lies in our human cellular model that was developed by reprogramming fibroblasts derived from the same group of subjects that were later recruited for a whole-brain fMRI scanning session. Our investigation sought to bridge the gap between these distinct but interdependent scales of inquiry, as a comprehensive understanding of the disorder's etiology is unlikely to be achieved by considering single scales in isolation. Together, the findings of this study align with previous research, reaffirming the presence of altered functional network topology in MDD. Notably, such alterations primarily manifested at the cellular level, characterized by decreased segregation capacity coupled with a reduction in overall node degree. Macroscale networks of depressed patients on the systems level showed a contrasting trend of increased integration and overall nodal connections, suggesting a potential compensatory mechanism of micro-macro scale association that needs to be validated in future investigations. On the nodal level, this work highlights changes in regional *BC* in macroscale networks of MDD patients, featuring a reduction in the IP region and an increase in AAIC, adding to the existing body of evidence implicating these regions in depression.

This scale-bridging approach is pivotal for advancing our understanding of the multiscale mechanisms of depression, ultimately providing valuable insights to inform diagnostic and therapeutic interventions.

Acknowledgements

"So long, and thanks for all the fish!"

I would like to express my deepest gratitude to my supervisors Prof. Dr. Christian Wetzel and Prof. Dr. Jens Schwarzbach. It was from their brilliant ideas that this project has originated and I am genuinely thankful for having had the opportunity to work on such an exciting project under their supervision. I would like to thank Christian for always being there to help and for his brilliant insights that assisted me through the exciting world of molecular neuroscience. A huge thanks to Jens, for his contagious scientific enthusiasm and for the invaluable professional and personal advice and guidance he provided throughout the years.

I would also like to thank Prof. Dr. Neumann for accepting to be among my mentors. I deeply appreciate the valuable input and the support she has provided.

Furthermore, I am grateful for the support I got from my colleagues at the Molecular Neuroscience lab. Special thanks to Dr. Vladimir Milenkovic for his immense methodological support and positive energy, to our lab technician Tatjana Jahner for helping me around the lab, to Anna Häb and her amazing efforts in establishing a protocol for happy neurons and for guiding me as I commenced on my first cell culture experience, and finally to my friend Carmen Constantinescu, for her lovely company and kind and encouraging words when I most needed them.

A wholehearted thank you goes to all my friends and colleagues in the Biomedical imaging lab. In particular, I want to thank the amazing Dr. Viola Wagner, who not only made the recruitment and scanning of fMRI subjects possible, but also provided immense mental support and was always there for me with open arms and great food. I am also thankful for all the help and support I got from Dr. Simon Wein. His computational insights and programming expertise were most valuable for this work. Big thanks to my dear friend Aino Alahäivälä. Thank you for the amazing company, the stimulating talks, and for Finish chocolate. A deep gratitude goes of course to Nadia Falhani, my fellow PhD buddy who was there at every laughter, every uncertainty, and every existential crisis. Thank you for existing! This would not have been bearable without you.

Special thanks go to my friends outside of the lab, especially to my dearest Dr. Nairveen Ali, who was by my side every step of the way. I am forever thankful for her care and support and for being my extended family away from home. Thank you to Zuzanna Kabulska for her unequivocal friendship and support, for being a good listener and for her contagious excitements towards science and life in general. I would also like to extend my thanks to Souad Ramadan, Asmaa Khdeir, Lama Al Khouja, Sabine Huber, and Markus Becker who endured a high dose of complaining and never hesitated to offer help when needed.

Last but not least, I would like to express my tremendous gratitude to my parents Mohamad and Dina, and my dear siblings Dania and Fuad for their unconditional love and support and for always believing in me. Your encouragement and guidance have always defied the distances between us and I am utterly grateful to have you in my life. Big thanks also to my aunt Baria who is always a role model in strength and perseverance. Finally, to the loved ones I lost along the way, to my beloved grandmother Dalal and to uncle Safwan. I know you would have been proud of me to reach the end of this path. I will never forget the love and support you have given me and will always cherish your memory.

References

American Psychiatric Association. (2013). Diagnostic and statistical manual of mental disorders (5th ed.). Arlington, VA: Author.

Achard, S. (2006). A Resilient, Low-Frequency, Small-World Human Brain Functional Network with Highly Connected Association Cortical Hubs. *Journal of Neuroscience*, *26*(1), 63–72. https://doi.org/10.1523/JNEUROSCI.3874-05.2006

Achard, S., & Bullmore, E. (2007). Efficiency and Cost of Economical Brain Functional Networks. *PLOS Computational Biology*, *3*(2), e17. https://doi.org/10.1371/journal.pcbi.0030017

Alexopoulos, G. S., Hoptman, M. J., Kanellopoulos, D., Murphy, C. F., Lim, K. O., & Gunning, F. M. (2012). Functional connectivity in the cognitive control network and the default mode network in late-life depression. *Journal of Affective Disorders*, *139*(1), 56–65. https://doi.org/10.1016/j.jad.2011.12.002

Alonso Martínez, S., Deco, G., Ter Horst, G. J., & Cabral, J. (2020). The Dynamics of Functional Brain Networks Associated With Depressive Symptoms in a Nonclinical Sample. *Frontiers in Neural Circuits*, *14*. https://www.frontiersin.org/articles/10.3389/fncir.2020.570583

Alonso Martínez, S., Marsman, J.-B. C., Kringelbach, M. L., Deco, G., & ter Horst, G. J. (2020). Reduced spatiotemporal brain dynamics are associated with increased depressive symptoms after a relationship breakup. *NeuroImage: Clinical*, *27*, 102299. https://doi.org/10.1016/j.nicl.2020.102299

Alstott, J., Breakspear, M., Hagmann, P., Cammoun, L., & Sporns, O. (2009). Modeling the Impact of Lesions in the Human Brain. *PLOS Computational Biology*, *5*(6), e1000408. https://doi.org/10.1371/journal.pcbi.1000408

Araque, A., Parpura, V., Sanzgiri, R. P., & Haydon, P. G. (1998). Glutamate-dependent astrocyte modulation of synaptic transmission between cultured hippocampal neurons. *European Journal of Neuroscience*, *10*(6), 2129–2142. https://doi.org/10.1046/j.1460-9568.1998.00221.x

Araque, A., Sanzgiri, R. P., Parpura, V., & Haydon, P. G. (1999). Astrocyte-induced modulation of synaptic transmission. *Canadian Journal of Physiology and Pharmacology*, *77*(9), 699–706. https://doi.org/10.1139/y99-076

Arenas, A., Díaz-Guilera, A., & Pérez-Vicente, C. J. (2006). Synchronization Reveals Topological Scales in Complex Networks. *Physical Review Letters*, *96*(11), 114102. https://doi.org/10.1103/PhysRevLett.96.114102

Arnatkeviciute, A., Fulcher, B. D., Bellgrove, M. A., & Fornito, A. (2021). Where the genome meets the connectome: Understanding how genes shape human brain connectivity. *NeuroImage*, *244*, 118570. https://doi.org/10.1016/j.neuroimage.2021.118570

Attwell, D., & Laughlin, S. B. (2001). An energy budget for signaling in the grey matter of the brain. *Journal of Cerebral Blood Flow and Metabolism: Official Journal of the International Society of Cerebral Blood Flow and Metabolism*, *21*(10), 1133–1145. https://doi.org/10.1097/00004647-200110000-00001

B. Di Benedetto & R. Rupprecht. (2013). Targeting Glia Cells: Novel Perspectives for the Treatment of Neuropsychiatric Diseases. *Current Neuropharmacology*, *11*(2), 171–185.

Bae, J. N., MacFall, J. R., Krishnan, K. R. R., Payne, M. E., Steffens, D. C., & Taylor, W. D. (2006). Dorsolateral Prefrontal Cortex and Anterior Cingulate Cortex White Matter Alterations in Late-Life Depression. *Biological Psychiatry*, *60*(12), 1356–1363. https://doi.org/10.1016/j.biopsych.2006.03.052

Bardy, C., Greenberg, Z., Perry, S. W., & Licinio, J. (2020). Personalized psychiatry with human iPSCs and neuronal reprogramming. In *Personalized Psychiatry* (pp. 127–146). Elsevier. https://doi.org/10.1016/B978-0-12-813176-3.00012-2

Barré-Sinoussi, F., & Montagutelli, X. (2015). Animal models are essential to biological research: Issues and perspectives. *Future Science OA*, *1*(4). https://doi.org/10.4155/fso.15.63

Bassett, D. S., Meyer-Lindenberg, A., Achard, S., Duke, T., & Bullmore, E. (2006). Adaptive reconfiguration of fractal small-world human brain functional networks. *Proceedings of the National Academy of Sciences*, *103*(51), 19518–19523. https://doi.org/10.1073/pnas.0606005103

Bassett, D. S., Zurn, P., & Gold, J. I. (2018). On the nature and use of models in network neuroscience. *Nature Reviews Neuroscience*, *19*(9), Article 9. https://doi.org/10.1038/s41583-018-0038-8

Beck, A. T. (1961). An Inventory for Measuring Depression. *Archives of General Psychiatry*, *4*(6), 561. https://doi.org/10.1001/archpsyc.1961.01710120031004

Beck, A. T. (2005). The current state of cognitive therapy: A 40-year retrospective. *Archives of General Psychiatry*, *62*(9), Article 9. https://doi.org/10.1001/archpsyc.62.9.953

Benjamini, Y., & Hochberg, Y. (1995). Controlling the False Discovery Rate: A Practical and Powerful Approach to Multiple Testing. *Journal of the Royal Statistical Society. Series B (Methodological)*, *57*(1), 289–300.

Berman, R. M., Cappiello, A., Anand, A., Oren, D. A., Heninger, G. R., Charney, D. S., & Krystal, J. H. (2000). Antidepressant effects of ketamine in depressed patients. *Biological Psychiatry*, *47*(4), 351–354. https://doi.org/10.1016/S0006-3223(99)00230-9

Bisio, M., Bosca, A., Pasquale, V., Berdondini, L., & Chiappalone, M. (2014). Emergence of Bursting Activity in Connected Neuronal Sub-Populations. *PLOS ONE*, *9*(9), e107400. https://doi.org/10.1371/journal.pone.0107400

Boccaletti, S., Latora, V., Moreno, Y., Chavez, M., & Hwang, D.-U. (2006). Complex networks: Structure and dynamics. *Physics Reports*, *424*(4), 175–308. https://doi.org/10.1016/j.physrep.2005.10.009

Bohr, I. J., Kenny, E., Blamire, A., O'Brien, J. T., Thomas, A. J., Richardson, J., & Kaiser, M. (2013). Resting-State Functional Connectivity in Late-Life Depression: Higher Global Connectivity and More Long Distance Connections. *Frontiers in Psychiatry*, *3*. https://doi.org/10.3389/fpsyt.2012.00116

Bonacich, P. (1972). Factoring and weighting approaches to status scores and clique identification. *Journal of Mathematical Sociology*. https://www.tandfonline.com/doi/abs/10.1080/0022250X.1972.9989806

Bonifazi, P., & Massobrio, P. (2019). Reconstruction of Functional Connectivity from Multielectrode Recordings and Calcium Imaging. In M. Chiappalone, V. Pasquale, & M. Frega (Eds.), *In Vitro Neuronal Networks: From Culturing Methods to Neuro-Technological Applications* (pp. 207–231). Springer International Publishing. https://doi.org/10.1007/978-3-030-11135-9_9

Brady, R. O., Tandon, N., Masters, G. A., Margolis, A., Cohen, B. M., Keshavan, M., & Öngür, D. (2017). Differential Brain Network Activity Across Mood States in Bipolar Disorder. *Journal of Affective Disorders*, *207*, 367–376. https://doi.org/10.1016/j.jad.2016.09.041

Breakspear, M., & Stam, C. J. (2005). Dynamics of a Neural System with a Multiscale Architecture. *Philosophical Transactions: Biological Sciences*, *360*(1457), 1051–1074.

Bressler, S. L., & Menon, V. (2010). Large-scale brain networks in cognition: Emerging methods and principles. *Trends in Cognitive Sciences*, *14*(6), 277–290. https://doi.org/10.1016/j.tics.2010.04.004

Briggman, K. L., Helmstaedter, M., & Denk, W. (2011). Wiring specificity in the direction-selectivity circuit of the retina. *Nature*, *471*(7337), 183–188. https://doi.org/10.1038/nature09818

Brodaty, H., Luscombe, G., Parker, G., Wilhelm, K., Hickie, I., Austin, M. P., & Mitchell, P. (2001). Early and late onset depression in old age: Different aetiologies, same phenomenology. *Journal of Affective Disorders*, *66*(2–3), Article 2–3. https://doi.org/10.1016/S0165-0327(00)00317-7

Buckner, R. L., & Krienen, F. M. (2013). The evolution of distributed association networks in the human brain. *Trends in Cognitive Sciences*, *17*(12), 648–665. https://doi.org/10.1016/j.tics.2013.09.017

Buckner, R. L., Sepulcre, J., Talukdar, T., Krienen, F. M., Liu, H., Hedden, T., Andrews-Hanna, J. R., Sperling, R. A., & Johnson, K. A. (2009). Cortical Hubs Revealed by Intrinsic Functional Connectivity: Mapping,

Assessment of Stability, and Relation to Alzheimer's Disease. *Journal of Neuroscience*, *29*(6), 1860–1873. https://doi.org/10.1523/JNEUROSCI.5062-08.2009

Bullmore, E., & Sporns, O. (2009). Complex brain networks: Graph theoretical analysis of structural and functional systems. *Nature Reviews Neuroscience*, *10*(3), Article 3. https://doi.org/10.1038/nrn2575

Bullmore, E., & Sporns, O. (2012). The economy of brain network organization. *Nature Reviews Neuroscience*, *13*(5), Article 5. https://doi.org/10.1038/nrn3214

Buzsáki, G., Geisler, C., Henze, D. A., & Wang, X.-J. (2004). Interneuron Diversity series: Circuit complexity and axon wiring economy of cortical interneurons. *Trends in Neurosciences*, *27*(4), 186–193. https://doi.org/10.1016/j.tins.2004.02.007

Caballero-Gaudes, C., & Reynolds, R. C. (2017). Methods for cleaning the BOLD fMRI signal. *NeuroImage*, *154*, 128–149. https://doi.org/10.1016/j.neuroimage.2016.12.018

Cardoso-Moreira, M., Sarropoulos, I., Velten, B., Mort, M., Cooper, D. N., Huber, W., & Kaessmann, H. (2020). Developmental Gene Expression Differences between Humans and Mammalian Models. *Cell Reports*, *33*(4), 108308. https://doi.org/10.1016/j.celrep.2020.108308

Cavalleri, L., Merlo Pich, E., Millan, M. J., Chiamulera, C., Kunath, T., Spano, P. F., & Collo, G. (2018). Ketamine enhances structural plasticity in mouse mesencephalic and human iPSC-derived dopaminergic neurons via AMPAR-driven BDNF and mTOR signaling. *Molecular Psychiatry*, *23*(4), Article 4. https://doi.org/10.1038/mp.2017.241

Chemla, S., & Chavane, F. (2010). Voltage-sensitive dye imaging: Technique review and models. *Journal of Physiology-Paris*, *104*(1), 40–50. https://doi.org/10.1016/j.jphysparis.2009.11.009

Cheng, W., Rolls, E. T., Qiu, J., Liu, W., Tang, Y., Huang, C. C., Wang, X. F., Zhang, J., Lin, W., Zheng, L., Pu, J. C., Tsai, S. J., Yang, A. C., Lin, C. P., Wang, F., Xie, P., & Feng, J. (2016). Medial reward and lateral non-reward orbitofrontal cortex circuits change in opposite directions in depression. *Brain*, *139*(12), Article 12. https://doi.org/10.1093/brain/aww255

Chklovskii, D. B. (2004). Synaptic Connectivity and Neuronal Morphology: Two Sides of the Same Coin. *Neuron*, *43*(5), 609–617. https://doi.org/10.1016/j.neuron.2004.08.012

Churchland, P. S., & Sejnowski, T. J. (1992). *The Computational Brain*. MIT Press.

Cipriani, A., Furukawa, T. A., Salanti, G., Geddes, J. R., Higgins, J. P., Churchill, R., Watanabe, N., Nakagawa, A., Omori, I. M., McGuire, H., Tansella, M., & Barbui, C. (2009). Comparative efficacy and acceptability of 12 new-generation antidepressants: A multiple-treatments meta-analysis. *The Lancet*, *373*(9665), 746–758. https://doi.org/10.1016/S0140-6736(09)60046-5

Cocchi, L., Zalesky, A., Fornito, A., & Mattingley, J. B. (2013). Dynamic cooperation and competition between brain systems during cognitive control. *Trends in Cognitive Sciences*, *17*(10), 493–501. https://doi.org/10.1016/j.tics.2013.08.006

Collin, G., Sporns, O., Mandl, R. C. W., & van den Heuvel, M. P. (2014). Structural and Functional Aspects Relating to Cost and Benefit of Rich Club Organization in the Human Cerebral Cortex. *Cerebral Cortex*, *24*(9), 2258–2267. https://doi.org/10.1093/cercor/bht064

Collo, G., Cavalleri, L., Chiamulera, C., & Merlo Pich, E. (2018). (2R,6R)-Hydroxynorketamine promotes dendrite outgrowth in human inducible pluripotent stem cell-derived neurons through AMPA receptor with timing and exposure compatible with ketamine infusion pharmacokinetics in humans. *NeuroReport*, *29*(16), 1425. https://doi.org/10.1097/WNR.0000000000001131

Collo, G., Cavalleri, L., Chiamulera, C., & Merlo Pich, E. (2019). Ketamine increases the expression of GluR1 and GluR2 α-amino-3-hydroxy-5-methy-4-isoxazole propionate receptor subunits in human dopaminergic neurons differentiated from induced pluripotent stem cells. *NeuroReport*, *30*(3), 207–212. https://doi.org/10.1097/WNR.0000000000001185

Collo, G., & Merlo Pich, E. (2018). Ketamine enhances structural plasticity in human dopaminergic neurons: Possible relevance for treatment-resistant depression. *Neural Regeneration Research*, *13*(4), 645–646. https://doi.org/10.4103/1673-5374.230288

Colpo, G. D., & Teixeira, A. L. (2021). Induced Pluripotent Stem Cells (iPSCs) Technology: Potential Targets for Depression. In Y.-K. Kim (Ed.), *Major Depressive Disorder: Rethinking and Understanding Recent Discoveries* (pp. 493–501). Springer. https://doi.org/10.1007/978-981-33-6044-0_24

Coveleskie, K., Gupta, A., Kilpatrick, L. A., Mayer, E. D., Ashe-McNalley, C., Stains, J., Labus, J. S., & Mayer, E. A. (2015). Altered functional connectivity within the central reward network in overweight and obese women. *Nutrition & Diabetes*, *5*(1), Article 1. https://doi.org/10.1038/nutd.2014.45

Cowen, P. J. (2010). Not fade away: The HPA axis and depression. *Psychological Medicine*, *40*(1), 1–4. https://doi.org/10.1017/S0033291709005558

Craig, A. D. (2002). How do you feel? Interoception: the sense of the physiological condition of the body. *Nature Reviews Neuroscience*, *3*(8), Article 8. https://doi.org/10.1038/nrn894

Crossley, N. A., Mechelli, A., Scott, J., Carletti, F., Fox, P. T., McGuire, P., & Bullmore, E. T. (2014). The hubs of the human connectome are generally implicated in the anatomy of brain disorders. *Brain*, *137*(8), 2382–2395. https://doi.org/10.1093/brain/awu132

Cusin, C., & Dougherty, D. D. (2012). Somatic therapies for treatment-resistant depression: ECT, TMS, VNS, DBS. *Biology of Mood & Anxiety Disorders*, *2*(1), 14. https://doi.org/10.1186/2045-5380-2-14

Dai, Y.-R., Wu, Y.-K., Chen, X., Zeng, Y.-W., Li, K., Li, J.-T., Su, Y.-A., Zhu, L.-L., Yan, C.-G., & Si, T.-M. (2023). Eight-week antidepressant treatment changes intrinsic functional brain topology in first-episode drug-naïve patients with major depressive disorder. *Journal of Affective Disorders*, *329*, 225–234. https://doi.org/10.1016/j.jad.2023.02.126

D'Angelo, E., & Jirsa, V. (2022). The quest for multiscale brain modeling. *Trends in Neurosciences*, *45*(10), 777–790. https://doi.org/10.1016/j.tins.2022.06.007

Delaveau, P., Jabourian, M., Lemogne, C., Guionnet, S., Bergouignan, L., & Fossati, P. (2011). Brain effects of antidepressants in major depression: A meta-analysis of emotional processing studies. *Journal of Affective Disorders*, *130*(1), 66–74. https://doi.org/10.1016/j.jad.2010.09.032

Denk, W., Delaney, K. R., Gelperin, A., Kleinfeld, D., Strowbridge, B. W., Tank, D. W., & Yuste, R. (1994). Anatomical and functional imaging of neurons using 2-photon laser scanning microscopy. *Journal of Neuroscience Methods*, *54*(2), 151–162. https://doi.org/10.1016/0165-0270(94)90189-9

Dingle, Y.-T. L., Liaudanskaya, V., Finnegan, L. T., Berlind, K. C., Mizzoni, C., Georgakoudi, I., Nieland, T. J. F., & Kaplan, D. L. (2020). Functional Characterization of Three-Dimensional Cortical Cultures for In Vitro Modeling of Brain Networks. *iScience*, *23*(8), 101434. https://doi.org/10.1016/j.isci.2020.101434

Douet, V., Chang, L., Cloak, C., & Ernst, T. (2014). Genetic influences on brain developmental trajectories on neuroimaging studies: From infancy to young adulthood. *Brain Imaging and Behavior*, *8*(2), 234–250. https://doi.org/10.1007/s11682-013-9260-1

Downes, J. H., Hammond, M. W., Xydas, D., Spencer, M. C., Becerra, V. M., Warwick, K., Whalley, B. J., & Nasuto, S. J. (2012). Emergence of a Small-World Functional Network in Cultured Neurons. *PLOS Computational Biology*, *8*(5), e1002522. https://doi.org/10.1371/journal.pcbi.1002522

Drevets, W. C., Price, J. L., & Furey, M. L. (2008). Brain structural and functional abnormalities in mood disorders: Implications for neurocircuitry models of depression. *Brain Structure and Function*, *213*(1), 93–118. https://doi.org/10.1007/s00429-008-0189-x

Duman, R. S., & Aghajanian, G. K. (2012). Synaptic Dysfunction in Depression: Potential Therapeutic Targets. *Science*, *338*(6103), 68–72. https://doi.org/10.1126/science.1222939

Duman, R. S., Aghajanian, G. K., Sanacora, G., & Krystal, J. H. (2016). Synaptic plasticity and depression: New insights from stress and rapid-acting antidepressants. *Nature Medicine*, *22*(3), Article 3. https://doi.org/10.1038/nm.4050

Esteban, O., Markiewicz, C. J., Blair, R. W., Moodie, C. A., Isik, A. I., Erramuzpe, A., Kent, J. D., Goncalves, M., DuPre, E., Snyder, M., Oya, H., Ghosh, S. S., Wright, J., Durnez, J., Poldrack, R. A., & Gorgolewski, K. J. (2019). fMRIPrep: A robust preprocessing pipeline for functional MRI. *Nature Methods*, *16*(1), Article 1. https://doi.org/10.1038/s41592-018-0235-4

Falk, A., Heine, V. M., Harwood, A. J., Sullivan, P. F., Peitz, M., Brüstle, O., Shen, S., Sun, Y.-M., Glover, J. C., Posthuma, D., & Djurovic, S. (2016). Modeling psychiatric disorders: From genomic findings to cellular phenotypes. *Molecular Psychiatry*, *21*(9), Article 9. https://doi.org/10.1038/mp.2016.89

Farahani, F. V., Karwowski, W., & Lighthall, N. R. (2019). Application of Graph Theory for Identifying Connectivity Patterns in Human Brain Networks: A Systematic Review. *Frontiers in Neuroscience*, *13*. https://www.frontiersin.org/articles/10.3389/fnins.2019.00585

Fava, M., & Kendler, K. S. (2000). Major Depressive Disorder. *Neuron*, *28*(2), 335–341. https://doi.org/10.1016/S0896-6273(00)00112-4

Feldt, S., Bonifazi, P., & Cossart, R. (2011). Dissecting functional connectivity of neuronal microcircuits: Experimental and theoretical insights. *Trends in Neurosciences*, *34*(5), 225–236. https://doi.org/10.1016/j.tins.2011.02.007

Feldt, S., Wang, J. X., Shtrahman, E., Dzakpasu, R., Olariu, E., & Żochowski, M. (2010). Functional clustering in hippocampal cultures: Relating network structure and dynamics. *Physical Biology*, *7*(4), 046004. https://doi.org/10.1088/1478-3975/7/4/046004

Felleman, D. J., & Van Essen, D. C. (1991). Distributed Hierarchical Processing in the Primate Cerebral Cortex. *Cerebral Cortex*, *1*(1), 1–47. https://doi.org/10.1093/cercor/1.1.1

Fields, R. D., & Stevens-Graham, B. (2002). New Insights into Neuron-Glia Communication. *Science*, *298*(5593), 556–562. https://doi.org/10.1126/science.298.5593.556

Fischer, A. S., Keller, C. J., & Etkin, A. (2016). The Clinical Applicability of Functional Connectivity in Depression: Pathways Toward More Targeted Intervention. *Biological Psychiatry: Cognitive Neuroscience and Neuroimaging*, *1*(3), Article 3. https://doi.org/10.1016/j.bpsc.2016.02.004

Fischl, B. (2012). FreeSurfer. *NeuroImage*, *62*(2), 774–781. https://doi.org/10.1016/j.neuroimage.2012.01.021

Fornito, A., Zalesky, A., Bassett, D. S., Meunier, D., Ellison-Wright, I., Yücel, M., Wood, S. J., Shaw, K., O'Connor, J., Nertney, D., Mowry, B. J., Pantelis, C., & Bullmore, E. T. (2011). Genetic Influences on Cost-Efficient Organization of Human Cortical Functional Networks. *Journal of Neuroscience*, *31*(9), 3261–3270. https://doi.org/10.1523/JNEUROSCI.4858-10.2011

Fornito, A., Zalesky, A., & Breakspear, M. (2015). The connectomics of brain disorders. *Nature Reviews Neuroscience*, *16*(3), 159–172. https://doi.org/10.1038/nrn3901

Fornito, A., Zalesky, A., & Bullmore, E. (2016). *Fundamentals of Brain Network Analysis*. Academic Press.

Freeman, L. C. (1977). A Set of Measures of Centrality Based on Betweenness. *Sociometry*, *40*(1), 35–41. https://doi.org/10.2307/3033543

Frodl, T., Bokde, A. L. W., Scheuerecker, J., Lisiecka, D., Schoepf, V., Hampel, H., Möller, H.-J., Brückmann, H., Wiesmann, M., & Meisenzahl, E. (2010). Functional Connectivity Bias of the Orbitofrontal Cortex in Drug-Free Patients with Major Depression. *Biological Psychiatry*, *67*(2), 161–167. https://doi.org/10.1016/j.biopsych.2009.08.022

Fulcher, B. D., & Fornito, A. (2016). A transcriptional signature of hub connectivity in the mouse connectome. *Proceedings of the National Academy of Sciences*, *113*(5), 1435–1440. https://doi.org/10.1073/pnas.1513302113

Garbett, K. A., Vereczkei, A., Kálmán, S., Wang, L., Korade, Ž., Shelton, R. C., & Mirnics, K. (2015). Fibroblasts from patients with major depressive disorder show distinct transcriptional response to metabolic stressors. *Translational Psychiatry*, *5*(3), Article 3. https://doi.org/10.1038/tp.2015.14

Genovese, C. R., Lazar, N. A., & Nichols, T. (2002). Thresholding of Statistical Maps in Functional Neuroimaging Using the False Discovery Rate. *NeuroImage*, *15*(4), 870–878. https://doi.org/10.1006/nimg.2001.1037

Gibson, G. (2008). The environmental contribution to gene expression profiles. *Nature Reviews Genetics*, *9*(8), Article 8. https://doi.org/10.1038/nrg2383

Giovannucci, A., Friedrich, J., Gunn, P., Kalfon, J., Brown, B. L., Koay, S. A., Taxidis, J., Najafi, F., Gauthier, J. L., Zhou, P., Khakh, B. S., Tank, D. W., Chklovskii, D. B., & Pnevmatikakis, E. A. (2019). CaImAn an open source tool for scalable calcium imaging data analysis. *eLife*, *8*, e38173. https://doi.org/10.7554/eLife.38173

Glasser, M. F., Coalson, T. S., Robinson, E. C., Hacker, C. D., Harwell, J., Yacoub, E., Ugurbil, K., Andersson, J., Beckmann, C. F., Jenkinson, M., Smith, S. M., & Van Essen, D. C. (2016). A multi-modal parcellation of human cerebral cortex. *Nature*, *536*(7615), Article 7615. https://doi.org/10.1038/nature18933

Gong, Q., & He, Y. (2015). Depression, Neuroimaging and Connectomics: A Selective Overview. *Biological Psychiatry*, *77*(3), 223–235. https://doi.org/10.1016/j.biopsych.2014.08.009

Gotlib, I. H., & Joormann, J. (2010). Cognition and Depression: Current Status and Future Directions. *Annual Review of Clinical Psychology*, *6*(1), 285–312. https://doi.org/10.1146/annurev.clinpsy.121208.131305

Goulas, A., Uylings, H. B. M., & Hilgetag, C. C. (2017). Principles of ipsilateral and contralateral cortico-cortical connectivity in the mouse. *Brain Structure and Function*, *222*(3), 1281–1295. https://doi.org/10.1007/s00429-016-1277-y

Grewe, B. F., Langer, D., Kasper, H., Kampa, B. M., & Helmchen, F. (2010). High-speed in vivo calcium imaging reveals neuronal network activity with near-millisecond precision. *Nature Methods*, *7*(5), Article 5. https://doi.org/10.1038/nmeth.1453

Grienberger, C., & Konnerth, A. (2012). Imaging Calcium in Neurons. *Neuron*, *73*(5), 862–885. https://doi.org/10.1016/j.neuron.2012.02.011

Gupta, S., M-Redmond, T., Meng, F., Tidball, A., Akil, H., Watson, S., Parent, J. M., & Uhler, M. (2018). Fibroblast growth factor 2 regulates activity and gene expression of human post-mitotic excitatory neurons. *Journal of Neurochemistry*, *145*(3), 188–203. https://doi.org/10.1111/jnc.14255

Hagberg, A., Swart, P., & S Chult, D. (2008). *Exploring network structure, dynamics, and function using networkx* (LA-UR-08-05495; LA-UR-08-5495). Los Alamos National Lab. (LANL), Los Alamos, NM (United States). https://www.osti.gov/biblio/960616

Hagmann, P., Cammoun, L., Gigandet, X., Meuli, R., Honey, C. J., Wedeen, V. J., & Sporns, O. (2008). Mapping the Structural Core of Human Cerebral Cortex. *PLOS Biology*, *6*(7), e159. https://doi.org/10.1371/journal.pbio.0060159

Hagmann, P., Kurant, M., Gigandet, X., Thiran, P., Wedeen, V. J., Meuli, R., & Thiran, J.-P. (2007). Mapping Human Whole-Brain Structural Networks with Diffusion MRI. *PLOS ONE*, *2*(7), e597. https://doi.org/10.1371/journal.pone.0000597

Hamilton, J. P., Chen, M. C., & Gotlib, I. H. (2013). Neural systems approaches to understanding major depressive disorder: An intrinsic functional organization perspective. *Neurobiology of Disease*, *52*, undefined-undefined. https://doi.org/10.1016/j.nbd.2012.01.015

Hamilton, J. P., Etkin, A., Furman, D. J., Lemus, M. G., Johnson, R. F., & Gotlib, I. H. (2012). Functional Neuroimaging of Major Depressive Disorder: A Meta-Analysis and New Integration of Baseline Activation and Neural Response Data. *American Journal of Psychiatry*, *169*(7), 693–703. https://doi.org/10.1176/appi.ajp.2012.11071105

Hamilton, J. P., Furman, D. J., Chang, C., Thomason, M. E., Dennis, E., & Gotlib, I. H. (2011). Default-Mode and Task-Positive Network Activity in Major Depressive Disorder: Implications for Adaptive and Maladaptive Rumination. *Biological Psychiatry*, *70*(4), 327–333. https://doi.org/10.1016/j.biopsych.2011.02.003

Hamilton, M. (1960). A rating scale for depression. *Journal of Neurology, Neurosurgery, and Psychiatry*, *23*(1), 56. https://doi.org/10.1136/jnnp.23.1.56

He, Y., & Evans, A. (2010). Graph theoretical modeling of brain connectivity. *Current Opinion in Neurology*, *23*(4), 341. https://doi.org/10.1097/WCO.0b013e32833aa567

Hebb, D. O. (1949). *The organization of behavior*. Wiley.

Heim, C., Plotsky, P. M., & Nemeroff, C. B. (2004). Importance of Studying the Contributions of Early Adverse Experience to Neurobiological Findings in Depression. *Neuropsychopharmacology*, *29*(4), Article 4. https://doi.org/10.1038/sj.npp.1300397

Hilgetag, C. C., Medalla, M., Beul, S. F., & Barbas, H. (2016). The primate connectome in context: Principles of connections of the cortical visual system. *NeuroImage*, *134*, 685–702. https://doi.org/10.1016/j.neuroimage.2016.04.017

Holmes, S. E., Scheinost, D., Finnema, S. J., Naganawa, M., Davis, M. T., DellaGioia, N., Nabulsi, N., Matuskey, D., Angarita, G. A., Pietrzak, R. H., Duman, R. S., Sanacora, G., Krystal, J. H., Carson, R. E., & Esterlis, I. (2019). Lower synaptic density is associated with depression severity and network alterations. *Nature Communications*, *10*(1), Article 1. https://doi.org/10.1038/s41467-019-09562-7

Holtzheimer, P. E., & Mayberg, H. S. (2011). Stuck in a rut: Rethinking depression and its treatment. *Trends in Neurosciences*, *34*(1), 1–9. https://doi.org/10.1016/j.tins.2010.10.004

Honey, C. J., Sporns, O., Cammoun, L., Gigandet, X., Thiran, J. P., Meuli, R., & Hagmann, P. (2009). Predicting human resting-state functional connectivity from structural connectivity. *Proceedings of the National Academy of Sciences of the United States of America*, *106*(6), 2035–2040. https://doi.org/10.1073/pnas.0811168106

Huang, J., Liu, F., Tang, H., Wu, H., Li, L., Wu, R., Zhao, J., Wu, Y., Liu, Z., & Chen, J. (2017). Tranylcypromine Causes Neurotoxicity and Represses BHC110/LSD1 in Human-Induced Pluripotent Stem Cell-Derived Cerebral Organoids Model. *Frontiers in Neurology*, *8*. https://www.frontiersin.org/articles/10.3389/fneur.2017.00626

Hughes, C. S., Postovit, L. M., & Lajoie, G. A. (2010). Matrigel: A complex protein mixture required for optimal growth of cell culture. *PROTEOMICS*, *10*(9), 1886–1890. https://doi.org/10.1002/pmic.200900758

Humphries, M. d, Gurney, K., & Prescott, T. j. (2005). The brainstem reticular formation is a small-world, not scale-free, network. *Proceedings of the Royal Society B: Biological Sciences*, *273*(1585), 503–511. https://doi.org/10.1098/rspb.2005.3354

Iturria-Medina, Y., Sotero, R. C., Canales-Rodríguez, E. J., Alemán-Gómez, Y., & Melie-García, L. (2008). Studying the human brain anatomical network via diffusion-weighted MRI and Graph Theory. *NeuroImage*, *40*(3), 1064–1076. https://doi.org/10.1016/j.neuroimage.2007.10.060

Jaffe, R. J., Novakovic, V., & Peselow, E. D. (2013). Scopolamine as an antidepressant: A systematic review. *Clinical Neuropharmacology*, *36*(1), Article 1. https://doi.org/10.1097/WNF.0b013e318278b703

Jahanshad, N., Prasad, G., Toga, A. W., McMahon, K. L., de Zubicaray, G. I., Martin, N. G., Wright, M. J., & Thompson, P. M. (2012). Genetics of Path Lengths in Brain Connectivity Networks: HARDI-Based Maps in 457 Adults. *Multimodal Brain Image Analysis : Second International Workshop, MBIA 2012, Held in Conjunction with MICCAI 2012, Nice, France, October 1-5, 2012 : Proceedings / Pew-Thian Yap ... [et al.], (Eds.). MBIA (Workshop) (2nd : 2012 : Nice, Fr.*, *7509*, 29–40. https://doi.org/10.1007/978-3-642-33530-3_3

Jakab, A., Molnár, P. P., Bogner, P., Béres, M., & Berényi, E. L. (2012). Connectivity-based parcellation reveals interhemispheric differences in the insula. *Brain Topography*, *25*(3), 264–271. https://doi.org/10.1007/s10548-011-0205-y

Jarrell, T. A., Wang, Y., Bloniarz, A. E., Brittin, C. A., Xu, M., Thomson, J. N., Albertson, D. G., Hall, D. H., & Emmons, S. W. (2012). The connectome of a decision-making neural network. *Science (New York, N.Y.)*, *337*(6093), 437–444. https://doi.org/10.1126/science.1221762

Jin, C., Gao, C., Chen, C., Ma, S., Netra, R., Wang, Y., Zhang, M., & Li, D. (2011). A preliminary study of the dysregulation of the resting networks in first-episode medication-naive adolescent depression. *Neuroscience Letters*, *503*(2), 105–109. https://doi.org/10.1016/j.neulet.2011.08.017

Kaiser, R. H., Andrews-Hanna, J. R., Wager, T. D., & Pizzagalli, D. A. (2015). Large-Scale Network Dysfunction in Major Depressive Disorder: A Meta-analysis of Resting-State Functional Connectivity. *JAMA Psychiatry*, *72*(6), 603–611. https://doi.org/10.1001/jamapsychiatry.2015.0071

Kang, H. J., Voleti, B., Hajszan, T., Rajkowska, G., Stockmeier, C. A., Licznerski, P., Lepack, A., Majik, M. S., Jeong, L. S., Banasr, M., Son, H., & Duman, R. S. (2012). Decreased expression of synapse-related genes and loss of synapses in major depressive disorder. *Nature Medicine*, *18*(9), Article 9. https://doi.org/10.1038/nm.2886

Kaufman, J., Plotsky, P. M., Nemeroff, C. B., & Charney, D. S. (2000). Effects of early adverse experiences on brain structure and function: Clinical implications. *Biological Psychiatry*, *48*(8), 778–790. https://doi.org/10.1016/S0006-3223(00)00998-7

Keller, A. S., Ball, T. M., & Williams, L. M. (2020). Deep phenotyping of attention impairments and the 'Inattention Biotype' in Major Depressive Disorder. *Psychological Medicine*, *50*(13), 2203–2212. https://doi.org/10.1017/S0033291719002290

Kendler, K. S., Gardner, C. O., Neale, M. C., & Prescott, C. A. (2001). Genetic risk factors for major depression in men and women: Similar or different heritabilities and same or partly distinct genes? *Psychological Medicine*, *31*(4), 605–616. https://doi.org/10.1017/s0033291701003907

Kendler, K. S., Gardner, C. O., & Prescott, C. A. (2006). Toward a comprehensive developmental model for major depression in men. *The American Journal of Psychiatry*, *163*(1), 115–124. https://doi.org/10.1176/appi.ajp.163.1.115

Kennedy, S. H., & Emsley, R. (2006). Placebo-controlled trial of agomelatine in the treatment of major depressive disorder. *European Neuropsychopharmacology*, *16*(2), 93–100. https://doi.org/10.1016/j.euroneuro.2005.09.002

Kennedy, S. H., & Giacobbe, P. (2007). Treatment Resistant Depression—Advances in Somatic Therapies. *Annals of Clinical Psychiatry*, *19*(4), 279–287. https://doi.org/10.1080/10401230701675222

Kessler, R. C., Berglund, P., Demler, O., Jin, R., Merikangas, K. R., & Walters, E. E. (2005). Lifetime prevalence and age-of-onset distributions of DSM-IV disorders in the national comorbidity survey replication. *Archives of General Psychiatry*, *62*(6), Article 6. https://doi.org/10.1001/archpsyc.62.6.593

Kim, K., Doi, A., Wen, B., Ng, K., Zhao, R., Cahan, P., Kim, J., Aryee, M. J., Ji, H., Ehrlich, L. I. R., Yabuuchi, A., Takeuchi, A., Cunniff, K. C., Hongguang, H., Mckinney-Freeman, S., Naveiras, O., Yoon, T. J., Irizarry, R. A., Jung, N., … Daley, G. Q. (2010). Epigenetic memory in induced pluripotent stem cells. *Nature*, *467*(7313), Article 7313. https://doi.org/10.1038/nature09342

Kim, M.-H., & von Gersdorff, H. (2010). Extending the realm of membrane capacitance measurements to nerve terminals with complex morphologies. *The Journal of Physiology*, *588*(Pt 12), 2011–2012. https://doi.org/10.1113/jphysiol.2010.191270

Kim, S.-G., & Ogawa, S. (2012). Biophysical and Physiological Origins of Blood Oxygenation Level-Dependent fMRI Signals. *Journal of Cerebral Blood Flow & Metabolism*, *32*(7), 1188–1206. https://doi.org/10.1038/jcbfm.2012.23

Kim, S.-Y., & Lim, W. (2015). Effect of small-world connectivity on fast sparsely synchronized cortical rhythms. *Physica A: Statistical Mechanics and Its Applications*, *421*, 109–123. https://doi.org/10.1016/j.physa.2014.10.019

Kircanski, K., & Gotlib, I. H. (2015). Processing of Emotional Information in Major Depressive Disorder: Toward a Dimensional Understanding. *Emotion Review*, *7*(3), 256–264. https://doi.org/10.1177/1754073915575402

Kitsak, M., Gallos, L. K., Havlin, S., Liljeros, F., Muchnik, L., Stanley, H. E., & Makse, H. A. (2010). Identification of influential spreaders in complex networks. *Nature Physics*, *6*(11), Article 11. https://doi.org/10.1038/nphys1746

Klein Gunnewiek, T. M., Van Hugte, E. J. H., Frega, M., Guardia, G. S., Foreman, K., Panneman, D., Mossink, B., Linda, K., Keller, J. M., Schubert, D., Cassiman, D., Rodenburg, R., Vidal Folch, N., Oglesbee, D., Perales-Clemente, E., Nelson, T. J., Morava, E., Nadif Kasri, N., & Kozicz, T. (2020). M.3243A > G-Induced Mitochondrial Dysfunction Impairs Human Neuronal Development and Reduces Neuronal Network Activity and Synchronicity. *Cell Reports*, *31*(3), 107538. https://doi.org/10.1016/j.celrep.2020.107538

Krienen, F. M., Yeo, B. T. T., Ge, T., Buckner, R. L., & Sherwood, C. C. (2016). Transcriptional profiles of supragranular-enriched genes associate with corticocortical network architecture in the human brain. *Proceedings of the National Academy of Sciences*, *113*(4), E469–E478. https://doi.org/10.1073/pnas.1510903113

Krohne, H., Egloff, B., Kohlmann, C.-W., & Tausch, A. (1996). Untersuchungen mit einer deutschen Version der "Positive and Negative Affect Schedule" (PANAS). *Diagnostica*, *42*, 139–156. https://doi.org/10.1037/t49650-000

Kuffner, K., Triebelhorn, J., Meindl, K., Benner, C., Manook, A., Sudria-Lopez, D., Siebert, R., Nothdurfter, C., Baghai, T. C., Drexler, K., Berneburg, M., Rupprecht, R., Milenkovic, V. M., & Wetzel, C. H. (2020). Major Depressive Disorder is Associated with Impaired Mitochondrial Function in Skin Fibroblasts. *Cells*, *9*(4), 884. https://doi.org/10.3390/cells9040884

Lake, E. M. R., Ge, X., Shen, X., Herman, P., Hyder, F., Cardin, J. A., Higley, M. J., Scheinost, D., Papademetris, X., Crair, M. C., & Constable, R. T. (2020). Simultaneous cortex-wide fluorescence Ca2+ imaging and whole-brain fMRI. *Nature Methods*, *17*(12), Article 12. https://doi.org/10.1038/s41592-020-00984-6

Latora, V., & Marchiori, M. (2001). Efficient Behavior of Small-World Networks. *Physical Review Letters*, *87*(19), 198701. https://doi.org/10.1103/PhysRevLett.87.198701

Lawrie, S. M., Whalley, H. C., Abukmeil, S. S., Kestelman, J. N., Donnelly, L., Miller, P., Best, J. J. K., Owens, D. G. C., & Johnstone, E. C. (2001). Brain structure, genetic liability, and psychotic symptoms in subjects at high risk of developing schizophrenia. *Biological Psychiatry*, *49*(10), 811–823. https://doi.org/10.1016/S0006-3223(00)01117-3

Lee, S. P., Sung, I. K., Kim, J. H., Lee, S. Y., Park, H. S., & Shim, C. S. (2015). The effect of emotional stress and depression on the prevalence of digestive diseases. *Journal of Neurogastroenterology and Motility*, *21*(2), Article 2. https://doi.org/10.5056/jnm14116

Lemke, G. (2001). Glial Control of Neuronal Development. *Annual Review of Neuroscience*, *24*, 87–105. https://doi.org/10.1146/annurev.neuro.24.1.87

Lewinsohn, P. M., Clarke, G. N., Seeley, J. R., & Rohde, P. (1994). Major Depression in Community Adolescents: Age at Onset, Episode Duration, and Time to Recurrence. *Journal of the American Academy of Child and Adolescent Psychiatry*, *33*(6), Article 6. https://doi.org/10.1097/00004583-199407000-00006

Li, W., Ward, B. D., Liu, X., Chen, G., Jones, J. L., Antuono, P. G., Li, S.-J., & Goveas, J. S. (2015). Disrupted small world topology and modular organisation of functional networks in late-life depression with and without amnestic mild cognitive impairment. *Journal of Neurology, Neurosurgery & Psychiatry*, *86*(10), 1097–1105. https://doi.org/10.1136/jnnp-2014-309180

Li, X.-H., Song, Q., Chen, T., & Zhuo, M. (2017). Characterization of postsynaptic calcium signals in the pyramidal neurons of anterior cingulate cortex. *Molecular Pain*, *13*, 1744806917719847. https://doi.org/10.1177/1744806917719847

Liang, X., Wang, J., Yan, C., Shu, N., Xu, K., Gong, G., & He, Y. (2012). Effects of Different Correlation Metrics and Preprocessing Factors on Small-World Brain Functional Networks: A Resting-State Functional MRI Study. *PLOS ONE*, *7*(3), e32766. https://doi.org/10.1371/journal.pone.0032766

Lindau, M., & Neher, E. (1988). Patch-clamp techniques for time-resolved capacitance measurements in single cells. *Pflügers Archiv*, *411*(2), 137–146. https://doi.org/10.1007/BF00582306

Litwin-Kumar, A., & Doiron, B. (2012). Slow dynamics and high variability in balanced cortical networks with clustered connections. *Nature Neuroscience*, *15*(11), Article 11. https://doi.org/10.1038/nn.3220

Logothetis, N. K., Pauls, J., Augath, M., Trinath, T., & Oeltermann, A. (2001). Neurophysiological investigation of the basis of the fMRI signal. *Nature*, *412*(6843), Article 6843. https://doi.org/10.1038/35084005

Lord, A., Horn, D., Breakspear, M., & Walter, M. (2012). Changes in Community Structure of Resting State Functional Connectivity in Unipolar Depression. *PLoS ONE*, *7*(8), e41282. https://doi.org/10.1371/journal.pone.0041282

Luppino, F. S., de Wit, L. M., Bouvy, P. F., Stijnen, T., Cuijpers, P., Penninx, B. W. J. H., & Zitman, F. G. (2010). Overweight, Obesity, and Depression: A Systematic Review and Meta-analysis of Longitudinal Studies. *Archives of General Psychiatry*, *67*(3), 220–229. https://doi.org/10.1001/archgenpsychiatry.2010.2

Lydon-Staley, D. M., & Bassett, D. S. (2018). Network Neuroscience: A Framework for Developing Biomarkers in Psychiatry. In J. Pratt & J. Hall (Eds.), *Biomarkers in Psychiatry* (Vol. 40, pp. 79–109). Springer International Publishing. https://doi.org/10.1007/7854_2018_41

Lynall, M.-E., Bassett, D. S., Kerwin, R., McKenna, P. J., Kitzbichler, M., Muller, U., & Bullmore, E. (2010). Functional Connectivity and Brain Networks in Schizophrenia. *Journal of Neuroscience*, *30*(28), 9477–9487. https://doi.org/10.1523/JNEUROSCI.0333-10.2010

Ma, D. K., Ming, G., & Song, H. (2005). Glial influences on neural stem cell development: Cellular niches for adult neurogenesis. *Current Opinion in Neurobiology*, *15*(5), 514–520. https://doi.org/10.1016/j.conb.2005.08.003

Ma, W., Tavakoli, T., Derby, E., Serebryakova, Y., Rao, M. S., & Mattson, M. P. (2008). Cell-extracellular matrix interactions regulate neural differentiation of human embryonic stem cells. *BMC Developmental Biology*, *8*(1), 90. https://doi.org/10.1186/1471-213X-8-90

Ma, Z., Zhang, Q., Tu, W., & Zhang, N. (2022). Gaining insight into the neural basis of resting-state fMRI signal. *NeuroImage*, *250*, 118960. https://doi.org/10.1016/j.neuroimage.2022.118960

Mazia, D., Schatten, G., & Sale, W. (1975). Adhesion of cells to surfaces coated with polylysine. Applications to electron microscopy. *The Journal of Cell Biology*, *66*(1), 198–200. https://doi.org/10.1083/jcb.66.1.198

McCarthy, M. J., Liang, S., Spadoni, A. D., Kelsoe, J. R., & Simmons, A. N. (2014). Whole Brain Expression of Bipolar Disorder Associated Genes: Structural and Genetic Analyses. *PLOS ONE*, *9*(6), e100204. https://doi.org/10.1371/journal.pone.0100204

McCulloch, W. S., & Pitts, W. A. (1943). A logical calculus of the ideas immanent in nervous activity. *Bull. Math. Biophys*, *5*, 115–133.

McQuin, C., Goodman, A., Chernyshev, V., Kamentsky, L., Cimini, B. A., Karhohs, K. W., Doan, M., Ding, L., Rafelski, S. M., Thirstrup, D., Wiegraebe, W., Singh, S., Becker, T., Caicedo, J. C., & Carpenter, A. E. (2018). CellProfiler 3.0: Next-generation image processing for biology. *PLOS Biology*, *16*(7), e2005970. https://doi.org/10.1371/journal.pbio.2005970

Mello, M. F. D., Mari, J. D. J., Bacaltchuk, J., Verdeli, H., & Neugebauer, R. (2005). A systematic review of research findings on the efficacy of interpersonal therapy for depressive disorders. *European Archives of Psychiatry and Clinical Neuroscience*, *255*(2), Article 2. https://doi.org/10.1007/s00406-004-0542-x

Meng, C., Brandl, F., Tahmasian, M., Shao, J., Manoliu, A., Scherr, M., Schwerthöffer, D., Bäuml, J., Förstl, H., Zimmer, C., Wohlschläger, A. M., Riedl, V., & Sorg, C. (2014). Aberrant topology of striatum's connectivity is

associated with the number of episodes in depression. *Brain*, *137*(2), 598–609. https://doi.org/10.1093/brain/awt290

Menon, V., Cerri, D., Lee, B., Yuan, R., Lee, S.-H., & Shih, Y.-Y. I. (2023). Optogenetic stimulation of anterior insular cortex neurons in male rats reveals causal mechanisms underlying suppression of the default mode network by the salience network. *Nature Communications*, *14*(1), Article 1. https://doi.org/10.1038/s41467-023-36616-8

Meunier, D., Lambiotte, R., & Bullmore, E. (2010). Modular and Hierarchically Modular Organization of Brain Networks. *Frontiers in Neuroscience*, *4*. https://www.frontiersin.org/articles/10.3389/fnins.2010.00200

Milgram. (1967). The small world problem. *Psychology Today*, *2*(1), 60–67.

Mišić, B., Betzel, R. F., de Reus, M. A., van den Heuvel, M. P., Berman, M. G., McIntosh, A. R., & Sporns, O. (2016). Network-Level Structure-Function Relationships in Human Neocortex. *Cerebral Cortex*, *26*(7), 3285–3296. https://doi.org/10.1093/cercor/bhw089

Molnar-Szakacs, I., & Uddin, L. Q. (2022). Anterior insula as a gatekeeper of executive control. *Neuroscience & Biobehavioral Reviews*, *139*, 104736. https://doi.org/10.1016/j.neubiorev.2022.104736

Mutschler, I., Wieckhorst, B., Kowalevski, S., Derix, J., Wentlandt, J., Schulze-Bonhage, A., & Ball, T. (2009). Functional organization of the human anterior insular cortex. *Neuroscience Letters*, *457*(2), 66–70. https://doi.org/10.1016/j.neulet.2009.03.101

Neher, E., & Sakaba, T. (2008). Multiple Roles of Calcium Ions in the Regulation of Neurotransmitter Release. *Neuron*, *59*(6), 861–872. https://doi.org/10.1016/j.neuron.2008.08.019

Nelson, C. J., & Bonner, S. (2021). Neuronal Graphs: A Graph Theory Primer for Microscopic, Functional Networks of Neurons Recorded by Calcium Imaging. *Frontiers in Neural Circuits*, *15*, 662882. https://doi.org/10.3389/fncir.2021.662882

Nestler, E. J., Barrot, M., DiLeone, R. J., Eisch, A. J., Gold, S. J., & Monteggia, L. M. (2002). Neurobiology of Depression. *Neuron*, *34*(1), 13–25. https://doi.org/10.1016/S0896-6273(02)00653-0

Nestler, E. J., & Hyman, S. E. (2010). Animal models of neuropsychiatric disorders. *Nature Neuroscience*, *13*(10), Article 10. https://doi.org/10.1038/nn.2647

Newman, M. E. J. (2004). Fast algorithm for detecting community structure in networks. *Physical Review E*, *69*(6), 066133. https://doi.org/10.1103/PhysRevE.69.066133

Nichols, T. E. (2012). Multiple testing corrections, nonparametric methods, and random field theory. *NeuroImage*, *62*(2), 811–815. https://doi.org/10.1016/j.neuroimage.2012.04.014

Niven, J. E., & Laughlin, S. B. (2008). Energy limitation as a selective pressure on the evolution of sensory systems. *Journal of Experimental Biology*, *211*(11), 1792–1804. https://doi.org/10.1242/jeb.017574

Ohi, Y., Qin, H., Hong, C., Blouin, L., Polo, J. M., Guo, T., Qi, Z., Downey, S. L., Manos, P. D., Rossi, D. J., Yu, J., Hebrok, M., Hochedlinger, K., Costello, J. F., Song, J. S., & Ramalho-Santos, M. (2011). Incomplete DNA methylation underlies a transcriptional memory of somatic cells in human iPS cells. *Nature Cell Biology*, *13*(5), Article 5. https://doi.org/10.1038/ncb2239

Okita, K., Matsumura, Y., Sato, Y., Okada, A., Morizane, A., Okamoto, S., Hong, H., Nakagawa, M., Tanabe, K., Tezuka, K., Shibata, T., Kunisada, T., Takahashi, M., Takahashi, J., Saji, H., & Yamanaka, S. (2011). A more efficient method to generate integration-free human iPS cells. *Nature Methods*, *8*(5), 409–412. https://doi.org/10.1038/nmeth.1591

O'Reilly, J. X., Croxson, P. L., Jbabdi, S., Sallet, J., Noonan, M. P., Mars, R. B., Browning, P. G. F., Wilson, C. R. E., Mitchell, A. S., Miller, K. L., Rushworth, M. F. S., & Baxter, M. G. (2013). Causal effect of disconnection lesions on interhemispheric functional connectivity in rhesus monkeys. *Proceedings of the National Academy of Sciences*, *110*(34), 13982–13987. https://doi.org/10.1073/pnas.1305062110

Otte, C., Gold, S. M., Penninx, B. W., Pariante, C. M., Etkin, A., Fava, M., Mohr, D. C., & Schatzberg, A. F. (2016). Major depressive disorder. *Nature Reviews Disease Primers*, *2*(1), 16065. https://doi.org/10.1038/nrdp.2016.65

Papouin, T., Dunphy, J., Tolman, M., Foley, J. C., & Haydon, P. G. (2017). Astrocytic control of synaptic function. *Philosophical Transactions of the Royal Society B: Biological Sciences*, *372*(1715), 20160154. https://doi.org/10.1098/rstb.2016.0154

Park, B., Seo, J., Yi, J., & Park, H. (2015). Structural and Functional Brain Connectivity of People with Obesity and Prediction of Body Mass Index Using Connectivity. *PLOS ONE*, *10*(11), e0141376. https://doi.org/10.1371/journal.pone.0141376

Park, C., Kim, S. Y., Kim, Y.-H., & Kim, K. (2008). Comparison of the small-world topology between anatomical and functional connectivity in the human brain. *Physica A: Statistical Mechanics and Its Applications*, *387*(23), 5958–5962. https://doi.org/10.1016/j.physa.2008.06.048

Park, H.-J., & Friston, K. (2013). Structural and functional brain networks: From connections to cognition. *Science (New York, N.Y.)*, *342*(6158), 1238411. https://doi.org/10.1126/science.1238411

Pauling, L., & Coryell, C. D. (1936). The Magnetic Properties and Structure of Hemoglobin, Oxyhemoglobin and Carbonmonoxyhemoglobin. *Proceedings of the National Academy of Sciences*, *22*(4), 210–216. https://doi.org/10.1073/pnas.22.4.210

Pei, S., Liu, L., Zhong, Z., Wang, H., Lin, S., & Shang, J. (2016). Risk of prenatal depression and stress treatment: Alteration on serotonin system of offspring through exposure to Fluoxetine. *Scientific Reports*, *6*(1), Article 1. https://doi.org/10.1038/srep33822

Penn, E., & Tracy, D. K. (2012). The drugs don't work? Antidepressants and the current and future pharmacological management of depression. *Therapeutic Advances in Psychopharmacology*, *2*(5), 179–188. https://doi.org/10.1177/2045125312445469

Perin, R., Berger, T. K., & Markram, H. (2011). A synaptic organizing principle for cortical neuronal groups. *Proceedings of the National Academy of Sciences*, *108*(13), 5419–5424. https://doi.org/10.1073/pnas.1016051108

Pernice, V., Staude, B., Cardanobile, S., & Rotter, S. (2011). How Structure Determines Correlations in Neuronal Networks. *PLOS Computational Biology*, *7*(5), e1002059. https://doi.org/10.1371/journal.pcbi.1002059

Pfrieger, F. W., & Barres, B. A. (1997). Synaptic Efficacy Enhanced by Glial Cells in Vitro. *Science*, *277*(5332), 1684–1687. https://doi.org/10.1126/science.277.5332.1684

Phan, K. L., Wager, T., Taylor, S. F., & Liberzon, I. (2002). Functional Neuroanatomy of Emotion: A Meta-Analysis of Emotion Activation Studies in PET and fMRI. *NeuroImage*, *16*(2), 331–348. https://doi.org/10.1006/nimg.2002.1087

Pnevmatikakis, E. A. (2019). Analysis pipelines for calcium imaging data. *Current Opinion in Neurobiology*, *55*, 15–21. https://doi.org/10.1016/j.conb.2018.11.004

Pnevmatikakis, E. A., & Giovannucci, A. (2017). NoRMCorre: An online algorithm for piecewise rigid motion correction of calcium imaging data. *Journal of Neuroscience Methods*, *291*, 83–94. https://doi.org/10.1016/j.jneumeth.2017.07.031

Poli, D., Pastore, V. P., & Massobrio, P. (2015). Functional connectivity in in vitro neuronal assemblies. *Frontiers in Neural Circuits*, *9*, 163767. https://doi.org/10.3389/fncir.2015.00057

Price, J. L., & Drevets, W. C. (2012). Neural circuits underlying the pathophysiology of mood disorders. *Trends in Cognitive Sciences*, *16*(1), Article 1. https://doi.org/10.1016/j.tics.2011.12.011

Price, R. B., Lane, S., Gates, K., Kraynak, T. E., Horner, M. S., Thase, M. E., & Siegle, G. J. (2017). Parsing Heterogeneity in the Brain Connectivity of Depressed and Healthy Adults During Positive Mood. *Biological Psychiatry*, *81*(4), 347–357. https://doi.org/10.1016/j.biopsych.2016.06.023

Puppo, F., George, V., & Silva, G. A. (2018). An Optimized Structure-Function Design Principle Underlies Efficient Signaling Dynamics in Neurons. *Scientific Reports*, *8*(1), Article 1. https://doi.org/10.1038/s41598-018-28527-2

Raichle, M. E., MacLeod, A. M., Snyder, A. Z., Powers, W. J., Gusnard, D. A., & Shulman, G. L. (2001). A default mode of brain function. *Proceedings of the National Academy of Sciences*, *98*(2), 676–682. https://doi.org/10.1073/pnas.98.2.676

Ramon y Cajal, S. (1995). *Histology of the Nervous System of Man and Vertebrates*. Oxford Univ. Press.

Ramón y Cajal, S. R. (1888). Estructura de los centros nerviosos de las aves. *Rev. Trim. Histol. Norm. Pat*, *1*, 1–10.

Reimann, M. W., Nolte, M., Scolamiero, M., Turner, K., Perin, R., Chindemi, G., Dłotko, P., Levi, R., Hess, K., & Markram, H. (2017). Cliques of Neurons Bound into Cavities Provide a Missing Link between Structure and Function. *Frontiers in Computational Neuroscience*, *11*. https://www.frontiersin.org/articles/10.3389/fncom.2017.00048

Reineberg, A. E., Hatoum, A. S., Hewitt, J. K., Banich, M. T., & Friedman, N. P. (2020). Genetic and Environmental Influence on the Human Functional Connectome. *Cerebral Cortex*, *30*(4), 2099–2113. https://doi.org/10.1093/cercor/bhz225

Rezin, G. T., Amboni, G., Zugno, A. I., Quevedo, J., & Streck, E. L. (2008). Mitochondrial Dysfunction and Psychiatric Disorders. *Neurochemical Research*, *34*(6), 1021. https://doi.org/10.1007/s11064-008-9865-8

Rial, D., Lemos, C., Pinheiro, H., Duarte, J. M., Gonçalves, F. Q., Real, J. I., Prediger, R. D., Gonçalves, N., Gomes, C. A., Canas, P. M., Agostinho, P., & Cunha, R. A. (2016). Depression as a Glial-Based Synaptic Dysfunction. *Frontiers in Cellular Neuroscience*, *9*. https://www.frontiersin.org/articles/10.3389/fncel.2015.00521

Rivera-Alba, M., Vitaladevuni, S. N., Mishchenko, Y., Lu, Z., Takemura, S.-Y., Scheffer, L., Meinertzhagen, I. A., Chklovskii, D. B., & de Polavieja, G. G. (2011). Wiring economy and volume exclusion determine neuronal placement in the Drosophila brain. *Current Biology: CB*, *21*(23), 2000–2005. https://doi.org/10.1016/j.cub.2011.10.022

Robinson, O. J., Cools, R., Carlisi, C. O., Sahakian, B. J., & Drevets, W. C. (2012). Ventral Striatum Response During Reward and Punishment Reversal Learning in Unmedicated Major Depressive Disorder. *American Journal of Psychiatry*, *169*(2), 152–159. https://doi.org/10.1176/appi.ajp.2011.11010137

Robinson, P. A., Henderson, J. A., Matar, E., Riley, P., & Gray, R. T. (2009). Dynamical Reconnection and Stability Constraints on Cortical Network Architecture. *Physical Review Letters*, *103*(10), 108104. https://doi.org/10.1103/PhysRevLett.103.108104

Romme, I. A. C., de Reus, M. A., Ophoff, R. A., Kahn, R. S., & van den Heuvel, M. P. (2017). Connectome Disconnectivity and Cortical Gene Expression in Patients With Schizophrenia. *Biological Psychiatry*, *81*(6), 495–502. https://doi.org/10.1016/j.biopsych.2016.07.012

Rubinov, M., & Sporns, O. (2010). Complex network measures of brain connectivity: Uses and interpretations. *NeuroImage*, *52*(3), 1059–1069. https://doi.org/10.1016/j.neuroimage.2009.10.003

Rubinov, M., Sporns, O., van Leeuwen, C., & Breakspear, M. (2009). Symbiotic relationship between brain structure and dynamics. *BMC Neuroscience*, *10*(1), 55. https://doi.org/10.1186/1471-2202-10-55

Ruhé, H., van Rooijen, G., Spijker, J., Peeters, F., & Schene, A. (2011). Staging methods for treatment resistant depression. A systematic review. *Journal of Affective Disorders*, *137*, 35–45. https://doi.org/10.1016/j.jad.2011.02.020

Santos-Sierra, D. de, Sendiña-Nadal, I., Leyva, I., Almendral, J. A., Anava, S., Ayali, A., Papo, D., & Boccaletti, S. (2014). Emergence of Small-World Anatomical Networks in Self-Organizing Clustered Neuronal Cultures. *PLOS ONE*, *9*(1), e85828. https://doi.org/10.1371/journal.pone.0085828

Saveanu, R. V., & Nemeroff, C. B. (2012). Etiology of Depression: Genetic and Environmental Factors. *Psychiatric Clinics of North America*, *35*(1), 51–71. https://doi.org/10.1016/j.psc.2011.12.001

Schildkraut, J. J. (1965). The catecholamine hypothesis of affective disorders: A review of supporting evidence. *The American Journal of Psychiatry*, *122*(5), Article 5. https://doi.org/10.1176/ajp.122.5.509

Schneider, C. A., Rasband, W. S., & Eliceiri, K. W. (2012). NIH Image to ImageJ: 25 years of image analysis. *Nature Methods*, *9*(7), Article 7. https://doi.org/10.1038/nmeth.2089

Scholtens, L. H., Pijnenburg, R., de Lange, S. C., Huitinga, I., van den Heuvel, M. P., & Netherlands Brain Bank. (2022). Common Microscale and Macroscale Principles of Connectivity in the Human Brain. *The Journal of Neuroscience*, *42*(20), 4147–4163. https://doi.org/10.1523/JNEUROSCI.1572-21.2022

Schroeter, M. S., Charlesworth, P., Kitzbichler, M. G., Paulsen, O., & Bullmore, E. T. (2015). Emergence of Rich-Club Topology and Coordinated Dynamics in Development of Hippocampal Functional Networks In Vitro. *Journal of Neuroscience*, *35*(14), 5459–5470. https://doi.org/10.1523/JNEUROSCI.4259-14.2015

Schröter, M., Paulsen, O., & Bullmore, E. T. (2017). Micro-connectomics: Probing the organization of neuronal networks at the cellular scale. *Nature Reviews Neuroscience*, *18*(3), 131–146. https://doi.org/10.1038/nrn.2016.182

Seeley, W. W., Crawford, R. K., Zhou, J., Miller, B. L., & Greicius, M. D. (2009). Neurodegenerative Diseases Target Large-Scale Human Brain Networks. *Neuron*, *62*(1), 42–52. https://doi.org/10.1016/j.neuron.2009.03.024

Shadrina, M., Bondarenko, E. A., & Slominsky, P. A. (2018). Genetics Factors in Major Depression Disease. *Frontiers in Psychiatry*, *9*. https://www.frontiersin.org/articles/10.3389/fpsyt.2018.00334

Shein-Idelson, M., Ben-Jacob, E., & Hanein, Y. (2011). Engineered Neuronal Circuits: A New Platform for Studying the Role of Modular Topology. *Frontiers in Neuroengineering*, *4*. https://www.frontiersin.org/articles/10.3389/fneng.2011.00010

Sheline, Y. I., Price, J. L., Yan, Z., & Mintun, M. A. (2010). Resting-state functional MRI in depression unmasks increased connectivity between networks via the dorsal nexus. *Proceedings of the National Academy of Sciences*, *107*(24), 11020–11025. https://doi.org/10.1073/pnas.1000446107

Shimono, M., & Beggs, J. M. (2015). Functional Clusters, Hubs, and Communities in the Cortical Microconnectome. *Cerebral Cortex*, *25*(10), 3743–3757. https://doi.org/10.1093/cercor/bhu252

Skudlarski, P., Jagannathan, K., Calhoun, V. D., Hampson, M., Skudlarska, B. A., & Pearlson, G. (2008). Measuring Brain Connectivity: Diffusion Tensor Imaging Validates Resting State Temporal Correlations. *NeuroImage*, *43*(3), 554–561. https://doi.org/10.1016/j.neuroimage.2008.07.063

Smit, D. J. A., Boersma, M., van Beijsterveldt, C. E. M., Posthuma, D., Boomsma, D. I., Stam, C. J., & de Geus, E. J. C. (2010). Endophenotypes in a Dynamically Connected Brain. *Behavior Genetics*, *40*(2), 167–177. https://doi.org/10.1007/s10519-009-9330-8

Smith, S. L., & Häusser, M. (2010). Parallel processing of visual space by neighboring neurons in mouse visual cortex. *Nature Neuroscience*, *13*(9), 1144–1149. https://doi.org/10.1038/nn.2620

Soliman, M. A., Aboharb, F., Zeltner, N., & Studer, L. (2017). Pluripotent stem cells in neuropsychiatric disorders. *Molecular Psychiatry*, *22*(9), Article 9. https://doi.org/10.1038/mp.2017.40

Sporns, O. (2011). The human connectome: A complex network: The human connectome. *Annals of the New York Academy of Sciences*, *1224*(1), 109–125. https://doi.org/10.1111/j.1749-6632.2010.05888.x

Sporns, O. (2016). Connectome Networks: From Cells to Systems. In H. Kennedy, D. C. Van Essen, & Y. Christen (Eds.), *Micro-, Meso- and Macro-Connectomics of the Brain*. Springer. http://www.ncbi.nlm.nih.gov/books/NBK435773/

Sporns, O., Honey, C. J., & Kötter, R. (2007). Identification and Classification of Hubs in Brain Networks. *PLOS ONE*, *2*(10), e1049. https://doi.org/10.1371/journal.pone.0001049

Sporns, O., Tononi, G., & Edelman, G. M. (2000). Theoretical Neuroanatomy: Relating Anatomical and Functional Connectivity in Graphs and Cortical Connection Matrices. *Cerebral Cortex*, *10*(2), 127–141. https://doi.org/10.1093/cercor/10.2.127

Sporns, O., & Zwi, J. (2004). The Small World of the Cerebral Cortex. *Neuroinformatics*, *2*, 145–162. https://doi.org/10.1385/NI:2:2:145

Stam, C. J., & Reijneveld, J. C. (2007). Graph theoretical analysis of complex networks in the brain. *Nonlinear Biomedical Physics*, *1*(1), 3. https://doi.org/10.1186/1753-4631-1-3

Stam, C. J., Van Straaten, E. C. W., Van Dellen, E., Tewarie, P., Gong, G., Hillebrand, A., Meier, J., & Van Mieghem, P. (2016). The relation between structural and functional connectivity patterns in complex brain networks. *International Journal of Psychophysiology*, *103*, 149–160. https://doi.org/10.1016/j.ijpsycho.2015.02.011

Stassen, H. H., & Angst, J. (1998). Delayed Onset of Action of Antidepressants. *CNS Drugs*, *9*(3), 177–184. https://doi.org/10.2165/00023210-199809030-00001

Stetter, O., Battaglia, D., Soriano, J., & Geisel, T. (2012). Model-Free Reconstruction of Excitatory Neuronal Connectivity from Calcium Imaging Signals. *PLOS Computational Biology*, *8*(8), e1002653. https://doi.org/10.1371/journal.pcbi.1002653

Stirling, D. R., Swain-Bowden, M. J., Lucas, A. M., Carpenter, A. E., Cimini, B. A., & Goodman, A. (2021). CellProfiler 4: Improvements in speed, utility and usability. *BMC Bioinformatics*, *22*(1), 433. https://doi.org/10.1186/s12859-021-04344-9

Sullivan, P. F., Neale, M. C., & Kendler, K. S. (2000). Genetic Epidemiology of Major Depression: Review and Meta-Analysis. *American Journal of Psychiatry*, *157*(10), 1552–1562. https://doi.org/10.1176/appi.ajp.157.10.1552

Szczepanski, S. M., Pinsk, M. A., Douglas, M. M., Kastner, S., & Saalmann, Y. B. (2013). Functional and structural architecture of the human dorsal frontoparietal attention network. *Proceedings of the National Academy of Sciences*, *110*(39), 15806–15811. https://doi.org/10.1073/pnas.1313903110

Takahashi, K., Tanabe, K., Ohnuki, M., Narita, M., Ichisaka, T., Tomoda, K., & Yamanaka, S. (2007). Induction of Pluripotent Stem Cells from Adult Human Fibroblasts by Defined Factors. *Cell*, *131*(5), 861–872. https://doi.org/10.1016/j.cell.2007.11.019

Teicher, M. H., Anderson, C. M., Ohashi, K., & Polcari, A. (2014). Childhood Maltreatment: Altered Network Centrality of Cingulate, Precuneus, Temporal Pole and Insula. *Biological Psychiatry*, *76*(4), 297–305. https://doi.org/10.1016/j.biopsych.2013.09.016

Teller, S., Granell, C., Domenico, M. D., Soriano, J., Gómez, S., & Arenas, A. (2014). Emergence of Assortative Mixing between Clusters of Cultured Neurons. *PLOS Computational Biology*, *10*(9), e1003796. https://doi.org/10.1371/journal.pcbi.1003796

Tesler, F., Linne, M.-L., & Destexhe, A. (2023). Modeling the relationship between neuronal activity and the BOLD signal: Contributions from astrocyte calcium dynamics. *Scientific Reports*, *13*(1), Article 1. https://doi.org/10.1038/s41598-023-32618-0

Tibau, E., Valencia, M., & Soriano, J. (2013). Identification of neuronal network properties from the spectral analysis of calcium imaging signals in neuronal cultures. *Frontiers in Neural Circuits*, *7*. https://www.frontiersin.org/articles/10.3389/fncir.2013.00199

Tobe, E. (2013). Mitochondrial dysfunction, oxidative stress, and major depressive disorder. *Neuropsychiatric Disease and Treatment*, 567. https://doi.org/10.2147/NDT.S44282

Tognoli, E., & Kelso, J. A. S. (2014). The Metastable Brain. *Neuron*, *81*(1), 35–48. https://doi.org/10.1016/j.neuron.2013.12.022

Towlson, E. K., Vértes, P. E., Ahnert, S. E., Schafer, W. R., & Bullmore, E. T. (2013). The Rich Club of the C. elegans Neuronal Connectome. *Journal of Neuroscience*, *33*(15), 6380–6387. https://doi.org/10.1523/JNEUROSCI.3784-12.2013

Trepl, J., Dahlmanns, M., Kornhuber, J., Groemer, T. W., & Dahlmanns, J. K. (2022). Common network effect-patterns after monoamine reuptake inhibition in dissociated hippocampus cultures. *Journal of Neural Transmission*, *129*(3), 261–275. https://doi.org/10.1007/s00702-022-02477-6

Triebelhorn, J., Cardon, I., Kuffner, K., Bader, S., Jahner, T., Meindl, K., Rothhammer-Hampl, T., Riemenschneider, M. J., Drexler, K., Berneburg, M., Nothdurfter, C., Manook, A., Brochhausen, C., Baghai, T. C., Hilbert, S., Rupprecht, R., Milenkovic, V. M., & Wetzel, C. H. (2022). Induced neural progenitor cells and iPS-neurons from major depressive disorder patients show altered bioenergetics and electrophysiological properties. *Molecular Psychiatry*. https://doi.org/10.1038/s41380-022-01660-1

Uddin, L. Q., Nomi, J. S., Hebert-Seropian, B., Ghaziri, J., & Boucher, O. (2017). Structure and function of the human insula. *Journal of Clinical Neurophysiology : Official Publication of the American Electroencephalographic Society*, *34*(4), 300–306. https://doi.org/10.1097/WNP.0000000000000377

Vaarmann, A., Mandel, M., Zeb, A., Wareski, P., Liiv, J., Kuum, M., Antsov, E., Liiv, M., Cagalinec, M., Choubey, V., & Kaasik, A. (2016). Mitochondrial biogenesis is required for axonal growth. *Development*, *143*(11), 1981–1992. https://doi.org/10.1242/dev.128926

Vadodaria, K. C., Ji, Y., Skime, M., Paquola, A. C., Nelson, T., Hall-Flavin, D., Heard, K. J., Fredlender, C., Deng, Y., Elkins, J., Dani, K., Le, A. T., Marchetto, M. C., Weinshilboum, R., & Gage, F. H. (2019). Altered serotonergic circuitry in SSRI-resistant major depressive disorder patient-derived neurons. *Molecular Psychiatry*, *24*(6), Article 6. https://doi.org/10.1038/s41380-019-0377-5

Vadodaria, K. C., Ji, Y., Skime, M., Paquola, A., Nelson, T., Hall-Flavin, D., Fredlender, C., Heard, K. J., Deng, Y., Le, A. T., Dave, S., Fung, L., Li, X., Marchetto, M. C., Weinshilboum, R., & Gage, F. H. (2019). Serotonin-induced hyperactivity in SSRI-resistant major depressive disorder patient-derived neurons. *Molecular Psychiatry*, *24*(6), Article 6. https://doi.org/10.1038/s41380-019-0363-y

Vadodaria, K. C., Mertens, J., Paquola, A., Bardy, C., Li, X., Jappelli, R., Fung, L., Marchetto, M. C., Hamm, M., Gorris, M., Koch, P., & Gage, F. H. (2016). Generation of functional human serotonergic neurons from fibroblasts. *Molecular Psychiatry*, *21*(1), Article 1. https://doi.org/10.1038/mp.2015.161

van den Heuvel, M. P., Bullmore, E. T., & Sporns, O. (2016). Comparative Connectomics. *Trends in Cognitive Sciences*, *20*(5), 345–361. https://doi.org/10.1016/j.tics.2016.03.001

van den Heuvel, M. P., Kahn, R. S., Goñi, J., & Sporns, O. (2012). High-cost, high-capacity backbone for global brain communication. *Proceedings of the National Academy of Sciences*, *109*(28), 11372–11377. https://doi.org/10.1073/pnas.1203593109

van den Heuvel, M. P., Scholtens, L. H., & Kahn, R. S. (2019). Multiscale Neuroscience of Psychiatric Disorders. *Biological Psychiatry*, *86*(7), 512–522. https://doi.org/10.1016/j.biopsych.2019.05.015

Van Den Heuvel, M. P., & Sporns, O. (2011). Rich-Club Organization of the Human Connectome. *The Journal of Neuroscience*, *31*(44), 15775–15786. https://doi.org/10.1523/JNEUROSCI.3539-11.2011

Van Den Heuvel, M. P., & Sporns, O. (2013). An Anatomical Substrate for Integration among Functional Networks in Human Cortex. *The Journal of Neuroscience*, *33*(36), 14489–14500. https://doi.org/10.1523/JNEUROSCI.2128-13.2013

van den Heuvel, M. P., & Sporns, O. (2019). A cross-disorder connectome landscape of brain dysconnectivity. *Nature Reviews Neuroscience*, *20*(7), Article 7. https://doi.org/10.1038/s41583-019-0177-6

van den Heuvel, M. P., van Soelen, I. L. C., Stam, C. J., Kahn, R. S., Boomsma, D. I., & Hulshoff Pol, H. E. (2013). Genetic control of functional brain network efficiency in children. *European Neuropsychopharmacology*, *23*(1), 19–23. https://doi.org/10.1016/j.euroneuro.2012.06.007

van den Heuvel, M. P., & Yeo, B. T. T. (2017). A Spotlight on Bridging Microscale and Macroscale Human Brain Architecture. *Neuron*, *93*(6), 1248–1251. https://doi.org/10.1016/j.neuron.2017.02.048

Versace, A., Thompson, W. K., Zhou, D., Almeida, J. R. C., Hassel, S., Klein, C. R., Kupfer, D. J., & Phillips, M. L. (2010). Abnormal Left and Right Amygdala-Orbitofrontal Cortical Functional Connectivity to Emotional Faces: State Versus Trait Vulnerability Markers of Depression in Bipolar Disorder. *Biological Psychiatry*, *67*(5), 422–431. https://doi.org/10.1016/j.biopsych.2009.11.025

Vértes, P. E., Alexander-Bloch, A. F., Gogtay, N., Giedd, J. N., Rapoport, J. L., & Bullmore, E. T. (2012). Simple models of human brain functional networks. *Proceedings of the National Academy of Sciences*, *109*(15), 5868–5873. https://doi.org/10.1073/pnas.1111738109

Vértes, P. E., & Bullmore, E. T. (2015). Annual Research Review: Growth connectomics – the organization and reorganization of brain networks during normal and abnormal development. *Journal of Child Psychology and Psychiatry*, *56*(3), 299–320. https://doi.org/10.1111/jcpp.12365

Vierbuchen, T., Ostermeier, A., Pang, Z. P., Kokubu, Y., Südhof, T. C., & Wernig, M. (2010). Direct conversion of fibroblasts to functional neurons by defined factors. *Nature*, *463*(7284), Article 7284. https://doi.org/10.1038/nature08797

Vos, T., Lim, S. S., Abbafati, C., Abbas, K. M., Abbasi, M., Abbasifard, M., Abbasi-Kangevari, M., Abbastabar, H., Abd-Allah, F., Abdelalim, A., Abdollahi, M., Abdollahpour, I., Abolhassani, H., Aboyans, V., Abrams, E. M., Abreu, L. G., Abrigo, M. R. M., Abu-Raddad, L. J., Abushouk, A. I., … Murray, C. J. L. (2020). Global burden of 369 diseases and injuries in 204 countries and territories, 1990–2019: A systematic analysis for the Global Burden of Disease Study 2019. *The Lancet*, *396*(10258), 1204–1222. https://doi.org/10.1016/S0140-6736(20)30925-9

Wang. (2011). Sustained activity in hierarchical modular neural networks: Self-organized criticality and oscillations. *Frontiers in Computational Neuroscience*. https://doi.org/10.3389/fncom.2011.00030

Wang, J., Wang, L., Zang, Y., Yang, H., Tang, H., Gong, Q., Chen, Z., Zhu, C., & He, Y. (2009). Parcellation-dependent small-world brain functional networks: A resting-state fMRI study. *Human Brain Mapping*, *30*(5), 1511–1523. https://doi.org/10.1002/hbm.20623

Wang, L., Hermens, D. F., Hickie, I. B., & Lagopoulos, J. (2012). A systematic review of resting-state functional-MRI studies in major depression. *Journal of Affective Disorders*, *142*(1), 6–12. https://doi.org/10.1016/j.jad.2012.04.013

Wang, M., Zhang, L., & Gage, F. H. (2020). Modeling neuropsychiatric disorders using human induced pluripotent stem cells. *Protein & Cell*, *11*(1), 45–59. https://doi.org/10.1007/s13238-019-0638-8

Wang, Q., Jie, W., Liu, J.-H., Yang, J.-M., & Gao, T.-M. (2017). An astroglial basis of major depressive disorder? An overview. *Glia*, *65*(8), 1227–1250. https://doi.org/10.1002/glia.23143

Wang, Z., Dai, Z., Gong, G., Zhou, C., & He, Y. (2015). Understanding Structural-Functional Relationships in the Human Brain: A Large-Scale Network Perspective. *The Neuroscientist*, *21*(3), 290–305. https://doi.org/10.1177/1073858414537560

Warren, D. E., Power, J. D., Bruss, J., Denburg, N. L., Waldron, E. J., Sun, H., Petersen, S. E., & Tranel, D. (2014). Network measures predict neuropsychological outcome after brain injury. *Proceedings of the National Academy of Sciences*, *111*(39), 14247–14252. https://doi.org/10.1073/pnas.1322173111

Watson, D., Clark, L. A., & Tellegen, A. (1988). Development and validation of brief measures of positive and negative affect: The PANAS scales. *Journal of Personality and Social Psychology*, *54*(6), 1063–1070. https://doi.org/10.1037/0022-3514.54.6.1063

Watts, D. J., & Strogatz, S. H. (1998). Collective dynamics of 'small-world' networks. *Nature*, *393*(6684), Article 6684. https://doi.org/10.1038/30918

Wen, Q., & Chklovskii, D. B. (2005). Segregation of the Brain into Gray and White Matter: A Design Minimizing Conduction Delays. *PLOS Computational Biology*, *1*(7), e78. https://doi.org/10.1371/journal.pcbi.0010078

Wen, Z., Nguyen, H. N., Guo, Z., Lalli, M. A., Wang, X., Su, Y., Kim, N.-S., Yoon, K.-J., Shin, J., Zhang, C., Makri, G., Nauen, D., Yu, H., Guzman, E., Chiang, C.-H., Yoritomo, N., Kaibuchi, K., Zou, J., Christian, K. M., … Ming, G. (2014). Synaptic dysregulation in a human iPS cell model of mental disorders. *Nature*, *515*(7527), Article 7527. https://doi.org/10.1038/nature13716

White, J. G., Southgate, E., Thomson, J. N., & Brenner, S. (1986). The Structure of the Nervous System of the Nematode Caenorhabditis elegans. *Philosophical Transactions of the Royal Society of London. Series B, Biological Sciences*, *314*(1165), 1–340.

World Health Organization [WHO]. (1993). The ICD-10 classification of mental and behavioural disorders. *World Health Organization*.

World Health Organization [WHO]. (2023). Depressive disorder (depression) [Fact sheet]. *Geneva, Switzerland: World Health Organization.*

Wray, N. R., Ripke, S., Mattheisen, M., Trzaskowski, M., Byrne, E. M., Abdellaoui, A., Adams, M. J., Agerbo, E., Air, T. M., Andlauer, T. M. F., Bacanu, S.-A., Bækvad-Hansen, M., Beekman, A. F. T., Bigdeli, T. B., Binder, E. B., Blackwood, D. R. H., Bryois, J., Buttenschøn, H. N., Bybjerg-Grauholm, J., … Sullivan, P. F. (2018). Genome-wide association analyses identify 44 risk variants and refine the genetic architecture of major depression. *Nature Genetics*, *50*(5), Article 5. https://doi.org/10.1038/s41588-018-0090-3

Wu, B., Li, X., Zhou, J., Zhang, M., & Long, Q. (2020). Altered Whole-Brain Functional Networks in Drug-Naïve, First-Episode Adolescents With Major Depression Disorder. *Journal of Magnetic Resonance Imaging*, *52*(6), 1790–1798. https://doi.org/10.1002/jmri.27270

Xu, Z., Jiang, H., Zhong, P., Yan, Z., Chen, S., & Feng, J. (2016). Direct conversion of human fibroblasts to induced serotonergic neurons. *Molecular Psychiatry*, *21*(1), Article 1. https://doi.org/10.1038/mp.2015.101

Yamamoto, H., Moriya, S., Ide, K., Hayakawa, T., Akima, H., Sato, S., Kubota, S., Tanii, T., Niwano, M., Teller, S., Soriano, J., & Hirano-Iwata, A. (2018). Impact of modular organization on dynamical richness in cortical networks. *Science Advances*, *4*(11), eaau4914. https://doi.org/10.1126/sciadv.aau4914

Yan, Y., Shin, S., Jha, B. S., Liu, Q., Sheng, J., Li, F., Zhan, M., Davis, J., Bharti, K., Zeng, X., Rao, M., Malik, N., & Vemuri, M. C. (2013). Efficient and Rapid Derivation of Primitive Neural Stem Cells and Generation of Brain Subtype Neurons From Human Pluripotent Stem Cells. *Stem Cells Translational Medicine*, *2*(11), 862–870. https://doi.org/10.5966/sctm.2013-0080

Yang, H., Chen, X., Chen, Z.-B., Li, L., Li, X.-Y., Castellanos, F. X., Bai, T.-J., Bo, Q.-J., Cao, J., Chang, Z.-K., Chen, G.-M., Chen, N.-X., Chen, W., Cheng, C., Cheng, Y.-Q., Cui, X.-L., Duan, J., Fang, Y., Gong, Q.-Y., … Yan, C.-G. (2021). Disrupted intrinsic functional brain topology in patients with major depressive disorder. *Molecular Psychiatry*, *26*(12), Article 12. https://doi.org/10.1038/s41380-021-01247-2

Yang, J., Liu, Z., Tao, H., Cheng, Y., Fan, Z., Sun, F., Ouyang, X., & Yang, J. (2022). Aberrant brain dynamics in major depressive disorder with suicidal ideation. *Journal of Affective Disorders*, *314*, 263–270. https://doi.org/10.1016/j.jad.2022.07.043

Yang, N., Ng, Y. H., Pang, Z. P., Südhof, T. C., & Wernig, M. (2011). Induced Neuronal Cells: How to Make and Define a Neuron. *Cell Stem Cell*, *9*(6), 517–525. https://doi.org/10.1016/j.stem.2011.11.015

Yang, Z., Zuo, X.-N., McMahon, K. L., Craddock, R. C., Kelly, C., de Zubicaray, G. I., Hickie, I., Bandettini, P. A., Castellanos, F. X., Milham, M. P., & Wright, M. J. (2016). Genetic and Environmental Contributions to Functional Connectivity Architecture of the Human Brain. *Cerebral Cortex*, *26*(5), 2341–2352. https://doi.org/10.1093/cercor/bhw027

Ye, M., Qing, P., Zhang, K., & Liu, G. (2016). Altered network efficiency in major depressive disorder. *BMC Psychiatry*, *16*(1), 450. https://doi.org/10.1186/s12888-016-1053-9

Young, M. P. (1992). Objective analysis of the topological organization of the primate cortical visual system. *Nature*, *358*(6382), Article 6382. https://doi.org/10.1038/358152a0

Yu, S., Huang, D., Singer, W., & Nikolić, D. (2008). A Small World of Neuronal Synchrony. *Cerebral Cortex*, *18*(12), 2891–2901. https://doi.org/10.1093/cercor/bhn047

Yuste, R. (2015). From the neuron doctrine to neural networks. *Nature Reviews Neuroscience*, *16*(8), 487–497. https://doi.org/10.1038/nrn3962

Zalesky, A., Fornito, A., Harding, I. H., Cocchi, L., Yücel, M., Pantelis, C., & Bullmore, E. T. (2010). Whole-brain anatomical networks: Does the choice of nodes matter? *NeuroImage*, *50*(3), 970–983. https://doi.org/10.1016/j.neuroimage.2009.12.027

Zeng, L. L., Shen, H., Liu, L., Wang, L., Li, B., Fang, P., Zhou, Z., Li, Y., & Hu, D. (2012). Identifying major depression using whole-brain functional connectivity: A multivariate pattern analysis. *Brain*, *135*(5), Article 5. https://doi.org/10.1093/brain/aws059

Zhang, J., Wang, J., Wu, Q., Kuang, W., Huang, X., He, Y., & Gong, Q. (2011). Disrupted Brain Connectivity Networks in Drug-Naive, First-Episode Major Depressive Disorder. *Biological Psychiatry*, *70*(4), 334–342. https://doi.org/10.1016/j.biopsych.2011.05.018

Zheng, H., Xu, L., Xie, F., Guo, X., Zhang, J., Yao, L., & Wu, X. (2015). The Altered Triple Networks Interaction in Depression under Resting State Based on Graph Theory. *BioMed Research International*, *2015*, e386326. https://doi.org/10.1155/2015/386326

Zhou, C., Zemanová, L., Zamora, G., Hilgetag, C. C., & Kurths, J. (2006). Hierarchical Organization Unveiled by Functional Connectivity in Complex Brain Networks. *Physical Review Letters*, *97*(23), 238103. https://doi.org/10.1103/PhysRevLett.97.238103

Zhou, J., Gennatas, E. D., Kramer, J. H., Miller, B. L., & Seeley, W. W. (2012). Predicting Regional Neurodegeneration from the Healthy Brain Functional Connectome. *Neuron*, *73*(6), 1216–1227. https://doi.org/10.1016/j.neuron.2012.03.004

Zhou, S., & Mondragon, R. J. (2004). The rich-club phenomenon in the Internet topology. *IEEE Communications Letters*, *8*(3), 180–182. https://doi.org/10.1109/LCOMM.2004.823426

Zhu, Y., Wang, D., Liu, Z., & Li, Y. (2018). Aberrant topographical organization in default-mode network in first-episode remitted geriatric depression: A graph-theoretical analysis. *International Psychogeriatrics*, *30*(5), 619–628. https://doi.org/10.1017/S1041610218000054

Zhuang, P., Sun, A. X., An, J., Chua, C. K., & Chew, S. Y. (2018). 3D neural tissue models: From spheroids to bioprinting. *Biomaterials*, *154*, 113–133. https://doi.org/10.1016/j.biomaterials.2017.10.002

Zucker, R. S. (1999). Calcium- and activity-dependent synaptic plasticity. *Current Opinion in Neurobiology*, *9*(3), 305–313. https://doi.org/10.1016/S0959-4388(99)80045-2

Zuckerman, H., Pan, Z., Park, C., Brietzke, E., Musial, N., Shariq, A. S., Iacobucci, M., Yim, S. J., Lui, L. M. W., Rong, C., & McIntyre, R. S. (2018). Recognition and Treatment of Cognitive Dysfunction in Major Depressive Disorder. *Frontiers in Psychiatry*, *9*. https://www.frontiersin.org/articles/10.3389/fpsyt.2018.00655

Appendix A. Method-related material

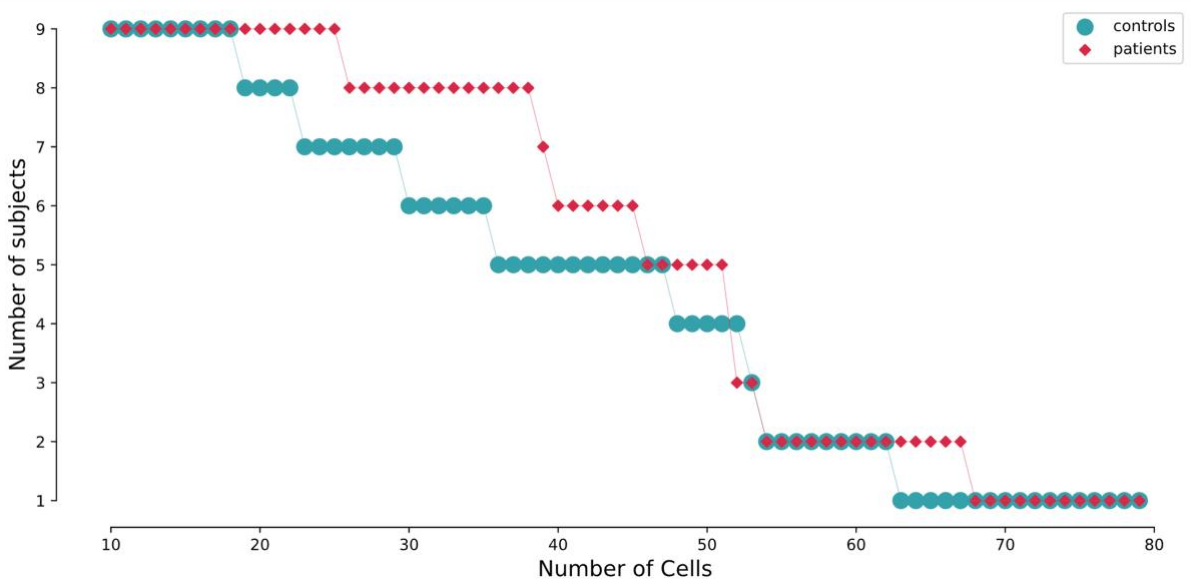

Figure A1. Number of subjects as a function of number of cells in calcium recordings across study groups. This figure illustrates how the number of subjects in the analysis decreases as the number of cells increase. This is due to the variability in the number of cells in the microscale subject data leading to subjects dropping from the analysis as the number of cells increases. Network size of 47 cells was the largest number at which at least 5 subjects from each group were included.

FMRIPrep Methods:

The following was automatically generated by fMRIPrep software and is copied here unchanged:

Results included in this manuscript come from preprocessing performed using *fMRIPrep* 20.2.1
@fmriprep1; @fmriprep2; RRID:SCR_016216),
which is based on *Nipype* 1.5.1
(@nipype1; @nipype2; RRID:SCR_002502).

Anatomical data preprocessing

: A total of 1 T1-weighted (T1w) images were found within the input BIDS dataset.The T1-weighted (T1w) image was corrected for intensity non-uniformity (INU) with

`N4BiasFieldCorrection` [@n4], distributed with ANTs 2.3.3 [@ants, RRID:SCR_004757], and used as T1w-reference throughout the workflow.
The T1w-reference was then skull-stripped with a *Nipype* implementation of the `antsBrainExtraction.sh` workflow (from ANTs), using OASIS30ANTs as target template.
Brain tissue segmentation of cerebrospinal fluid (CSF), white-matter (WM) and gray-matter (GM) was performed on the brain-extracted T1w using `fast` [FSL 5.0.9, RRID:SCR_002823,

@fsl_fast].
Brain surfaces were reconstructed using `recon-all` [FreeSurfer 6.0.1,RRID:SCR_001847, @fs_reconall], and the brain mask estimated previously was refined with a custom variation of the method to reconcile ANTs-derived and FreeSurfer-derived segmentations of the cortical gray-matter of Mindboggle [RRID:SCR_002438, @mindboggle].
Volume-based spatial normalization to two standard spaces (MNI152NLin2009cAsym, MNI152NLin6Asym) was performed through nonlinear registration with `antsRegistration` (ANTs 2.3.3), using brain-extracted versions of both T1w reference and the T1w template.
The following templates were selected for spatial normalization:
ICBM 152 Nonlinear Asymmetrical template version 2009c [@mni152nlin2009casym, RRID:SCR_008796; TemplateFlow ID: MNI152NLin2009cAsym], *FSL's MNI ICBM 152 non-linear 6th Generation Asymmetric Average Brain Stereotaxic Registration Model* [@mni152nlin6asym, RRID:SCR_002823; TemplateFlow ID: MNI152NLin6Asym],

Functional data preprocessing

: For each of the 1 BOLD runs found per subject (across all tasks and sessions), the following preprocessing was performed.
First, a reference volume and its skull-stripped version were generated using a custom methodology of *fMRIPrep*.
A B0-nonuniformity map (or *fieldmap*) was estimated based on a phase-difference map calculated with a dual-echo GRE (gradient-recall echo) sequence, processed with a custom workflow of *SDCFlows* inspired by the [`epidewarp.fsl` script](http://www.nmr.mgh.harvard.edu/~greve/fbirn/b0/epidewarp.fsl) and further improvements in HCP Pipelines [@hcppipelines].
The *fieldmap* was then co-registered to the target EPI (echo-planar imaging) reference run and converted to a displacements field map (amenable to registration tools such as ANTs)

with FSL's `fugue` and other *SDCflows* tools.
Based on the estimated susceptibility distortion, a corrected EPI (echo-planar imaging) reference was calculated for a more accurate co-registration with the anatomical reference.
The BOLD reference was then co-registered to the T1w reference using `bbregister` (FreeSurfer) which implements boundary-based registration [@bbr].
Co-registration was configured with six degrees of freedom.
Head-motion parameters with respect to the BOLD reference (transformation matrices, and six corresponding rotation and translation parameters) are estimated before any spatiotemporal filtering using `mcflirt` [FSL 5.0.9, @mcflirt].BOLD runs were slice-time corrected using `3dTshift` from AFNI 20160207 [@afni, RRID:SCR_005927].
The BOLD time-series were resampled onto the following surfaces (FreeSurfer reconstruction nomenclature):
fsaverage.

The BOLD time-series (including slice-timing correction when applied) were resampled onto their original, native space by applying a single, composite transform to correct for head-motion and susceptibility distortions.
These resampled BOLD time-series will be referred to as *preprocessed BOLD in original space*, or just *preprocessed BOLD*.
The BOLD time-series were resampled into standard space, generating a *preprocessed BOLD run in MNI152NLin2009cAsym space*.
First, a reference volume and its skull-stripped version were generated using a custom methodology of *fMRIPrep*.
Grayordinates files [@hcppipelines] containing 91k samples were also generated using the highest-resolution ``fsaverage`` as intermediate standardized surface space.
Several confounding time-series were calculated based on the *preprocessed BOLD*: framewise displacement (FD), DVARS and three region-wise global signals.
FD was computed using two formulations following Power (absolute sum of relative motions, @power_fd_dvars) and Jenkinson (relative root mean square displacement between affines, @mcflirt).
FD and DVARS are calculated for each functional run, both using their implementations in *Nipype* [following the definitions by @power_fd_dvars].
The three global signals are extracted within the CSF, the WM, and the whole-brain masks.
Additionally, a set of physiological regressors were extracted to allow for component-based noise correction [*CompCor*, @compcor].

Principal components are estimated after high-pass filtering the *preprocessed BOLD* time-series (using a discrete cosine filter with 128s cut-off) for the two *CompCor* variants: temporal (tCompCor) and anatomical (aCompCor).
tCompCor components are then calculated from the top 2% variable voxels within the brain mask.
For aCompCor, three probabilistic masks (CSF, WM and combined CSF+WM) are generated in anatomical space.
The implementation differs from that of Behzadi et al. in that instead of eroding the masks by 2 pixels on BOLD space, the aCompCor masks are subtracted a mask of pixels that likely contain a volume fraction of GM.
This mask is obtained by dilating a GM mask extracted from the FreeSurfer's *aseg* segmentation, and it ensures components are not extracted from voxels containing a minimal fraction of GM.
Finally, these masks are resampled into BOLD space and binarized by thresholding at 0.99 (as in the original implementation).
Components are also calculated separately within the WM and CSF masks.
For each CompCor decomposition, the *k* components with the largest singular values are retained, such that the retained components' time series are sufficient to explain 50 percent of variance across the nuisance mask (CSF, WM, combined, or temporal). The remaining components are dropped from consideration.
The head-motion estimates calculated in the correction step were also placed within the corresponding confounds file.
The confound time series derived from head motion estimates and global signals were expanded with the inclusion of temporal derivatives and quadratic terms for each [@confounds_satterthwaite_2013].
Frames that exceeded a threshold of 0.5 mm FD or 1.5 standardised DVARS were annotated as motion outliers.
All resamplings can be performed with *a single interpolation step* by composing all the pertinent transformations (i.e. head-motion transform matrices, susceptibility distortion correction when available, and co-registrations to anatomical and output spaces).
Gridded (volumetric) resamplings were performed using `antsApplyTransforms` (ANTs), configured with Lanczos interpolation to minimize the smoothing effects of other kernels [@lanczos].
Non-gridded (surface) resamplings were performed using `mri_vol2surf` (FreeSurfer).

Many internal operations of *fMRIPrep* use *Nilearn* 0.6.2 [@nilearn, RRID:SCR_001362], mostly within the functional processing workflow.
For more details of the pipeline, see [the section corresponding to workflows in *fMRIPrep*'s zocumentation](https://fmriprep.readthedocs.io/en/latest/workflows.html "FMRIPrep's documentation").

Copyright Waiver

The above boilerplate text was automatically generated by fMRIPrep with the express intention that users should copy and paste this text into their manuscripts *unchanged*.

It is released under the [CC0](https://creativecommons.org/publicdomain/zero/1.0/) license.

Demographic questionnaire:

Demographischer Fragebogen Code: ☐ Datum: ☐☐☐☐

Angaben zur Person: Bitte kreuzen Sie die für Sie zutreffenden Antworten an.

Alter _____Jahre

Geschlecht
- ☐ weiblich
- ☐ männlich
- ☐ andere
- ☐ keine Angabe

Händigkeit
- ☐ rechts
- ☐ links
- ☐ beide

Familienstand
- ☐ ledig, allein lebend
- ☐ ledig, mit Partner/in lebend
- ☐ verheiratet
- ☐ verwitwet
- ☐ geschieden, getrennt lebend
- ☐ geschieden, mit Partner/in lebend

Höchster Schulabschluß
- ☐ Volks-,Hauptschulabschluß
- ☐ mittlere Reife
- ☐ Fachhochschulreife
- ☐ Hochschulreife

Derzeitige Tätigkeit
- ☐ im Studium / in Ausbildung
- ☐ teilzeitbeschäftigt
- ☐ voll berufstätig
- ☐ Sonstiges

Ich nehme folgende Medikamente ein:

PANAS:

PANAS

Dieser Fragebogen enthält eine Reihe von Wörtern, die unterschiedliche Gefühle und Empfindungen beschreiben. Lesen Sie jedes Wort und tragen Sie dann in die Skala neben jedem Wort die Intensität ein. Sie haben die Möglichkeit, zwischen fünf Abstufungen zu wählen:

1. ganz wenig oder gar nicht 2. ein bißchen 3. einigermaßen 4. erheblich 5. äußerst

Geben Sie bitte an, wie Sie sich im Moment fühlen.

	ganz wenig oder gar nicht	ein bißchen	einiger-maßen	erheblich	äußerst
aktiv	O	O	O	O	O
bekümmert	O	O	O	O	O
interessiert	O	O	O	O	O
freudig erregt	O	O	O	O	O
verärgert	O	O	O	O	O
stark	O	O	O	O	O
schuldig	O	O	O	O	O
erschrocken	O	O	O	O	O
feindselig	O	O	O	O	O
angeregt	O	O	O	O	O
stolz	O	O	O	O	O
gereizt	O	O	O	O	O
begeistert	O	O	O	O	O
beschämt	O	O	O	O	O
wach	O	O	O	O	O
nervös	O	O	O	O	O
entschlossen	O	O	O	O	O
aufmerksam	O	O	O	O	O
durcheinander	O	O	O	O	O
ängstlich	O	O	O	O	O

Beck's Depression Inventory (BDI):

B D I

Die folgenden beiden Seiten enthalten 21 Gruppen von Aussagen. Bitte lesen Sie jede Gruppe sorgfältig durch. Kreuzen Sie dann die eine Aussage jeder Gruppe an, die am besten beschreibt, wie Sie sich **in dieser Woche einschließlich heute** gefühlt haben! Falls mehrere Aussagen in einer Gruppe gleichermaßen zuzutreffen scheinen, können Sie auch mehrere Ziffern ankreuzen. **Lesen Sie auf jeden Fall alle Aussagen in jeder Gruppe, bevor Sie Ihre Wahl treffen.**

A

0 Ich fühle mich nicht traurig.
1 Ich fühle mich traurig.
2 Ich bin die ganze Zeit traurig und komme nicht davon los.
3 Ich bin so traurig oder unglücklich, dass ich es kaum noch ertrage.

B

0 Ich sehe nicht besonders mutlos in die Zukunft.
1 Ich sehe mutlos in die Zukunft
2 Ich habe nichts, worauf ich mich freuen kann.
3 Ich habe das Gefühl, dass die Zukunft hoffnungslos ist, und dass die Situation nicht besser werden kann.

C

0 Ich fühle mich nicht als Versager.
1 Ich habe das Gefühl, öfter zu versagt zu haben als der Durchschnitt.
2 Wenn ich auf mein Leben zurückblicke, sehe ich bloß eine Menge Fehlschläge.
3 Ich habe das Gefühl, als Mensch ein völliger Versager zu sein.

D

0 Ich kann die Dinge genauso genießen wie früher.
1 Ich kann die Dinge nicht mehr so genießen wie früher.
2 Ich kann aus nichts mehr eine echte Befriedigung mehr ziehen.
3 Ich bin mit allem unzufrieden oder gelangweilt.

E

0 Ich habe keine Schuldgefühle.
1 Ich habe häufig Schuldgefühle.
2 Ich habe fast immer Schuldgefühle.
3 Ich habe immer Schuldgefühle.

F

0 Ich habe nicht das Gefühl, gestraft zu sein.
1 Ich habe das Gefühl, vielleicht bestraft zu sein.
2 Ich erwarte, bestraft zu werden.
3 Ich habe das Gefühl, bestraft zu gehören.

G

0 Ich bin nicht von mir enttäuscht.
1 Ich bin von mir enttäuscht.
2 Ich finde mich fürchterlich.
3 Ich hasse mich.

H

0 Ich habe nicht das Gefühl, schlechter zu sein als alle anderen.
1 Ich kritisiere mich wegen meiner Fehler oder Schwächen.
2 Ich mache mir die ganze Zeit Vorwürfe wegen meiner Mängel.
3 Ich gebe mir für alles die Schuld was schief geht.

I

0 Ich denke nicht daran, mir etwas anzutun.
1 Ich denke manchmal an Selbstmord, ich würde es aber nicht tun.
2 Ich möchte mich am liebsten umbringen.
3 Ich würde mich umbringen, wenn ich es könnte.

J

0 Ich weine nicht öfter als früher.
1 Ich weine jetzt mehr als früher.
2 Ich weine jetzt die ganze Zeit.
3 Früher konnte ich weinen, aber jetzt kann ich es nicht mehr, obwohl ich es möchte.

K

0 Ich bin nicht reizbarer als sonst.
1 Ich bin jetzt leichter verärgert oder gereizt als früher.
2 Ich fühle mich dauernd gereizt.
3 Die Dinge die mich früher geärgert haben, berühren mich nicht mehr.

L

0 Ich habe nicht das Interesse an anderen Menschen verloren.
1 Ich interessiere mich jetzt weniger für andere Menschen als früher.
2 Ich habe mein Interesse an anderen Menschen zum größten Teil verloren.
3 Ich habe mein ganzes Interesse an anderen Menschen verloren.

M

0 Ich bin so entschlussfreudig wie immer.
1 Ich schiebe jetzt Entscheidungen öfter als früher auf.
2 Es fällt mir jetzt schwerer als früher, Entscheidungen zu treffen.
3 Ich kann überhaupt keine Entscheidungen mehr treffen.

N

0 Ich habe nicht das Gefühl schlechter auszusehen als früher.
1 Ich mache mir Sorgen, dass ich alt oder unattraktiv aussehe.
2 Ich habe das Gefühl, dass in meinem Aussehen Veränderungen eingetreten sind, die mich unattraktiv machen.
3 Ich finde mich hässlich.

O

0 Ich kann genauso gut arbeiten wie früher.
1 Ich muss mir einen Ruck geben, bevor ich eine Tätigkeit in Angriff nehme.
2 Ich muss mich zu jeder Tätigkeit zwingen.
3 Ich bin unfähig zu arbeiten.

P

0 Ich schlafe so gut wie sonst.
1 Ich schlafe nicht mehr so gut wie früher.
2 Ich wache 1 bis 2 Stunden früher auf als sonst, und es fällt mir schwer wieder einzuschlafen.
3 Ich wache mehrere Stunden früher auf als sonst und kann nicht mehr einschlafen.

Q

0 Ich ermüde nicht stärker als sonst.
1 Ich ermüde schneller als früher.
2 Fast alles ermüdet mich.
3 Ich bin zu müde um etwas zu tun.

R

0 Mein Appetit ist nicht schlechter als sonst.
1 Mein Appetit ist nicht mehr so gut wie früher.
2 Mein Appetit hat sehr stark nachgelassen.
3 Ich habe überhaupt keinen Appetit mehr.

S

0 Ich habe in letzter Zeit kaum abgenommen.
1 Ich habe mehr als zwei Kilo abgenommen.
2 Ich habe mehr als fünf Kilo abgenommen.
3 Ich habe mehr als acht Kilo abgenommen.

Ich esse absichtlich weniger, um abzunehmen:
ja nein

T

0 Ich mache mir keine größeren Sorgen um meine Gesundheit als sonst.
1 Ich mache mir Sorgen über körperliche Probleme, wie Schmerzen, Magenbeschwerden oder Verstopfung.
2 Ich mache mir so große Sorgen über gesundheitliche Probleme, dass es mir schwer fällt, an etwas anderes zu denken.
3 Ich mache mir so große Sorgen über meine gesundheitlichen Probleme, dass ich an nichts anderes denken kann.

U

0 Ich habe in letzter Zeit keine Veränderung meines Interesses an Sexualität bemerkt.
1 Ich interessiere mich jetzt weniger für Sexualität als früher.
2 Ich interessiere mich jetzt viel weniger für Sexualität.
3 Ich habe das Interesse für Sexualität völlig verloren.

Appendix B. Result-related material

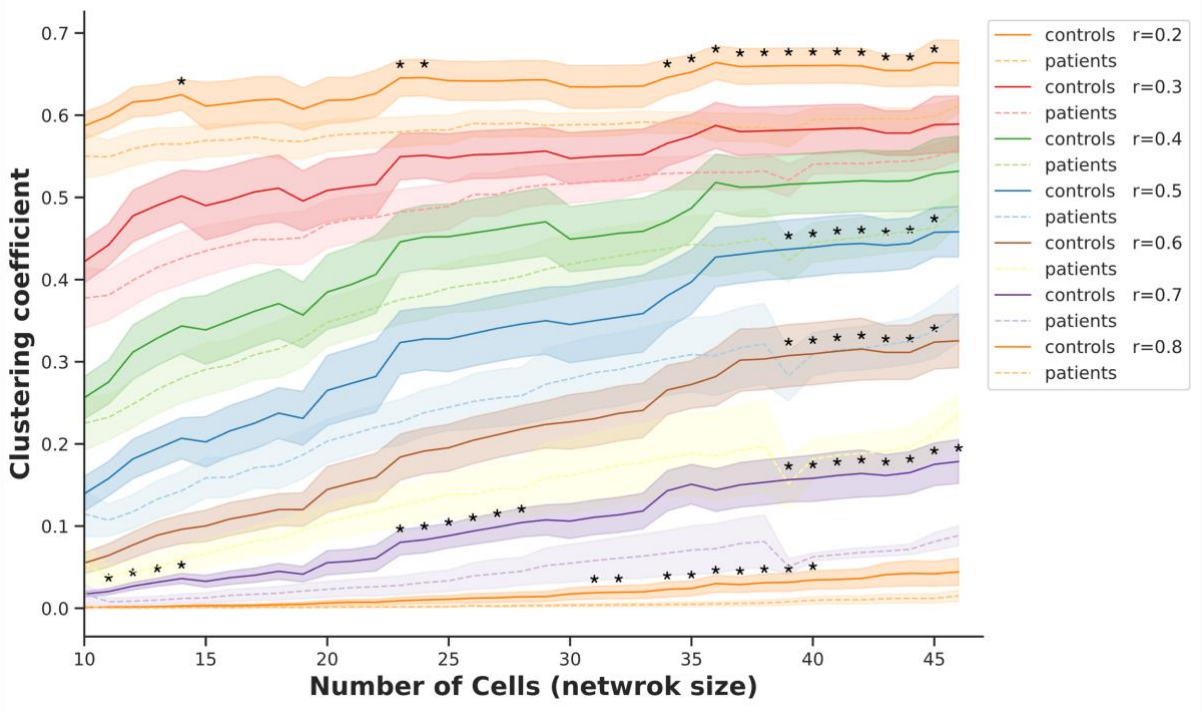

Figure B1. Decreased *clustering coefficient* in patient-derived neurons compared to controls across varying network thresholds and sizes. *C* showed a significant overall reduction (p=0.04) in neuronal cultures of MDD patients (dashed lines) compared to controls (solid lines) across network sizes and all correlation thresholds r_{thresh} (depicted in different colors). *C* was significantly higher when lower r_{thresh} were applied (p< 0.001) and for larger network sizes (p< 0.001). We explored the levels of network sizes and r_{thresh} at which group differences in *C* occurred. Asterisks (*) indicate the presence of statistically significant difference (p<0.05, uncorrected). The shaded area represents the standard error of the mean (SEM) (instead of confidance coefficient shown in the main text) for better visability.

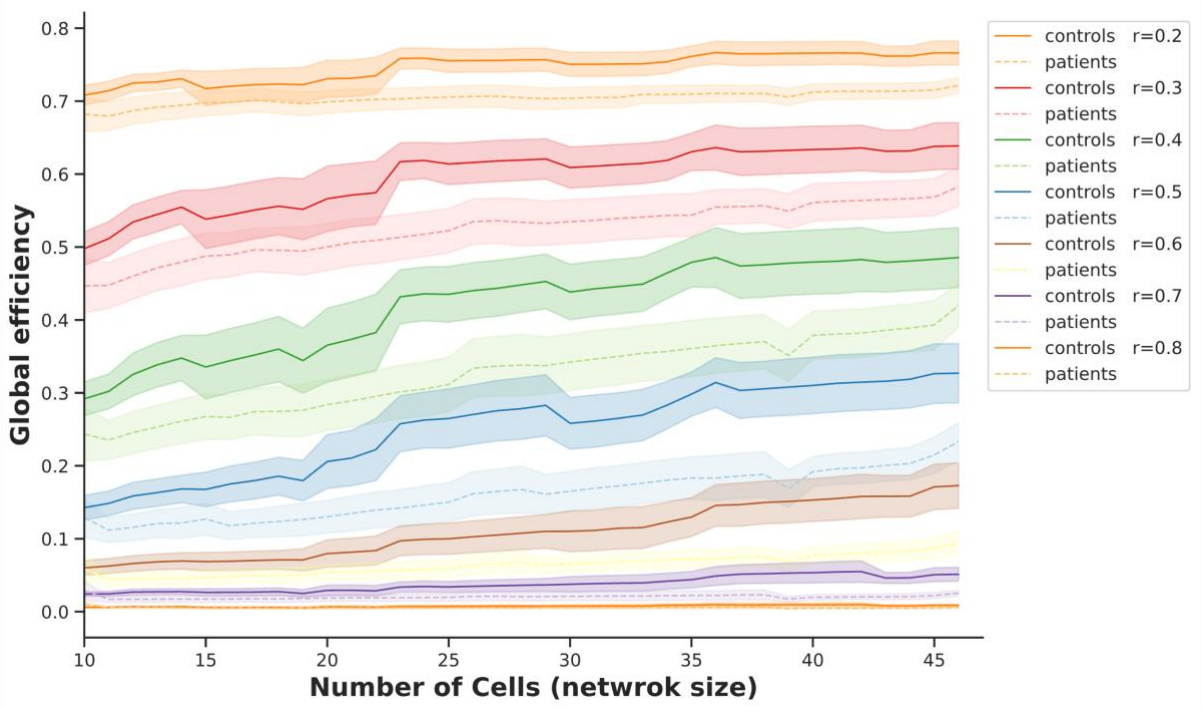

Figure B2. Alterations in *global efficiency* across experimental groups, thresholds, and network sizes. Changes in mean E_{glob} in graphs of depressed patients (dashed lines) compared to controls (solid lines) across different network sizes and correlation r_{thresh} (depicted by difference colors). Although an overall trend of lower E_{glob} in MDD neuronal cultures is present, no statistically significant group differences in network integration capacity could be detected ($p=0.194$). E_{glob} significantly increased as the networks grew larger ($p< 0.001$) and as r_{thresh} became more liberal ($p< 0.001$). The shaded area represents the standard error of the mean (SEM) (instead of confidance coefficient shown in the main text) for better visability.

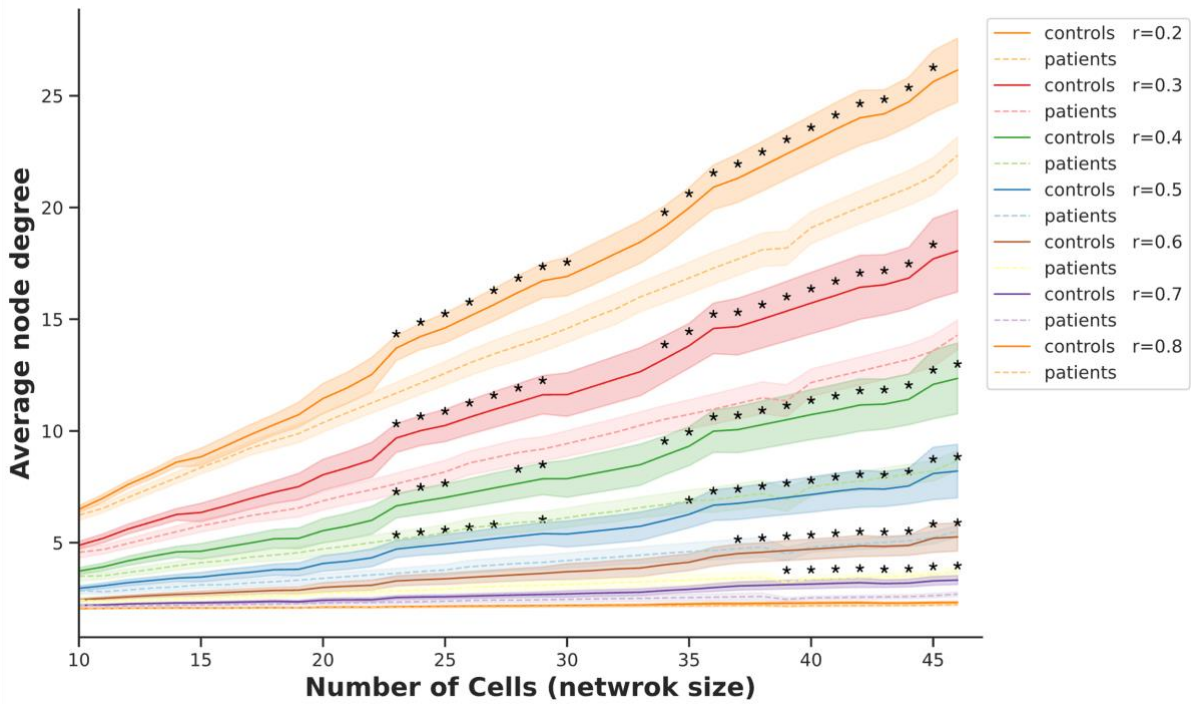

Figure B3. Decreased *average node degree* in patient-derived neurons compared to controls across varying network thresholds and sizes. *ANDeg* showed a significant overall decrease (p=0.048) in graphs of depressed patients (dashed lines) compared to controls (solid lines) across varying network sizes and r_{thresh} (depicted in different colors). *ANDeg* significantly increased with larger network sizes (p<0.001) and lower r_{thresh} (p<0.001). We explored the levels of network sizes and r_{thresh} at which group differences in *ANDeg* occurred. Asterisks (*) indicate the presence of statistically significant difference (p<0.05, uncorrected). The shaded area represents the standard error of the mean (SEM) for better visability (instead of confidance interval shown in the main text).

Table B1. Descriptive statistics of *C* of *in vitro* neural networks of experimental groups across thresholds and network sizes.

Threshold	Network size	Group	Mean *C*	Confidence interval *C*	t-values	p-values
0,2	10	control	0,5871	0.0312/0.0295	1,1751	0,2544
0,2	10	patient	0,5503	0.0466/0.0502		
0,2	11	control	0,5986	0.0319/0.0286	1,8850	0,0762
0,2	11	patient	0,5492	0.0358/0.0399		
0,2	12	control	0,6161	0.0349/0.0329	2,0699	0,0512
0,2	12	patient	0,5592	0.036/0.0389		
0,2	13	control	0,6186	0.0345/0.0327	1,9840	0,0618
0,2	13	patient	0,5650	0.0342/0.0383		
0,2	14	control	0,6250	0.0363/0.0333	2,1842	0,0442
0,2	14	patient	0,5649	0.0357/0.0373		
0,2	15	control	0,6111	0.049/0.0556	1,2076	0,2378
0,2	15	patient	0,5691	0.0355/0.0385		
0,2	16	control	0,6145	0.0484/0.053	1,3169	0,203
0,2	16	patient	0,5699	0.0357/0.0359		
0,2	17	control	0,6182	0.05/0.0554	1,3202	0,2056
0,2	17	patient	0,5734	0.0334/0.0356		
0,2	18	control	0,6195	0.0502/0.0524	1,4396	0,1712
0,2	18	patient	0,5687	0.0377/0.0419		
0,2	19	control	0,6075	0.0447/0.0506	1,1742	0,2596
0,2	19	patient	0,5681	0.0376/0.0409		
0,2	20	control	0,6180	0.0476/0.0548	1,2946	0,2182
0,2	20	patient	0,5748	0.0343/0.0369		
0,2	21	control	0,6189	0.0457/0.0526	1,2854	0,2208
0,2	21	patient	0,5772	0.0339/0.0352		
0,2	22	control	0,6263	0.0485/0.0553	1,4487	0,1668
0,2	22	patient	0,5784	0.0325/0.0351		
0,2	23	control	0,6452	0.0394/0.041	2,2991	0,0412
0,2	23	patient	0,5797	0.0324/0.0334		
0,2	24	control	0,6458	0.0387/0.0413	2,2853	0,042
0,2	24	patient	0,5819	0.0312/0.033		
0,2	25	control	0,6421	0.0429/0.0441	2,0616	0,0656
0,2	25	patient	0,5821	0.0313/0.034		
0,2	26	control	0,6416	0.0427/0.0435	1,8585	0,0888
0,2	26	patient	0,5899	0.0277/0.0303		
0,2	27	control	0,6417	0.0424/0.0441	1,8633	0,0884
0,2	27	patient	0,5893	0.0273/0.0303		
0,2	28	control	0,6428	0.0429/0.0429	1,8729	0,0854
0,2	28	patient	0,5904	0.028/0.0299		
0,2	29	control	0,6431	0.0413/0.0431	2,0729	0,0604
0,2	29	patient	0,5877	0.0246/0.0284		

Threshold	Network size	Group	Mean *C*	Confidence interval *C*	t-values	p-values
0,2	30	control	0,6346	0.0474/0.0458	1,6727	0,11655012
0,2	30	patient	0,5884	0.0236/0.0282		
0,2	31	control	0,6343	0.0466/0.0454	1,6413	0,12354312
0,2	31	patient	0,5885	0.0239/0.0281		
0,2	32	control	0,6351	0.0471/0.0447	1,6590	0,12087912
0,2	32	patient	0,5894	0.0242/0.0273		
0,2	33	control	0,6354	0.0468/0.0446	1,6307	0,12820513
0,2	33	patient	0,5917	0.0223/0.0256		
0,2	34	control	0,6460	0.0406/0.0378	2,2678	0,04895105
0,2	34	patient	0,5907	0.0223/0.0257		
0,2	35	control	0,6523	0.0381/0.0383	2,5862	0,02597403
0,2	35	patient	0,5910	0.0225/0.0247		
0,2	36	control	0,6640	0.0341/0.0364	2,8991	0,01398601
0,2	36	patient	0,5852	0.0287/0.034		
0,2	37	control	0,6592	0.0389/0.036	2,6662	0,01942502
0,2	37	patient	0,5852	0.0276/0.0345		
0,2	38	control	0,6597	0.0384/0.0356	2,7078	0,01787102
0,2	38	patient	0,5848	0.0281/0.0337		
0,2	39	control	0,6603	0.0379/0.0354	2,7700	0,01767677
0,2	39	patient	0,5803	0.0313/0.0379		
0,2	40	control	0,6604	0.0355/0.0355	2,6685	0,02164502
0,2	40	patient	0,5945	0.0221/0.0269		
0,2	41	control	0,6606	0.0376/0.0351	2,6595	0,02164502
0,2	41	patient	0,5955	0.0215/0.0268		
0,2	42	control	0,6599	0.0357/0.0357	2,6081	0,02164502
0,2	42	patient	0,5954	0.0217/0.0274		
0,2	43	control	0,6544	0.038/0.0329	2,5166	0,02380952
0,2	43	patient	0,5957	0.0219/0.0263		
0,2	44	control	0,6543	0.0337/0.0325	2,5643	0,02597403
0,2	44	patient	0,5950	0.022/0.027		
0,2	45	control	0,6640	0.0533/0.0414	2,1836	0,03463203
0,2	45	patient	0,5987	0.0232/0.0299		
0,2	46	control	0,6636	0.0537/0.0426	1,7770	0,07936508
0,2	46	patient	0,6115	0.0159/0.017		
0,2	47	control	0,6639	0.0538/0.0416	1,7853	0,07936508
0,2	47	patient	0,6114	0.0157/0.0171		
0,3	10	control	0,4219	0.0464/0.0512	0,9851	0,3368
0,3	10	patient	0,3775	0.0678/0.067		
0,3	11	control	0,4423	0.0457/0.0489	1,5414	0,145
0,3	11	patient	0,3810	0.055/0.0573		
0,3	12	control	0,4774	0.0577/0.0582	1,7851	0,0914
0,3	12	patient	0,3991	0.0555/0.0579		

Threshold	Network size	Group	Mean *C*	Confidence interval *C*	t-values	p-values
0,3	13	control	0,4904	0.0586/0.0576	1,7277	0,1002
0,3	13	patient	0,4148	0.0524/0.0574		
0,3	14	control	0,5017	0.0582/0.0562	1,6971	0,1074
0,3	14	patient	0,4258	0.0572/0.0594		
0,3	15	control	0,4900	0.0722/0.079	1,0659	0,2962
0,3	15	patient	0,4350	0.055/0.0568		
0,3	16	control	0,4972	0.0736/0.0799	1,0996	0,2836
0,3	16	patient	0,4419	0.0521/0.0539		
0,3	17	control	0,5066	0.0733/0.0756	1,1787	0,2546
0,3	17	patient	0,4487	0.0514/0.0527		
0,3	18	control	0,5112	0.0741/0.0773	1,2152	0,2426
0,3	18	patient	0,4489	0.0567/0.0595		
0,3	19	control	0,4956	0.0631/0.0711	0,9233	0,3694
0,3	19	patient	0,4511	0.058/0.0585		
0,3	20	control	0,5085	0.0661/0.0728	0,8603	0,406
0,3	20	patient	0,4676	0.0516/0.0562		
0,3	21	control	0,5126	0.0637/0.0706	0,8468	0,4128
0,3	21	patient	0,4734	0.0506/0.0529		
0,3	22	control	0,5158	0.0652/0.0741	0,8588	0,4054
0,3	22	patient	0,4758	0.0509/0.0519		
0,3	23	control	0,5495	0.05/0.0531	1,6727	0,1144
0,3	23	patient	0,4822	0.0494/0.0528		
0,3	24	control	0,5512	0.0487/0.0517	1,6467	0,119
0,3	24	patient	0,4855	0.0497/0.0521		
0,3	25	control	0,5479	0.0509/0.0536	1,4288	0,1724
0,3	25	patient	0,4890	0.0505/0.054		
0,3	26	control	0,5518	0.0518/0.0518	1,2421	0,2336
0,3	26	patient	0,5035	0.0454/0.0496		
0,3	27	control	0,5526	0.0521/0.0525	1,2481	0,231
0,3	27	patient	0,5036	0.0462/0.0502		
0,3	28	control	0,5543	0.0513/0.0528	1,1162	0,2766
0,3	28	patient	0,5120	0.043/0.0478		
0,3	29	control	0,5564	0.0504/0.052	1,1115	0,2818
0,3	29	patient	0,5154	0.0403/0.0466		
0,3	30	control	0,5474	0.0582/0.0558	0,7898	0,44522145
0,3	30	patient	0,5169	0.0416/0.0455		
0,3	31	control	0,5496	0.0555/0.0555	0,7961	0,44322344
0,3	31	patient	0,5193	0.0403/0.0451		
0,3	32	control	0,5509	0.0559/0.0536	0,7819	0,45088245
0,3	32	patient	0,5213	0.0393/0.0454		
0,3	33	control	0,5521	0.0555/0.0552	0,6892	0,5004995
0,3	33	patient	0,5274	0.0374/0.0388		

Threshold	Network size	Group	Mean *C*	Confidence interval *C*	t-values	p-values
0,3	34	control	0,5657	0.0502/0.0482	1,0972	0,29437229
0,3	34	patient	0,5291	0.0349/0.0379		
0,3	35	control	0,5744	0.0467/0.0476	1,3573	0,1968032
0,3	35	patient	0,5301	0.0355/0.0385		
0,3	36	control	0,5876	0.0433/0.0514	1,6240	0,12587413
0,3	36	patient	0,5306	0.0369/0.042		
0,3	37	control	0,5800	0.0503/0.0515	1,3899	0,18881119
0,3	37	patient	0,5303	0.0374/0.0423		
0,3	38	control	0,5809	0.0498/0.0498	1,3767	0,18958819
0,3	38	patient	0,5322	0.0368/0.0414		
0,3	39	control	0,5818	0.0498/0.0507	1,7895	0,09974747
0,3	39	patient	0,5208	0.032/0.038		
0,3	40	control	0,5827	0.0497/0.0509	1,4272	0,18181818
0,3	40	patient	0,5403	0.0227/0.0212		
0,3	41	control	0,5840	0.0493/0.0507	1,4407	0,17748918
0,3	41	patient	0,5414	0.0223/0.0216		
0,3	42	control	0,5844	0.0485/0.0487	1,4879	0,16883117
0,3	42	patient	0,5410	0.0216/0.0219		
0,3	43	control	0,5783	0.0477/0.0413	1,2646	0,22294372
0,3	43	patient	0,5434	0.0215/0.0209		
0,3	44	control	0,5783	0.048/0.0439	1,2223	0,24025974
0,3	44	patient	0,5441	0.0229/0.0218		
0,3	45	control	0,5885	0.0659/0.0505	1,1033	0,32467532
0,3	45	patient	0,5494	0.0295/0.0248		
0,3	46	control	0,5892	0.0656/0.0501	0,8101	0,50793651
0,3	46	patient	0,5589	0.0299/0.0195		
0,3	47	control	0,5895	0.0656/0.0502	0,7685	0,53968254
0,3	47	patient	0,5607	0.0295/0.0197		
0,4	10	control	0,2563	0.047/0.0483	0,7441	0,4662
0,4	10	patient	0,2252	0.0643/0.0574		
0,4	11	control	0,2754	0.0481/0.05	1,1274	0,2734
0,4	11	patient	0,2324	0.052/0.0485		
0,4	12	control	0,3118	0.0615/0.0607	1,4561	0,1636
0,4	12	patient	0,2484	0.0542/0.0509		
0,4	13	control	0,3286	0.0614/0.0603	1,4172	0,171
0,4	13	patient	0,2662	0.0548/0.0536		
0,4	14	control	0,3435	0.0612/0.0619	1,4000	0,1776
0,4	14	patient	0,2799	0.0553/0.0538		
0,4	15	control	0,3387	0.0733/0.0818	0,9127	0,362
0,4	15	patient	0,2907	0.0609/0.0571		
0,4	16	control	0,3500	0.0744/0.0809	1,0252	0,3168
0,4	16	patient	0,2963	0.0581/0.0524		

Threshold	Network size	Group	Mean *C*	Confidence interval *C*	t-values	p-values
0,4	17	control	0,3614	0.0759/0.0822	1,0082	0,3282
0,4	17	patient	0,3085	0.0587/0.0543		
0,4	18	control	0,3708	0.0741/0.0805	1,0140	0,3284
0,4	18	patient	0,3155	0.0647/0.0618		
0,4	19	control	0,3568	0.0677/0.0775	0,5332	0,5976
0,4	19	patient	0,3287	0.0642/0.0635		
0,4	20	control	0,3848	0.0783/0.0879	0,6957	0,5008
0,4	20	patient	0,3480	0.0574/0.0501		
0,4	21	control	0,3941	0.0793/0.0875	0,7038	0,4882
0,4	21	patient	0,3566	0.0578/0.0491		
0,4	22	control	0,4062	0.0829/0.0858	0,7446	0,4602
0,4	22	patient	0,3656	0.0588/0.0503		
0,4	23	control	0,4458	0.0676/0.0714	1,4785	0,163
0,4	23	patient	0,3757	0.0587/0.0499		
0,4	24	control	0,4518	0.0674/0.0739	1,4698	0,164
0,4	24	patient	0,3809	0.058/0.0506		
0,4	25	control	0,4522	0.0712/0.0732	1,2789	0,221
0,4	25	patient	0,3897	0.0597/0.0508		
0,4	26	control	0,4567	0.0728/0.0755	1,2034	0,25
0,4	26	patient	0,3944	0.0652/0.055		
0,4	27	control	0,4610	0.0749/0.0746	1,2161	0,2408
0,4	27	patient	0,3979	0.0653/0.055		
0,4	28	control	0,4661	0.0756/0.0764	1,1860	0,2566
0,4	28	patient	0,4039	0.066/0.056		
0,4	29	control	0,4703	0.0744/0.0772	1,0518	0,307
0,4	29	patient	0,4126	0.0758/0.0596		
0,4	30	control	0,4492	0.0706/0.0714	0,5643	0,58474858
0,4	30	patient	0,4187	0.0718/0.0586		
0,4	31	control	0,4522	0.0713/0.0716	0,5144	0,61471861
0,4	31	patient	0,4242	0.0727/0.0587		
0,4	32	control	0,4563	0.0717/0.0731	0,5094	0,61904762
0,4	32	patient	0,4286	0.0704/0.0581		
0,4	33	control	0,4586	0.0723/0.0723	0,4589	0,65301365
0,4	33	patient	0,4339	0.0717/0.0571		
0,4	34	control	0,4707	0.0692/0.0692	0,6272	0,54045954
0,4	34	patient	0,4374	0.0694/0.0569		
0,4	35	control	0,4869	0.0673/0.0737	0,8336	0,41924742
0,4	35	patient	0,4430	0.0688/0.0566		
0,4	36	control	0,5182	0.05/0.0653	1,4043	0,18648019
0,4	36	patient	0,4411	0.0717/0.0617		
0,4	37	control	0,5123	0.0577/0.0666	1,2196	0,24553225
0,4	37	patient	0,4453	0.0704/0.0632		

Threshold	Network size	Group	Mean *C*	Confidence interval *C*	t-values	p-values
0,4	38	control	0,5130	0.059/0.0695	1,1364	0,27661228
0,4	38	patient	0,4499	0.0728/0.0648		
0,4	39	control	0,5159	0.058/0.0684	2,1100	0,06186869
0,4	39	patient	0,4235	0.0458/0.0491		
0,4	40	control	0,5172	0.0594/0.0696	1,7059	0,11904762
0,4	40	patient	0,4452	0.0399/0.0444		
0,4	41	control	0,5186	0.0604/0.0677	1,6501	0,13852814
0,4	41	patient	0,4481	0.0387/0.0464		
0,4	42	control	0,5202	0.0602/0.0683	1,6011	0,15151515
0,4	42	patient	0,4515	0.0406/0.0453		
0,4	43	control	0,5195	0.0584/0.0733	1,5096	0,17316017
0,4	43	patient	0,4555	0.0394/0.0449		
0,4	44	control	0,5202	0.0586/0.0707	1,4406	0,19047619
0,4	44	patient	0,4588	0.0397/0.0465		
0,4	45	control	0,5288	0.071/0.0732	1,3846	0,2034632
0,4	45	patient	0,4629	0.044/0.0487		
0,4	46	control	0,5318	0.0712/0.0728	0,9688	0,34126984
0,4	46	patient	0,4866	0.0361/0.0274		
0,4	47	control	0,5326	0.0715/0.073	0,9029	0,38888889
0,4	47	patient	0,4902	0.0363/0.028		
0,5	10	control	0,1395	0.0404/0.0366	0,7189	0,4892
0,5	10	patient	0,1147	0.0541/0.0456		
0,5	11	control	0,1579	0.04/0.0367	1,7798	0,0984
0,5	11	patient	0,1072	0.0385/0.0332		
0,5	12	control	0,1818	0.044/0.0456	2,0292	0,0598
0,5	12	patient	0,1175	0.0417/0.0351		
0,5	13	control	0,1943	0.0434/0.0471	1,8524	0,0814
0,5	13	patient	0,1328	0.0448/0.0381		
0,5	14	control	0,2069	0.0437/0.0477	1,8597	0,0804
0,5	14	patient	0,1428	0.0465/0.0408		
0,5	15	control	0,2024	0.0553/0.0573	1,1130	0,271
0,5	15	patient	0,1587	0.0474/0.0439		
0,5	16	control	0,2159	0.0555/0.058	1,4341	0,1692
0,5	16	patient	0,1595	0.0485/0.0415		
0,5	17	control	0,2251	0.0543/0.0621	1,3623	0,1902
0,5	17	patient	0,1709	0.0476/0.0425		
0,5	18	control	0,2375	0.0538/0.0584	1,5106	0,1506
0,5	18	patient	0,1739	0.0542/0.0509		
0,5	19	control	0,2311	0.0561/0.0618	1,0152	0,3352
0,5	19	patient	0,1868	0.0539/0.0514		
0,5	20	control	0,2651	0.0757/0.0795	1,2627	0,2322
0,5	20	patient	0,2034	0.0526/0.0468		

Threshold	Network size	Group	Mean *C*	Confidence interval *C*	t-values	p-values
0,5	21	control	0,2738	0.0763/0.078	1,2665	0,2314
0,5	21	patient	0,2114	0.0508/0.048		
0,5	22	control	0,2821	0.0786/0.0783	1,2398	0,2412
0,5	22	patient	0,2204	0.0507/0.0464		
0,5	23	control	0,3233	0.0699/0.0701	2,0930	0,0552
0,5	23	patient	0,2265	0.0534/0.0493		
0,5	24	control	0,3278	0.0708/0.0704	1,9509	0,0734
0,5	24	patient	0,2381	0.0523/0.05		
0,5	25	control	0,3278	0.074/0.0696	1,7576	0,1012
0,5	25	patient	0,2445	0.0543/0.05		
0,5	26	control	0,3343	0.0698/0.0709	1,5988	0,13
0,5	26	patient	0,2516	0.0636/0.0585		
0,5	27	control	0,3406	0.0734/0.0716	1,6099	0,126
0,5	27	patient	0,2558	0.0655/0.059		
0,5	28	control	0,3459	0.0719/0.0696	1,6530	0,1192
0,5	28	patient	0,2586	0.0677/0.0575		
0,5	29	control	0,3500	0.0734/0.0738	1,2981	0,214
0,5	29	patient	0,2726	0.087/0.0694		
0,5	30	control	0,3453	0.0848/0.0813	1,0191	0,32667333
0,5	30	patient	0,2794	0.088/0.0719		
0,5	31	control	0,3499	0.0875/0.0832	0,9686	0,35131535
0,5	31	patient	0,2867	0.0881/0.0699		
0,5	32	control	0,3542	0.0853/0.0819	0,9765	0,34698635
0,5	32	patient	0,2905	0.0878/0.0721		
0,5	33	control	0,3586	0.0864/0.0828	0,9427	0,36396936
0,5	33	patient	0,2972	0.0915/0.0705		
0,5	34	control	0,3802	0.0742/0.0668	1,2293	0,24608725
0,5	34	patient	0,3037	0.0921/0.0698		
0,5	35	control	0,3971	0.0665/0.0699	1,4223	0,18015318
0,5	35	patient	0,3086	0.0907/0.0714		
0,5	36	control	0,4274	0.0711/0.0642	1,7623	0,1025641
0,5	36	patient	0,3073	0.0972/0.0786		
0,5	37	control	0,4307	0.0683/0.0615	1,6638	0,12587413
0,5	37	patient	0,3169	0.0992/0.0807		
0,5	38	control	0,4343	0.0676/0.0594	1,6375	0,12898213
0,5	38	patient	0,3218	0.0974/0.0808		
0,5	39	control	0,4369	0.0685/0.0615	3,2630	0,00883838
0,5	39	patient	0,2830	0.0541/0.057		
0,5	40	control	0,4394	0.068/0.0593	3,0369	0,01515152
0,5	40	patient	0,3092	0.0445/0.0461		
0,5	41	control	0,4427	0.0676/0.0584	2,9940	0,01298701
0,5	41	patient	0,3144	0.045/0.0478		

Threshold	Network size	Group	Mean *C*	Confidence interval *C*	t-values	p-values
0,5	42	control	0,4439	0.067/0.0586	2,9511	0,01731602
0,5	42	patient	0,3165	0.0472/0.0472		
0,5	43	control	0,4416	0.0557/0.0537	2,9303	0,02164502
0,5	43	patient	0,3205	0.0486/0.0501		
0,5	44	control	0,4440	0.0555/0.0522	2,8631	0,02164502
0,5	44	patient	0,3251	0.0488/0.0497		
0,5	45	control	0,4576	0.0495/0.0572	2,6326	0,03463203
0,5	45	patient	0,3376	0.059/0.0585		
0,5	46	control	0,4582	0.0507/0.0579	2,1429	0,08730159
0,5	46	patient	0,3584	0.0601/0.0617		
0,5	47	control	0,4616	0.0506/0.0585	2,0788	0,08730159
0,5	47	patient	0,3632	0.0619/0.0617		
0,6	10	control	0,0550	0.0261/0.0209	0,0081	0,9948
0,6	10	patient	0,0548	0.0515/0.0366		
0,6	11	control	0,0643	0.0286/0.0234	1,3274	0,2054
0,6	11	patient	0,0394	0.0251/0.0189		
0,6	12	control	0,0771	0.03/0.0268	1,5256	0,1358
0,6	12	patient	0,0447	0.03/0.0212		
0,6	13	control	0,0888	0.033/0.0303	1,7389	0,0968
0,6	13	patient	0,0501	0.0296/0.0221		
0,6	14	control	0,0961	0.0329/0.0308	1,5209	0,1382
0,6	14	patient	0,0599	0.0335/0.0249		
0,6	15	control	0,1002	0.0365/0.0338	1,2911	0,2072
0,6	15	patient	0,0673	0.0345/0.0259		
0,6	16	control	0,1087	0.0373/0.0354	1,3299	0,1894
0,6	16	patient	0,0739	0.0356/0.0268		
0,6	17	control	0,1140	0.0369/0.0363	1,1992	0,2434
0,6	17	patient	0,0816	0.0372/0.0293		
0,6	18	control	0,1201	0.0359/0.035	1,2209	0,2294
0,6	18	patient	0,0848	0.043/0.0353		
0,6	19	control	0,1201	0.038/0.0366	0,8229	0,4398
0,6	19	patient	0,0952	0.0429/0.037		
0,6	20	control	0,1445	0.0538/0.047	1,1080	0,3004
0,6	20	patient	0,1054	0.0435/0.0368		
0,6	21	control	0,1524	0.054/0.0487	1,1252	0,2934
0,6	21	patient	0,1120	0.0454/0.0389		
0,6	22	control	0,1594	0.0555/0.0507	1,1223	0,2952
0,6	22	patient	0,1176	0.0477/0.0403		
0,6	23	control	0,1840	0.0555/0.0452	1,5911	0,1368
0,6	23	patient	0,1250	0.0478/0.0415		
0,6	24	control	0,1914	0.0545/0.0438	1,6056	0,1314
0,6	24	patient	0,1316	0.0481/0.043		

Threshold	Network size	Group	Mean *C*	Confidence interval *C*	t-values	p-values
0,6	25	control	0,1953	0.0553/0.0476	1,4596	0,1744
0,6	25	patient	0,1383	0.0499/0.0458		
0,6	26	control	0,2044	0.0557/0.0466	1,5198	0,1528
0,6	26	patient	0,1384	0.0651/0.0506		
0,6	27	control	0,2111	0.0541/0.0436	1,4898	0,161
0,6	27	patient	0,1457	0.0657/0.0513		
0,6	28	control	0,2180	0.0566/0.0467	1,6037	0,1328
0,6	28	patient	0,1448	0.0699/0.0551		
0,6	29	control	0,2237	0.0564/0.0483	1,2224	0,2432
0,6	29	patient	0,1584	0.089/0.0636		
0,6	30	control	0,2268	0.0642/0.0522	1,1046	0,3036963
0,6	30	patient	0,1619	0.0935/0.0654		
0,6	31	control	0,2306	0.0626/0.0536	1,0467	0,32900433
0,6	31	patient	0,1673	0.0945/0.0681		
0,6	32	control	0,2372	0.0649/0.0526	1,0278	0,33699634
0,6	32	patient	0,1746	0.096/0.0694		
0,6	33	control	0,2408	0.0645/0.0513	1,0241	0,33866134
0,6	33	patient	0,1775	0.0977/0.0717		
0,6	34	control	0,2656	0.0568/0.0491	1,3254	0,21744922
0,6	34	patient	0,1837	0.0988/0.0731		
0,6	35	control	0,2724	0.0559/0.0485	1,3462	0,20845821
0,6	35	patient	0,1881	0.104/0.0731		
0,6	36	control	0,2820	0.0688/0.0628	1,2924	0,22144522
0,6	36	patient	0,1854	0.1074/0.0868		
0,6	37	control	0,3020	0.0611/0.0653	1,4399	0,18181818
0,6	37	patient	0,1921	0.1106/0.0878		
0,6	38	control	0,3034	0.0671/0.0625	1,3691	0,1973582
0,6	38	patient	0,1973	0.1104/0.0916		
0,6	39	control	0,3075	0.0614/0.0668	3,1540	0,01388889
0,6	39	patient	0,1513	0.0516/0.0625		
0,6	40	control	0,3096	0.0629/0.0657	3,0056	0,01948052
0,6	40	patient	0,1817	0.0382/0.044		
0,6	41	control	0,3128	0.0601/0.0661	2,9763	0,01948052
0,6	41	patient	0,1858	0.0379/0.045		
0,6	42	control	0,3154	0.0606/0.0661	2,9325	0,01948052
0,6	42	patient	0,1884	0.0399/0.0459		
0,6	43	control	0,3113	0.0559/0.0576	3,0222	0,01948052
0,6	43	patient	0,1910	0.0394/0.0455		
0,6	44	control	0,3114	0.0513/0.0598	2,8353	0,01948052
0,6	44	patient	0,1965	0.0409/0.0471		
0,6	45	control	0,3239	0.0492/0.0601	2,5615	0,04112554
0,6	45	patient	0,2112	0.0497/0.0527		

Threshold	Network size	Group	Mean *C*	Confidence interval *C*	t-values	p-values
0,6	46	control	0,3255	0.0491/0.0593	2,1546	0,07936508
0,6	46	patient	0,2368	0.0422/0.0422		
0,6	47	control	0,3280	0.0485/0.061	2,0650	0,07936508
0,6	47	patient	0,2411	0.0417/0.0425		
0,7	10	control	0,0172	0.0065/0.0059	-0,0390	0,9946
0,7	10	patient	0,0177	0.0255/0.016		
0,7	11	control	0,0204	0.0073/0.0067	2,1480	0,0492
0,7	11	patient	0,0079	0.0093/0.0061		
0,7	12	control	0,0269	0.0087/0.0088	2,7379	0,0162
0,7	12	patient	0,0086	0.0101/0.0066		
0,7	13	control	0,0317	0.0087/0.0089	3,1378	0,0092
0,7	13	patient	0,0099	0.0103/0.0072		
0,7	14	control	0,0362	0.0113/0.0112	2,9457	0,0118
0,7	14	patient	0,0119	0.0113/0.008		
0,7	15	control	0,0328	0.0136/0.0133	2,1017	0,0516
0,7	15	patient	0,0127	0.0129/0.0091		
0,7	16	control	0,0372	0.0152/0.0149	1,9671	0,0632
0,7	16	patient	0,0157	0.0153/0.0106		
0,7	17	control	0,0402	0.016/0.0157	1,9930	0,0638
0,7	17	patient	0,0170	0.016/0.0115		
0,7	18	control	0,0450	0.0179/0.0172	2,1005	0,0518
0,7	18	patient	0,0183	0.0167/0.0121		
0,7	19	control	0,0414	0.0171/0.0176	1,5452	0,15
0,7	19	patient	0,0210	0.0195/0.0136		
0,7	20	control	0,0555	0.0285/0.0248	1,8702	0,0846
0,7	20	patient	0,0230	0.0198/0.0144		
0,7	21	control	0,0573	0.0269/0.0257	1,8678	0,0868
0,7	21	patient	0,0251	0.0209/0.0151		
0,7	22	control	0,0609	0.0299/0.028	1,8417	0,0898
0,7	22	patient	0,0263	0.0231/0.0165		
0,7	23	control	0,0802	0.0301/0.0251	2,8091	0,0166
0,7	23	patient	0,0279	0.0233/0.0172		
0,7	24	control	0,0833	0.0302/0.0264	2,6157	0,0224
0,7	24	patient	0,0314	0.0264/0.0187		
0,7	25	control	0,0883	0.0297/0.0237	2,7709	0,0164
0,7	25	patient	0,0334	0.0266/0.0199		
0,7	26	control	0,0939	0.0317/0.0264	2,3832	0,0312
0,7	26	patient	0,0393	0.0334/0.0227		
0,7	27	control	0,0989	0.0339/0.0276	2,3036	0,0378
0,7	27	patient	0,0421	0.037/0.0245		
0,7	28	control	0,1043	0.0342/0.0286	2,4262	0,0314
0,7	28	patient	0,0450	0.0354/0.0235		

Threshold	Network size	Group	Mean *C*	Confidence interval *C*	t-values	p-values
0,7	29	control	0,1075	0.0351/0.0297	1,9417	0,0762
0,7	29	patient	0,0519	0.0445/0.029		
0,7	30	control	0,1061	0.0425/0.0292	1,5823	0,15417915
0,7	30	patient	0,0548	0.0476/0.0312		
0,7	31	control	0,1107	0.0426/0.0283	1,5919	0,15184815
0,7	31	patient	0,0580	0.0494/0.0328		
0,7	32	control	0,1137	0.043/0.0296	1,5070	0,17282717
0,7	32	patient	0,0610	0.0532/0.0343		
0,7	33	control	0,1184	0.0442/0.0294	1,5132	0,17182817
0,7	33	patient	0,0634	0.0556/0.0353		
0,7	34	control	0,1430	0.0453/0.0417	1,9679	0,07659008
0,7	34	patient	0,0671	0.0577/0.0377		
0,7	35	control	0,1510	0.0441/0.0403	1,9991	0,07326007
0,7	35	patient	0,0709	0.0619/0.0397		
0,7	36	control	0,1437	0.0499/0.04	1,6277	0,13442113
0,7	36	patient	0,0726	0.0621/0.0408		
0,7	37	control	0,1501	0.0517/0.0427	1,6038	0,13986014
0,7	37	patient	0,0788	0.064/0.0419		
0,7	38	control	0,1533	0.0512/0.0428	1,5486	0,15229215
0,7	38	patient	0,0813	0.0672/0.0435		
0,7	39	control	0,1565	0.0497/0.0416	4,2087	0,00126263
0,7	39	patient	0,0508	0.0147/0.0189		
0,7	40	control	0,1582	0.0568/0.0441	3,6859	0,0021645
0,7	40	patient	0,0626	0.0087/0.0082		
0,7	41	control	0,1616	0.053/0.0443	3,6328	0,0021645
0,7	41	patient	0,0652	0.0096/0.0098		
0,7	42	control	0,1640	0.0538/0.0445	3,5960	0,0021645
0,7	42	patient	0,0679	0.0105/0.0105		
0,7	43	control	0,1616	0.0452/0.0393	3,9006	0,0021645
0,7	43	patient	0,0696	0.0107/0.0106		
0,7	44	control	0,1651	0.0471/0.0404	3,8645	0,0021645
0,7	44	patient	0,0718	0.0116/0.0109		
0,7	45	control	0,1752	0.0451/0.0445	3,5999	0,00649351
0,7	45	patient	0,0811	0.0197/0.0174		
0,7	46	control	0,1786	0.0486/0.046	3,0601	0,01587302
0,7	46	patient	0,0885	0.0216/0.0198		
0,7	47	control	0,1808	0.0459/0.0454	3,0473	0,01587302
0,7	47	patient	0,0907	0.0251/0.0213		
0,8	10	control	0,0011	0.0009/0.0008	-0,4894	0,9654
0,8	10	patient	0,0022	0.0041/0.0022		
0,8	11	control	0,0014	0.0014/0.0012	1,3927	0,23
0,8	11	patient	0,0004	0.0004/0.0004		

Threshold	Network size	Group	Mean *C*	Confidence interval *C*	t-values	p-values
0,8	12	control	0,0016	0.0015/0.0013	1,5486	0,1448
0,8	12	patient	0,0004	0.0006/0.0004		
0,8	13	control	0,0020	0.0017/0.0016	1,5578	0,1434
0,8	13	patient	0,0005	0.0007/0.0005		
0,8	14	control	0,0028	0.0025/0.0024	1,5403	0,1472
0,8	14	patient	0,0007	0.0009/0.0007		
0,8	15	control	0,0033	0.003/0.0029	1,4179	0,193
0,8	15	patient	0,0009	0.001/0.0009		
0,8	16	control	0,0032	0.003/0.0025	1,4821	0,1374
0,8	16	patient	0,0008	0.0012/0.0008		
0,8	17	control	0,0036	0.0032/0.0029	1,3347	0,1744
0,8	17	patient	0,0012	0.0015/0.0012		
0,8	18	control	0,0044	0.004/0.0037	1,4705	0,1664
0,8	18	patient	0,0012	0.0015/0.001		
0,8	19	control	0,0049	0.0042/0.0035	1,8303	0,1018
0,8	19	patient	0,0009	0.0013/0.0009		
0,8	20	control	0,0064	0.0061/0.0052	1,6615	0,1218
0,8	20	patient	0,0013	0.0016/0.0013		
0,8	21	control	0,0073	0.0067/0.0055	1,6952	0,106
0,8	21	patient	0,0015	0.0022/0.0015		
0,8	22	control	0,0075	0.0067/0.0056	1,7608	0,115
0,8	22	patient	0,0015	0.0017/0.0012		
0,8	23	control	0,0092	0.0076/0.0066	1,9772	0,0666
0,8	23	patient	0,0018	0.0023/0.0018		
0,8	24	control	0,0102	0.0087/0.0075	1,9731	0,0654
0,8	24	patient	0,0018	0.0022/0.0018		
0,8	25	control	0,0109	0.0088/0.0078	2,0413	0,0522
0,8	25	patient	0,0021	0.0025/0.0018		
0,8	26	control	0,0124	0.0107/0.0089	1,7211	0,1104
0,8	26	patient	0,0030	0.003/0.0023		
0,8	27	control	0,0128	0.0112/0.0091	1,7996	0,105
0,8	27	patient	0,0028	0.0028/0.0022		
0,8	28	control	0,0140	0.0113/0.01	1,8749	0,0962
0,8	28	patient	0,0031	0.0034/0.0031		
0,8	29	control	0,0143	0.0115/0.0098	1,8218	0,1036
0,8	29	patient	0,0033	0.0034/0.0025		
0,8	30	control	0,0174	0.0132/0.0118	2,0891	0,06193806
0,8	30	patient	0,0038	0.0038/0.0028		
0,8	31	control	0,0189	0.0146/0.0126	2,1410	0,04195804
0,8	31	patient	0,0038	0.0038/0.0029		
0,8	32	control	0,0195	0.0148/0.013	2,1159	0,04761905
0,8	32	patient	0,0042	0.0045/0.0032		

Threshold	Network size	Group	Mean *C*	Confidence interval *C*	t-values	p-values
0,8	33	control	0,0200	0.0156/0.0138	2,0745	0,05228105
0,8	33	patient	0,0043	0.0045/0.0033		
0,8	34	control	0,0230	0.0169/0.0157	2,1565	0,04229104
0,8	34	patient	0,0048	0.0048/0.0036		
0,8	35	control	0,0241	0.0167/0.0152	2,3048	0,03696304
0,8	35	patient	0,0049	0.0049/0.0037		
0,8	36	control	0,0300	0.018/0.018	2,8416	0,01165501
0,8	36	patient	0,0053	0.0053/0.0039		
0,8	37	control	0,0288	0.0157/0.0158	2,7662	0,01631702
0,8	37	patient	0,0059	0.0059/0.0046		
0,8	38	control	0,0311	0.0173/0.0175	2,6388	0,01631702
0,8	38	patient	0,0066	0.0068/0.0052		
0,8	39	control	0,0315	0.0177/0.0177	2,3187	0,04040404
0,8	39	patient	0,0079	0.0075/0.0062		
0,8	40	control	0,0344	0.0183/0.0187	2,1765	0,04978355
0,8	40	patient	0,0097	0.0086/0.0075		
0,8	41	control	0,0350	0.0191/0.0191	2,0872	0,06709957
0,8	41	patient	0,0104	0.0092/0.0081		
0,8	42	control	0,0363	0.0192/0.0195	2,2092	0,06060606
0,8	42	patient	0,0102	0.0087/0.008		
0,8	43	control	0,0409	0.0236/0.0233	2,0368	0,06060606
0,8	43	patient	0,0117	0.0102/0.009		
0,8	44	control	0,0425	0.0255/0.0244	2,0015	0,06926407
0,8	44	patient	0,0122	0.0097/0.009		
0,8	45	control	0,0419	0.026/0.0246	1,9928	0,06709957
0,8	45	patient	0,0121	0.0102/0.0095		
0,8	46	control	0,0443	0.0284/0.0262	1,6465	0,13492063
0,8	46	patient	0,0151	0.0117/0.0117		
0,8	47	control	0,0469	0.0286/0.0267	1,7186	0,12698413
0,8	47	patient	0,0159	0.0123/0.0123		

Table B2. Descriptive statistics of *ANDeg* of *in vitro* neural networks of experimental groups across thresholds and network sizes.

Threshold	Network size	Group	Mean *ANDeg*	Confidence interval *ANDeg*	t-values	p-values
0,2	10	control	6,4954	0.3034/0.2673	0,9210	0,3766
0,2	10	patient	6,2318	0.4398/0.4401		
0,2	11	control	7,0026	0.3464/0.3111	1,7116	0,1076
0,2	11	patient	6,5478	0.3316/0.3977		
0,2	12	control	7,5941	0.3353/0.3183	2,0411	0,054
0,2	12	patient	7,0185	0.3663/0.4472		
0,2	13	control	8,0683	0.3742/0.3612	1,9162	0,0718
0,2	13	patient	7,4688	0.3994/0.4812		
0,2	14	control	8,6027	0.4138/0.3884	2,0600	0,0542
0,2	14	patient	7,9035	0.4308/0.5085		
0,2	15	control	8,8396	0.637/0.7636	0,9864	0,3418
0,2	15	patient	8,3635	0.4849/0.5678		
0,2	16	control	9,3263	0.6889/0.7976	1,1036	0,2878
0,2	16	patient	8,7642	0.5176/0.5873		
0,2	17	control	9,8223	0.7478/0.9264	1,0991	0,2898
0,2	17	patient	9,2221	0.5378/0.6025		
0,2	18	control	10,2818	0.7818/0.932	1,2182	0,2364
0,2	18	patient	9,5604	0.6387/0.6992		
0,2	19	control	10,7252	0.9375/1.0927	1,2385	0,235
0,2	19	patient	9,8844	0.7386/0.7734		
0,2	20	control	11,4517	1.1487/1.3042	1,4019	0,1842
0,2	20	patient	10,3694	0.746/0.7772		
0,2	21	control	11,9311	1.1753/1.3644	1,3824	0,1902
0,2	21	patient	10,8199	0.7858/0.8382		
0,2	22	control	12,5270	1.3016/1.4887	1,4673	0,1654
0,2	22	patient	11,2557	0.7989/0.8559		
0,2	23	control	13,7067	0.9807/0.9974	2,7475	0,0156
0,2	23	patient	11,6900	0.8565/0.9176		
0,2	24	control	14,2272	1.0464/1.0588	2,7288	0,016
0,2	24	patient	12,1397	0.8952/0.9417		
0,2	25	control	14,6104	1.27/1.1677	2,4255	0,0316
0,2	25	patient	12,5783	0.953/0.9839		
0,2	26	control	15,1314	1.259/1.2056	2,3757	0,0362
0,2	26	patient	13,0414	1.0262/1.0513		
0,2	27	control	15,6492	1.3744/1.2593	2,3710	0,0368
0,2	27	patient	13,4450	1.0579/1.1275		
0,2	28	control	16,2001	1.4555/1.3104	2,4479	0,031
0,2	28	patient	13,8080	1.1419/1.1895		
0,2	29	control	16,7206	1.4828/1.3334	2,6058	0,024
0,2	29	patient	14,1632	1.1054/1.1899		

Threshold	Network size	Group	Mean *ANDeg*	Confidence interval *ANDeg*	t-values	p-values
0,2	30	control	16,9150	1.5653/1.4649	2,2162	0,04928405
0,2	30	patient	14,5869	1.1081/1.2166		
0,2	31	control	17,4151	1.6393/1.56	2,1645	0,05527806
0,2	31	patient	15,0449	1.1623/1.2439		
0,2	32	control	17,9410	1.6784/1.58	2,2008	0,05061605
0,2	32	patient	15,4645	1.2061/1.275		
0,2	33	control	18,4556	1.7056/1.6353	2,1998	0,05094905
0,2	33	patient	16,0008	1.1571/1.224		
0,2	34	control	19,1440	1.6693/1.5795	2,4265	0,03396603
0,2	34	patient	16,4109	1.2093/1.2861		
0,2	35	control	19,9854	1.6344/1.5997	2,7902	0,01665002
0,2	35	patient	16,8435	1.2678/1.3014		
0,2	36	control	20,9083	1.7375/1.6446	3,0125	0,01243201
0,2	36	patient	17,2868	1.2907/1.3436		
0,2	37	control	21,3095	1.8593/1.8593	2,9212	0,01787102
0,2	37	patient	17,6852	1.2824/1.3295		
0,2	38	control	21,8470	1.9136/1.9136	2,9154	0,01709402
0,2	38	patient	18,1112	1.3554/1.4082		
0,2	39	control	22,4027	1.9525/1.9525	3,2069	0,01262626
0,2	39	patient	18,1875	1.3607/1.3828		
0,2	40	control	22,9427	2.0099/2.0099	2,9318	0,01731602
0,2	40	patient	19,0945	1.2546/1.2254		
0,2	41	control	23,4967	2.0479/2.0479	2,9350	0,01731602
0,2	41	patient	19,5564	1.2787/1.276		
0,2	42	control	24,0102	2.1216/2.1216	2,8972	0,01948052
0,2	42	patient	20,0105	1.2986/1.3417		
0,2	43	control	24,1951	1.8364/1.8118	2,9268	0,01948052
0,2	43	patient	20,4352	1.3411/1.3411		
0,2	44	control	24,7272	1.9009/1.8533	2,9374	0,01948052
0,2	44	patient	20,8717	1.3677/1.3677		
0,2	45	control	25,6267	2.6554/2.2584	2,7277	0,02164502
0,2	45	patient	21,4022	1.4125/1.4534		
0,2	46	control	26,1507	2.731/2.2991	2,3195	0,05555556
0,2	46	patient	22,3372	1.3048/1.5919		
0,2	47	control	26,6894	2.8091/2.3669	2,3161	0,05555556
0,2	47	patient	22,7751	1.3326/1.6376		
0,3	10	control	4,8826	0.3284/0.3031	1,0266	0,326
0,3	10	patient	4,5686	0.4807/0.4602		
0,3	11	control	5,1992	0.3967/0.3518	1,8063	0,089
0,3	11	patient	4,6937	0.3404/0.3775		
0,3	12	control	5,6073	0.4102/0.3872	2,1008	0,0518
0,3	12	patient	4,9630	0.3787/0.4111		

Threshold	Network size	Group	Mean *ANDeg*	Confidence interval *ANDeg*	t-values	p-values
0,3	13	control	5,9309	0.4514/0.4465	2,0809	0,054
0,3	13	patient	5,2278	0.4076/0.4415		
0,3	14	control	6,2626	0.496/0.4687	2,0790	0,0536
0,3	14	patient	5,4919	0.4614/0.5152		
0,3	15	control	6,3507	0.7145/0.7972	1,1940	0,2492
0,3	15	patient	5,7562	0.5009/0.5207		
0,3	16	control	6,6427	0.7608/0.8926	1,3040	0,213
0,3	16	patient	5,9619	0.5124/0.5457		
0,3	17	control	6,9644	0.8319/0.8992	1,3623	0,1944
0,3	17	patient	6,2043	0.5562/0.5742		
0,3	18	control	7,2598	0.8474/0.9745	1,4441	0,169
0,3	18	patient	6,3758	0.656/0.6807		
0,3	19	control	7,5088	1.0205/1.0984	1,3548	0,2014
0,3	19	patient	6,5554	0.7504/0.7616		
0,3	20	control	8,0373	1.2079/1.3298	1,4892	0,1598
0,3	20	patient	6,8714	0.7366/0.7614		
0,3	21	control	8,3552	1.2569/1.3856	1,4797	0,1628
0,3	21	patient	7,1422	0.763/0.8096		
0,3	22	control	8,7067	1.3483/1.4896	1,5232	0,1514
0,3	22	patient	7,3726	0.8077/0.8353		
0,3	23	control	9,6831	1.1576/1.1661	2,6212	0,023
0,3	23	patient	7,6365	0.8302/0.8768		
0,3	24	control	10,0141	1.1789/1.1941	2,6091	0,022
0,3	24	patient	7,9022	0.8994/0.9344		
0,3	25	control	10,2438	1.2871/1.2735	2,4077	0,0334
0,3	25	patient	8,1670	0.9343/0.957		
0,3	26	control	10,6133	1.4046/1.3059	2,2570	0,0454
0,3	26	patient	8,5630	0.9519/0.9834		
0,3	27	control	10,9559	1.5126/1.4252	2,2573	0,0456
0,3	27	patient	8,7972	0.9945/1.0457		
0,3	28	control	11,2850	1.5225/1.4701	2,2612	0,0436
0,3	28	patient	9,0335	1.0564/1.085		
0,3	29	control	11,6195	1.5377/1.5131	2,4454	0,0334
0,3	29	patient	9,1857	0.9576/1.0449		
0,3	30	control	11,6243	1.7052/1.609	2,0544	0,06726607
0,3	30	patient	9,4354	0.9796/1.0637		
0,3	31	control	11,9693	1.7921/1.747	2,0585	0,06626707
0,3	31	patient	9,6885	1.0525/1.0968		
0,3	32	control	12,3173	1.8598/1.7897	2,0754	0,06460206
0,3	32	patient	9,9457	1.0675/1.1771		
0,3	33	control	12,6505	2.0037/1.7908	2,0736	0,06426906
0,3	33	patient	10,2489	1.0613/1.1092		

Threshold	Network size	Group	Mean *ANDeg*	Confidence interval *ANDeg*	t-values	p-values
0,3	34	control	13,2256	1.8325/1.7621	2,3710	0,03596404
0,3	34	patient	10,5212	1.0826/1.175		
0,3	35	control	13,8136	1.8208/1.7341	2,6921	0,01631702
0,3	35	patient	10,7420	1.1229/1.1898		
0,3	36	control	14,5874	1.8761/1.8665	2,9354	0,01320901
0,3	36	patient	10,9779	1.1858/1.2681		
0,3	37	control	14,6692	2.2437/2.2437	2,6065	0,02408702
0,3	37	patient	11,2277	1.2006/1.2832		
0,3	38	control	15,0100	2.2853/2.2745	2,6086	0,02486402
0,3	38	patient	11,4826	1.2297/1.3194		
0,3	39	control	15,3637	2.3614/2.3614	2,8671	0,01641414
0,3	39	patient	11,3507	1.2133/1.3461		
0,3	40	control	15,7229	2.4282/2.4282	2,5203	0,03030303
0,3	40	patient	12,1647	1.0249/1.1091		
0,3	41	control	16,0644	2.4533/2.4968	2,5147	0,03030303
0,3	41	patient	12,4235	1.0383/1.1135		
0,3	42	control	16,4288	2.5288/2.3486	2,5557	0,02813853
0,3	42	patient	12,6760	1.1112/1.1636		
0,3	43	control	16,5404	2.3445/2.3445	2,5647	0,02813853
0,3	43	patient	12,9389	1.0739/1.1482		
0,3	44	control	16,8408	2.404/2.2417	2,5261	0,03030303
0,3	44	patient	13,2000	1.1079/1.1743		
0,3	45	control	17,7031	3.3803/2.9621	2,2927	0,04112554
0,3	45	patient	13,5722	1.1974/1.2347		
0,3	46	control	18,0553	3.4292/3.0211	1,9293	0,08730159
0,3	46	patient	14,2949	1.0897/1.2792		
0,3	47	control	18,4295	3.5113/3.1096	1,9226	0,0952381
0,3	47	patient	14,5859	1.0592/1.2971		
0,4	10	control	3,7293	0.2909/0.2644	0,8542	0,4106
0,4	10	patient	3,5018	0.445/0.3698		
0,4	11	control	3,9176	0.3302/0.2992	1,7615	0,0962
0,4	11	patient	3,5169	0.2719/0.2707		
0,4	12	control	4,1847	0.3879/0.3691	1,9749	0,0628
0,4	12	patient	3,6658	0.3089/0.3103		
0,4	13	control	4,3966	0.4357/0.4044	2,0201	0,0578
0,4	13	patient	3,8093	0.3222/0.3335		
0,4	14	control	4,5866	0.4718/0.4369	1,9828	0,063
0,4	14	patient	3,9678	0.3465/0.35		
0,4	15	control	4,6159	0.6224/0.6481	1,2715	0,2212
0,4	15	patient	4,1033	0.388/0.3961		
0,4	16	control	4,8053	0.6697/0.6867	1,4247	0,1686
0,4	16	patient	4,1997	0.3976/0.3878		

Threshold	Network size	Group	Mean *ANDeg*	Confidence interval *ANDeg*	t-values	p-values
0,4	17	control	4,9827	0.6985/0.7357	1,3995	0,177
0,4	17	patient	4,3499	0.4299/0.4166		
0,4	18	control	5,1753	0.746/0.7803	1,4865	0,1532
0,4	18	patient	4,4466	0.5023/0.4857		
0,4	19	control	5,1924	0.8345/0.8439	1,1982	0,2588
0,4	19	patient	4,5552	0.5378/0.5161		
0,4	20	control	5,5370	0.9863/0.9796	1,3733	0,1984
0,4	20	patient	4,7191	0.5541/0.5261		
0,4	21	control	5,7420	1.0454/1.0449	1,4151	0,1844
0,4	21	patient	4,8518	0.5806/0.5493		
0,4	22	control	6,0028	1.1241/1.1274	1,4750	0,1688
0,4	22	patient	5,0013	0.5882/0.5857		
0,4	23	control	6,6458	0.9721/0.9461	2,4513	0,0302
0,4	23	patient	5,1530	0.6127/0.5913		
0,4	24	control	6,8441	1.0479/1.0282	2,4430	0,032
0,4	24	patient	5,2817	0.6476/0.628		
0,4	25	control	7,0199	1.0997/1.0225	2,3509	0,0386
0,4	25	patient	5,4421	0.673/0.6666		
0,4	26	control	7,2315	1.1545/1.1187	2,1408	0,0562
0,4	26	patient	5,6595	0.7892/0.7391		
0,4	27	control	7,4452	1.188/1.1372	2,1726	0,0518
0,4	27	patient	5,7810	0.794/0.7459		
0,4	28	control	7,6512	1.2914/1.2108	2,1788	0,0492
0,4	28	patient	5,9036	0.8577/0.7923		
0,4	29	control	7,8587	1.3074/1.2303	2,3712	0,0352
0,4	29	patient	5,9668	0.7551/0.7572		
0,4	30	control	7,8628	1.4715/1.3434	2,0061	0,07126207
0,4	30	patient	6,1189	0.7897/0.7791		
0,4	31	control	8,0731	1.5091/1.4885	1,9756	0,07492507
0,4	31	patient	6,2789	0.8783/0.8219		
0,4	32	control	8,2788	1.5916/1.5258	2,0058	0,07059607
0,4	32	patient	6,4026	0.8927/0.8372		
0,4	33	control	8,4885	1.6152/1.5912	2,0031	0,07026307
0,4	33	patient	6,5737	0.8606/0.8414		
0,4	34	control	8,9065	1.5547/1.4891	2,3663	0,03363303
0,4	34	patient	6,7049	0.8963/0.857		
0,4	35	control	9,3177	1.611/1.5588	2,6085	0,02197802
0,4	35	patient	6,8612	0.9498/0.868		
0,4	36	control	9,9894	1.6243/1.6243	2,9990	0,01243201
0,4	36	patient	6,9180	1.0055/1.0016		
0,4	37	control	10,0587	1.8223/1.8223	2,7553	0,01709402
0,4	37	patient	7,0643	1.0237/1.0561		

Threshold	Network size	Group	Mean *ANDeg*	Confidence interval *ANDeg*	t-values	p-values
0,4	38	control	10,2816	1.8754/1.8754	2,7574	0,01787102
0,4	38	patient	7,1994	1.0773/1.0691		
0,4	39	control	10,5019	1.9074/1.9074	3,2547	0,00378788
0,4	39	patient	6,9331	0.8811/1.0131		
0,4	40	control	10,7309	1.9678/1.9678	2,9332	0,00649351
0,4	40	patient	7,4982	0.6735/0.7308		
0,4	41	control	10,9261	2.0289/2.0289	2,8846	0,00865801
0,4	41	patient	7,6461	0.7089/0.7268		
0,4	42	control	11,1611	2.061/2.061	2,9459	0,00649351
0,4	42	patient	7,7502	0.7346/0.7647		
0,4	43	control	11,2007	1.9364/1.9364	2,9415	0,00649351
0,4	43	patient	7,9239	0.711/0.7654		
0,4	44	control	11,4125	1.9665/1.9665	2,9540	0,00649351
0,4	44	patient	8,0687	0.7496/0.7713		
0,4	45	control	12,0838	2.7789/2.4901	2,6182	0,01082251
0,4	45	patient	8,2126	0.7956/0.8217		
0,4	46	control	12,3508	3.0329/2.5589	2,2347	0,03968254
0,4	46	patient	8,6783	0.7324/0.8384		
0,4	47	control	12,5859	3.0872/2.6164	2,2364	0,03968254
0,4	47	patient	8,8415	0.7636/0.8624		
0,5	10	control	2,9570	0.2185/0.1781	0,5534	0,5886
0,5	10	patient	2,8517	0.3165/0.2657		
0,5	11	control	3,0724	0.2523/0.2018	1,6232	0,1236
0,5	11	patient	2,8084	0.2027/0.1881		
0,5	12	control	3,2098	0.2774/0.243	1,7949	0,0878
0,5	12	patient	2,8816	0.2219/0.2033		
0,5	13	control	3,3120	0.2937/0.257	1,7153	0,1072
0,5	13	patient	2,9697	0.248/0.2345		
0,5	14	control	3,4152	0.312/0.274	1,8317	0,0856
0,5	14	patient	3,0231	0.2681/0.2455		
0,5	15	control	3,4611	0.3835/0.38	1,3489	0,1928
0,5	15	patient	3,1130	0.2942/0.2744		
0,5	16	control	3,5805	0.4244/0.4173	1,6921	0,108
0,5	16	patient	3,1197	0.2972/0.2624		
0,5	17	control	3,6737	0.451/0.4322	1,6646	0,1148
0,5	17	patient	3,1987	0.31/0.2714		
0,5	18	control	3,7891	0.4655/0.4593	1,7498	0,098
0,5	18	patient	3,2518	0.3482/0.3056		
0,5	19	control	3,8085	0.5402/0.5186	1,4415	0,179
0,5	19	patient	3,3243	0.3616/0.3165		
0,5	20	control	4,0683	0.6569/0.613	1,7045	0,1156
0,5	20	patient	3,4067	0.3834/0.3291		

Threshold	Network size	Group	Mean *ANDeg*	Confidence interval *ANDeg*	t-values	p-values
0,5	21	control	4,1706	0.6752/0.6664	1,6851	0,1194
0,5	21	patient	3,4825	0.405/0.3482		
0,5	22	control	4,3242	0.7295/0.7163	1,7466	0,1068
0,5	22	patient	3,5595	0.4247/0.3702		
0,5	23	control	4,7122	0.7105/0.6668	2,5778	0,0236
0,5	23	patient	3,6254	0.444/0.3776		
0,5	24	control	4,8310	0.7237/0.6891	2,5662	0,0238
0,5	24	patient	3,7082	0.4696/0.3948		
0,5	25	control	4,9374	0.7953/0.7238	2,4774	0,0288
0,5	25	patient	3,7770	0.4826/0.4201		
0,5	26	control	5,0542	0.8252/0.7477	2,2127	0,0454
0,5	26	patient	3,9244	0.5809/0.4767		
0,5	27	control	5,1764	0.8597/0.8128	2,2105	0,0468
0,5	27	patient	3,9958	0.6114/0.4956		
0,5	28	control	5,2876	0.8777/0.817	2,1886	0,0512
0,5	28	patient	4,0684	0.6215/0.5256		
0,5	29	control	5,4043	0.9132/0.8566	2,2315	0,0452
0,5	29	patient	4,1148	0.637/0.5411		
0,5	30	control	5,3866	1.0519/0.9735	1,8751	0,09057609
0,5	30	patient	4,2003	0.6685/0.5637		
0,5	31	control	5,4996	1.0595/1.0034	1,8405	0,09423909
0,5	31	patient	4,2869	0.6913/0.5932		
0,5	32	control	5,6133	1.1274/1.0454	1,8699	0,09090909
0,5	32	patient	4,3587	0.7163/0.5911		
0,5	33	control	5,7340	1.1538/1.0798	1,8536	0,09423909
0,5	33	patient	4,4434	0.7495/0.6092		
0,5	34	control	5,9913	1.1094/1.0366	2,1539	0,05361305
0,5	34	patient	4,5250	0.7424/0.6315		
0,5	35	control	6,2657	1.0963/1.0481	2,4315	0,03196803
0,5	35	patient	4,5991	0.761/0.6357		
0,5	36	control	6,6788	1.1994/1.1591	2,7028	0,02175602
0,5	36	patient	4,6449	0.8304/0.7078		
0,5	37	control	6,7587	1.2452/1.2452	2,6039	0,02331002
0,5	37	patient	4,7314	0.8219/0.7221		
0,5	38	control	6,8898	1.2668/1.2668	2,6255	0,02331002
0,5	38	patient	4,7995	0.8572/0.7547		
0,5	39	control	7,0213	1.322/1.322	3,4778	0,00378788
0,5	39	patient	4,4974	0.493/0.5686		
0,5	40	control	7,1518	1.3602/1.3602	3,1038	0,00649351
0,5	40	patient	4,8047	0.3939/0.4222		
0,5	41	control	7,2973	1.3974/1.3974	3,1092	0,004329
0,5	41	patient	4,8892	0.3946/0.4428		

Threshold	Network size	Group	Mean *ANDeg*	Confidence interval *ANDeg*	t-values	p-values
0,5	42	control	7,4163	1.421/1.421	3,1168	0,00649351
0,5	42	patient	4,9461	0.4212/0.4606		
0,5	43	control	7,3975	1.4203/1.3062	3,1394	0,00649351
0,5	43	patient	5,0192	0.4122/0.4536		
0,5	44	control	7,5388	1.4507/1.3421	3,1520	0,00649351
0,5	44	patient	5,0878	0.4419/0.4669		
0,5	45	control	8,0960	2.2103/1.7918	2,6008	0,00865801
0,5	45	patient	5,2242	0.4581/0.5066		
0,5	46	control	8,2041	2.3901/1.8259	2,1989	0,03174603
0,5	46	patient	5,5074	0.3801/0.5146		
0,5	47	control	8,3458	2.2057/1.8571	2,2262	0,02380952
0,5	47	patient	5,5774	0.3919/0.5144		
0,6	10	control	2,4492	0.1261/0.1122	0,0794	0,9434
0,6	10	patient	2,4385	0.2413/0.1839		
0,6	11	control	2,5079	0.1423/0.1238	1,3180	0,2028
0,6	11	patient	2,3781	0.1344/0.1039		
0,6	12	control	2,5756	0.1548/0.1482	1,4442	0,1636
0,6	12	patient	2,4160	0.1512/0.1157		
0,6	13	control	2,6363	0.1745/0.1603	1,5580	0,133
0,6	13	patient	2,4497	0.1563/0.1263		
0,6	14	control	2,6865	0.1905/0.1721	1,5954	0,1248
0,6	14	patient	2,4809	0.1719/0.134		
0,6	15	control	2,7233	0.2133/0.2099	1,3428	0,1948
0,6	15	patient	2,5237	0.1855/0.1435		
0,6	16	control	2,7716	0.2312/0.2177	1,3465	0,1984
0,6	16	patient	2,5601	0.2011/0.1549		
0,6	17	control	2,8163	0.2454/0.2328	1,2438	0,2278
0,6	17	patient	2,6058	0.2196/0.1707		
0,6	18	control	2,8620	0.2485/0.2483	1,3120	0,2088
0,6	18	patient	2,6244	0.2399/0.1968		
0,6	19	control	2,8758	0.3022/0.2825	1,0480	0,32
0,6	19	patient	2,6662	0.2443/0.2015		
0,6	20	control	2,9989	0.3813/0.351	1,1454	0,2754
0,6	20	patient	2,7352	0.261/0.1988		
0,6	21	control	3,0521	0.3968/0.365	1,1850	0,258
0,6	21	patient	2,7683	0.2665/0.2063		
0,6	22	control	3,0954	0.4171/0.3824	1,1727	0,264
0,6	22	patient	2,8000	0.2845/0.2165		
0,6	23	control	3,2889	0.4254/0.3786	1,7414	0,1042
0,6	23	patient	2,8459	0.2888/0.2207		
0,6	24	control	3,3428	0.4261/0.3934	1,7476	0,1042
0,6	24	patient	2,8807	0.3022/0.2311		

Threshold	Network size	Group	Mean *ANDeg*	Confidence interval *ANDeg*	t-values	p-values
0,6	25	control	3,3828	0.4699/0.425	1,6477	0,1278
0,6	25	patient	2,9189	0.3168/0.2438		
0,6	26	control	3,4477	0.478/0.4436	1,4275	0,176
0,6	26	patient	2,9982	0.3855/0.2965		
0,6	27	control	3,5063	0.5058/0.4513	1,4290	0,1728
0,6	27	patient	3,0411	0.3978/0.3049		
0,6	28	control	3,5673	0.5132/0.4834	1,4454	0,1702
0,6	28	patient	3,0684	0.4206/0.3288		
0,6	29	control	3,6255	0.5563/0.5042	1,5266	0,1512
0,6	29	patient	3,0887	0.418/0.335		
0,6	30	control	3,7002	0.615/0.5734	1,4328	0,18081918
0,6	30	patient	3,1324	0.4439/0.3512		
0,6	31	control	3,7471	0.6236/0.6166	1,4169	0,18481518
0,6	31	patient	3,1697	0.4448/0.3595		
0,6	32	control	3,8240	0.6615/0.6557	1,4497	0,17649018
0,6	32	patient	3,2101	0.4659/0.3769		
0,6	33	control	3,8670	0.6759/0.6597	1,4228	0,18215118
0,6	33	patient	3,2489	0.4722/0.3814		
0,6	34	control	4,0124	0.6564/0.6353	1,6654	0,12587413
0,6	34	patient	3,2911	0.5025/0.3966		
0,6	35	control	4,1243	0.6619/0.6619	1,8284	0,0955711
0,6	35	patient	3,3263	0.5198/0.4095		
0,6	36	control	4,3755	0.7188/0.7167	2,1582	0,05050505
0,6	36	patient	3,3650	0.5294/0.4171		
0,6	37	control	4,5114	0.7206/0.7162	2,3197	0,04118104
0,6	37	patient	3,4075	0.5446/0.4278		
0,6	38	control	4,5717	0.7173/0.7074	2,3421	0,03962704
0,6	38	patient	3,4458	0.5776/0.4375		
0,6	39	control	4,6477	0.7509/0.7509	3,4031	0,00631313
0,6	39	patient	3,2349	0.2792/0.2853		
0,6	40	control	4,7091	0.7634/0.7634	3,0265	0,01082251
0,6	40	patient	3,3713	0.2622/0.2784		
0,6	41	control	4,7783	0.7832/0.7733	3,0494	0,01082251
0,6	41	patient	3,4040	0.2734/0.2864		
0,6	42	control	4,8558	0.8084/0.8063	3,0179	0,00865801
0,6	42	patient	3,4429	0.2849/0.3056		
0,6	43	control	4,8369	0.7427/0.7265	3,1451	0,01082251
0,6	43	patient	3,4723	0.2896/0.3132		
0,6	44	control	4,8783	0.768/0.74	3,0764	0,01082251
0,6	44	patient	3,5123	0.2937/0.314		
0,6	45	control	5,1969	1.2278/0.9931	2,6811	0,01082251
0,6	45	patient	3,5705	0.3228/0.3546		

Threshold	Network size	Group	Mean *ANDeg*	Confidence interval *ANDeg*	t-values	p-values
0,6	46	control	5,2575	1.2463/1.0032	2,3244	0,03968254
0,6	46	patient	3,7121	0.2708/0.3969		
0,6	47	control	5,3431	1.2924/1.0411	2,3042	0,03968254
0,6	47	patient	3,7546	0.2808/0.4004		
0,7	10	control	2,1955	0.0406/0.0397	-0,1200	0,9392
0,7	10	patient	2,2048	0.1567/0.11		
0,7	11	control	2,2166	0.0468/0.0468	1,3304	0,201
0,7	11	patient	2,1565	0.0757/0.0585		
0,7	12	control	2,2584	0.0626/0.0623	1,6182	0,1228
0,7	12	patient	2,1713	0.0851/0.0641		
0,7	13	control	2,2832	0.0678/0.0651	1,7288	0,0996
0,7	13	patient	2,1857	0.0904/0.0692		
0,7	14	control	2,3040	0.0739/0.0733	1,6633	0,1128
0,7	14	patient	2,2001	0.0971/0.0756		
0,7	15	control	2,3085	0.0957/0.1002	1,2906	0,208
0,7	15	patient	2,2128	0.1061/0.0817		
0,7	16	control	2,3293	0.1037/0.1043	1,3003	0,204
0,7	16	patient	2,2264	0.1163/0.0851		
0,7	17	control	2,3487	0.1114/0.1127	1,2484	0,2234
0,7	17	patient	2,2431	0.1232/0.0924		
0,7	18	control	2,3733	0.117/0.117	1,3360	0,1924
0,7	18	patient	2,2522	0.1307/0.1016		
0,7	19	control	2,3552	0.1112/0.1169	0,8608	0,4118
0,7	19	patient	2,2750	0.1377/0.1065		
0,7	20	control	2,4249	0.1622/0.1576	1,1604	0,2716
0,7	20	patient	2,2970	0.1379/0.1025		
0,7	21	control	2,4439	0.1746/0.1606	1,1171	0,2912
0,7	21	patient	2,3157	0.1409/0.1082		
0,7	22	control	2,4451	0.1813/0.1604	0,9985	0,3452
0,7	22	patient	2,3266	0.1597/0.1153		
0,7	23	control	2,5465	0.1704/0.1367	1,7472	0,107
0,7	23	patient	2,3430	0.156/0.1228		
0,7	24	control	2,5687	0.178/0.1413	1,7035	0,1152
0,7	24	patient	2,3596	0.1713/0.1254		
0,7	25	control	2,5805	0.1846/0.1512	1,5938	0,1402
0,7	25	patient	2,3766	0.1747/0.1332		
0,7	26	control	2,6086	0.1984/0.1589	1,3669	0,1954
0,7	26	patient	2,4124	0.2073/0.1544		
0,7	27	control	2,6362	0.2074/0.1724	1,3634	0,1968
0,7	27	patient	2,4289	0.2198/0.1636		
0,7	28	control	2,6615	0.2141/0.1718	1,4700	0,1654
0,7	28	patient	2,4292	0.2359/0.1724		

Threshold	Network size	Group	Mean *ANDeg*	Confidence interval *ANDeg*	t-values	p-values
0,7	29	control	2,6837	0.2276/0.1832	1,4612	0,1684
0,7	29	patient	2,4463	0.2403/0.1782		
0,7	30	control	2,7065	0.255/0.224	1,3186	0,21778222
0,7	30	patient	2,4648	0.238/0.1853		
0,7	31	control	2,7384	0.2741/0.2238	1,3665	0,20612721
0,7	31	patient	2,4802	0.2516/0.1928		
0,7	32	control	2,7614	0.2822/0.2396	1,3465	0,20912421
0,7	32	patient	2,4975	0.2633/0.2031		
0,7	33	control	2,7843	0.2951/0.2377	1,3628	0,20546121
0,7	33	patient	2,5077	0.2745/0.208		
0,7	34	control	2,8577	0.2748/0.2392	1,6151	0,13653014
0,7	34	patient	2,5281	0.2854/0.2149		
0,7	35	control	2,9140	0.2691/0.245	1,7650	0,10689311
0,7	35	patient	2,5446	0.2943/0.2201		
0,7	36	control	2,9905	0.3164/0.2855	1,8686	0,08857809
0,7	36	patient	2,5565	0.304/0.2271		
0,7	37	control	3,0623	0.3231/0.3311	2,0204	0,07148407
0,7	37	patient	2,5784	0.2991/0.2368		
0,7	38	control	3,0906	0.3349/0.327	2,0153	0,07070707
0,7	38	patient	2,5914	0.3193/0.2439		
0,7	39	control	3,1220	0.3442/0.3389	3,4894	0,00631313
0,7	39	patient	2,4622	0.1588/0.1553		
0,7	40	control	3,1461	0.3485/0.3424	3,0845	0,01731602
0,7	40	patient	2,5338	0.135/0.1372		
0,7	41	control	3,1800	0.3547/0.365	3,1173	0,01515152
0,7	41	patient	2,5454	0.1389/0.1435		
0,7	42	control	3,2083	0.3717/0.3613	3,1070	0,01515152
0,7	42	patient	2,5627	0.1416/0.1448		
0,7	43	control	3,1694	0.2723/0.318	3,3412	0,01948052
0,7	43	patient	2,5730	0.1454/0.1503		
0,7	44	control	3,1912	0.2728/0.326	3,2975	0,01948052
0,7	44	patient	2,5848	0.1504/0.157		
0,7	45	control	3,2907	0.3164/0.3712	3,2054	0,01731602
0,7	45	patient	2,6277	0.1727/0.1804		
0,7	46	control	3,3253	0.321/0.3778	2,8102	0,04761905
0,7	46	patient	2,6981	0.1623/0.1868		
0,7	47	control	3,3565	0.335/0.3843	2,7977	0,04761905
0,7	47	patient	2,7114	0.1682/0.191		
0,8	10	control	2,0515	0.0127/0.0137	-0,9769	0,4316
0,8	10	patient	2,0762	0.0502/0.0349		
0,8	11	control	2,0575	0.0154/0.0154	0,0661	0,9416
0,8	11	patient	2,0567	0.0174/0.0153		

Threshold	Network size	Group	Mean *ANDeg*	Confidence interval *ANDeg*	t-values	p-values
0,8	12	control	2,0696	0.018/0.0192	0,4458	0,6622
0,8	12	patient	2,0633	0.0195/0.0172		
0,8	13	control	2,0730	0.0188/0.0204	0,2098	0,8436
0,8	13	patient	2,0697	0.023/0.0201		
0,8	14	control	2,0828	0.0221/0.0234	0,9776	0,3458
0,8	14	patient	2,0654	0.0258/0.021		
0,8	15	control	2,0768	0.0287/0.0299	0,3469	0,7358
0,8	15	patient	2,0694	0.0286/0.0226		
0,8	16	control	2,0804	0.0314/0.0325	0,3029	0,7608
0,8	16	patient	2,0736	0.03/0.024		
0,8	17	control	2,0867	0.0318/0.0346	0,2775	0,783
0,8	17	patient	2,0801	0.0333/0.0258		
0,8	18	control	2,0931	0.0342/0.0366	0,5033	0,6274
0,8	18	patient	2,0797	0.0368/0.0296		
0,8	19	control	2,0879	0.037/0.0384	-0,0426	0,968
0,8	19	patient	2,0891	0.0378/0.0307		
0,8	20	control	2,1134	0.0592/0.0544	0,4498	0,6578
0,8	20	patient	2,0976	0.037/0.0306		
0,8	21	control	2,1189	0.0631/0.0579	0,4584	0,6484
0,8	21	patient	2,1018	0.0401/0.0309		
0,8	22	control	2,1133	0.0623/0.0559	0,1649	0,8666
0,8	22	patient	2,1072	0.0417/0.0339		
0,8	23	control	2,1384	0.0606/0.0512	0,7120	0,4904
0,8	23	patient	2,1122	0.0444/0.0358		
0,8	24	control	2,1441	0.0653/0.0531	0,7355	0,4806
0,8	24	patient	2,1158	0.0453/0.0366		
0,8	25	control	2,1553	0.064/0.0517	0,8645	0,4128
0,8	25	patient	2,1215	0.049/0.0389		
0,8	26	control	2,1622	0.069/0.0547	0,7809	0,4544
0,8	26	patient	2,1284	0.0534/0.0454		
0,8	27	control	2,1706	0.0734/0.0567	0,8989	0,388
0,8	27	patient	2,1303	0.0546/0.0444		
0,8	28	control	2,1760	0.0696/0.0581	0,9587	0,3574
0,8	28	patient	2,1307	0.0606/0.0499		
0,8	29	control	2,1801	0.0714/0.0601	0,6246	0,5306
0,8	29	patient	2,1457	0.0833/0.0628		
0,8	30	control	2,1894	0.0922/0.0737	0,6155	0,54312354
0,8	30	patient	2,1505	0.0876/0.0663		
0,8	31	control	2,1962	0.0959/0.0765	0,6338	0,52980353
0,8	31	patient	2,1551	0.0872/0.0648		
0,8	32	control	2,2051	0.0995/0.0788	0,6504	0,51948052
0,8	32	patient	2,1609	0.0938/0.0694		

Threshold	Network size	Group	Mean *ANDeg*	Confidence interval *ANDeg*	t-values	p-values
0,8	33	control	2,2084	0.1032/0.082	0,5975	0,55078255
0,8	33	patient	2,1666	0.0932/0.0715		
0,8	34	control	2,2427	0.097/0.0861	0,9858	0,34798535
0,8	34	patient	2,1716	0.102/0.0767		
0,8	35	control	2,2559	0.0944/0.0783	1,1253	0,28571429
0,8	35	patient	2,1767	0.1/0.0782		
0,8	36	control	2,2744	0.1164/0.1019	1,1675	0,27583528
0,8	36	patient	2,1802	0.1052/0.08		
0,8	37	control	2,2756	0.1085/0.0973	1,0386	0,32634033
0,8	37	patient	2,1904	0.1031/0.0827		
0,8	38	control	2,2830	0.1154/0.1026	1,0382	0,32711733
0,8	38	patient	2,1947	0.1078/0.086		
0,8	39	control	2,2919	0.1285/0.1063	2,0597	0,06060606
0,8	39	patient	2,1529	0.0578/0.0592		
0,8	40	control	2,2992	0.1302/0.1073	1,7642	0,10822511
0,8	40	patient	2,1752	0.056/0.0579		
0,8	41	control	2,3086	0.1334/0.1099	1,8206	0,0974026
0,8	41	patient	2,1778	0.0552/0.059		
0,8	42	control	2,3148	0.1356/0.1122	1,8226	0,0952381
0,8	42	patient	2,1816	0.0573/0.0599		
0,8	43	control	2,2952	0.0874/0.0874	1,7674	0,11471861
0,8	43	patient	2,1891	0.06/0.0669		
0,8	44	control	2,3013	0.0873/0.0873	1,8234	0,10822511
0,8	44	patient	2,1920	0.0588/0.0626		
0,8	45	control	2,3182	0.0903/0.0903	1,8110	0,1017316
0,8	45	patient	2,2043	0.0638/0.072		
0,8	46	control	2,3274	0.0943/0.0943	1,4633	0,18253968
0,8	46	patient	2,2263	0.0597/0.082		
0,8	47	control	2,3356	0.0946/0.0946	1,4658	0,19047619
0,8	47	patient	2,2327	0.0633/0.0858		